Studies of the General Circulation of the Atmosphere with a Simplified Moist General Circulation Model

Dargan M. W. Frierson

A Dissertation
Presented to the Faculty
of Princeton University
in Candidacy for the Degree
of Doctor of Philosophy

Recommended for Acceptance
by the Program in
Applied and Computational Mathematics

September 2005

Abstract

We formulate a simplified moist general circulation model (GCM) and use this model to study several topics in the moist general circulation of the atmosphere. The model consists of the full primitive equations on the sphere, with simplified physical parameterizations which isolate certain climate feedbacks and facilitate simulation over a wide range of parameters. A key simplification is the use of grey radiative transfer, in which water vapor and other constituents have no effect on radiative fluxes.

We first consider a set of experiments with no convection scheme (large scale condensation only) and study the effect of moisture on midlatitude static stability, eddy scales, and energy transports (this section is in collaboration with Isaac Held and Pablo Zurita-Gotor). We vary the moisture content of the atmosphere over a wide range, from dry to 10 times the moisture of the current climate, by varying a parameter in the Clausius-Clapeyron equation. In these simulations, the midlatitude static stability is found to be remarkably neutral with respect to moist convection. Despite the large changes in dry stability as the moisture content is increased, the eddy length scales in the simulations remain nearly constant, a fact we interpret with the Rhines scale at the jet latitude. Finally, as moisture content is increased, the poleward fluxes of energy are remarkably constant as well, indicating a high degree of compensation between dry static energy fluxes and moisture fluxes (the compensation is 99% from the control case to the dry limit). We interpret these findings with energy balance models, including a model with exact compensation, and a model which predicts the jet latitude and strength, and moist static energy diffusivity.

We then shift our focus to the tropics, first by deriving a one-dimensional model to study the effect of moisture on large-scale dynamics on the equator. We use this to formulate a theory for "precipitation fronts" in the tropical atmosphere, which mark the boundary between precipitating and non-precipitating regions in the tropics. This section is in collaboration with Andy Majda and Olivier Pauluis.

As the tropical circulation in the GCM is somewhat unrealistic with no convection scheme, we develop a simplified convection scheme in the style of Betts and Miller (1986) and study the effects of this scheme and its parameters on the zonally averaged circulation in the tropics. We find that a key categorization of convection schemes is whether these can build up and rapidly release convectively available potential energy. The formulation of some kind of shallow convection scheme is important in determining this behavior.

Acknowledgements

First and foremost I would like to thank my advisor Isaac Held, without whom none of this work and my growth as a scientist would have been possible. I have thoroughly enjoyed our frequent conversations, sharing in his remarkable insight and intuition into all aspects of the general circulation of the atmosphere. The experience of learning his unique way of attacking problems from all different angles has been invaluable.

My time here at Princeton has also greatly benefitted from frequent conversations with two postdocs, Pablo Zurita-Gotor and Olivier Pauluis. I have been very fortunate to learn from Pablo the subtleties of baroclinic eddies and midlatitude dynamics. From Olivier I have learned all about tropical dynamics, thermodynamics, and convection. Their willingness to share their experiences and knowledge with me has been a great source of enjoyment for me.

I would also like to acknowledge the contributions of Andy Majda to my graduate school experience, which began with a summer workshop he organized at UCLA in the summer of 2003. He then was gracious enough to take me on as a collaborator, and I have been fortunate to share in his wealth of knowledge of tropical dynamics and all branches of applied mathematics.

My fellow students have additionally been a great source for me: Edwin Gerber and Shree Khare. Ed and I have been compatriots since the beginning here, working side by side as the only two applied math students in atmospheric science. While Shree has spent much of the last few years in Boulder, I have enjoyed learning about data assimilation and statistics from him in his time here. I thank these friends as well as all the other applied math, atmospheric and oceanic sciences, and geosciences grad students I've worked with here at Princeton.

I have also benefitted from the professors in applied math, atmospheric and oceanic sciences, and other departments. Particularly helpful were courses from Weinan E, Geoff Vallis, Isaac Held, Leo Donner, Isidoro Orlanski, Steve Garner, Paul Kushner, Erhan Cinlar, Jorge Sarmiento, George Philander, Phil Holmes, Ronnie Sircar, Roscoe White, and Lex Smits. I have additionally enjoyed frequent conversations throughout my tenure with Ming Zhou, Alexey Fedorov, and Geoff Vallis.

Last I would like to thank my family and friends for being there for me throughout the last five years. This includes my parents, sister, grandparents, friends in Princeton and North Carolina, and, of course, my band the Jersey Sprawl.

Contents

Chapter 1

Introduction

To understand a physical system as complex as the atmosphere with any degree of sophistication requires a hierarchical modeling approach encompassing models of a wide range of complexity. One always interprets physical systems in terms of simpler ideas; this is done more effectively when quantitative predictions can be made with a self-consistent system, i.e., a simpler model. However in order to make connections with observations of the full system, or to make useful predictions, models of a high degree of complexity are often needed. We begin by discussing the current state of the modeling hierarchy in atmospheric science.

Due to the constant need for improved seasonal and long term climate forecasts, there is always much research in atmospheric science being done at the highest levels of complexity, i.e., full general circulation models (GCM's) and their associated parameterizations. Modeling teams from all around the world focus their efforts on improving the simulation of such physical processes as cloud physics, moist convection, and boundary layer dynamics, in order to make better predictions of the climate on a regional and global scale. These efforts have culminated in remarkable simulations of climate change scenarios (IPCC, 2001), as well as greatly improved forecasts of such phenomena as El Niño and the Southern Oscillation (Cane et al., 1986), and seasonal climate forecasting in general (Roads et al., 2001).

In concert with the forecast-quality modeling, there is additionally a significant body of work using relatively simple models, designed to improve our understanding of the climate system. This can improve general circulation models as well by helping us understand differences among GCM's, or between models and observations (see Held (2004)). These simple models often fall into one or more of the following classes: linearized systems, models with truncated vertical or horizontal resolution, asymptotically reduced systems of equations, and models with idealized physical parameterizations or boundary conditions.

However connecting simple theories or models to full GCM's is often difficult. This is primarily due to the extreme complexity of the climate system: full general circulation models must take into account a myriad of effects in order to forecast the climate accurately, while even the simplest atmospheric models can be chaotic and difficult to make progress in understanding (Lorenz, 1963). However the wide gulf between full GCM's and simple models is in part due to the fact that within the hierarchy of models discussed above, intermediate complexity models have been neglected. We argue that this class of models is of critical importance both for our understanding of the climate system, and for the improvement of full GCM's.

1.1 Intermediate Complexity Models

We introduce the notion of an intermediate complexity atmospheric model by example, by describing the model of Held and Suarez (1994). This model consists of the standard primitive equations dynamical core on the sphere, along with Newtonian cooling to a stably stratified radiative equilibrium profile and Rayleigh damping as the only physical parameterizations. The model was proposed as a benchmark for the systematic comparison of GCM dynamical cores, but produces a climatology which qualitatively reproduces the general features of the atmosphere, and has been useful for a number of modeling studies including Franzke (2002), Seager et al. (2003), Williams (2003), Kushner and Polvani (2004), Harnik and Chang (2004), and Franzke et al. (2004). Clearly the idealizations of diabatic and frictional processes in this model limit its applicability for study of many climate problems. However the model contains the essential elements needed for the study of dry baroclinic dynamics; the above studies focus on low frequency variability and the North Atlantic Oscillation (Franzke (2002); Franzke et al. (2004)), cyclone dynamics (Seager et al., 2003), equatorial superrotation (Williams, 2003), stratosphere-troposphere interactions (Kushner and Polvani, 2004), and jet width and barotropic waves (Harnik and Chang, 2004).

The specification of a stably stratified radiative equilibrium is a key assumption within the realm of dry dynamics. In order to examine the determination of the static stability of the atmosphere, one must consider a more complex model. Simulations with a similar dry model have been performed by Schneider (2004); this model relaxes instead to a strongly unstable radiative equilibrium profile, therefore allowing study of the influence of dry baroclinic eddies on the static stability. In order to handle the unstable radiative equilibrium, a simplified boundary layer scheme and convective adjustment are additionally necessary in Schneider's model.

However these models remains remote from full general circulation models, specifically since they contain no moist physics. Much of the additional physics within full GCM's, e.g., radiative transfer, convection, and clouds, relies on the humidity content of the atmosphere. We have thus developed an intermediate complexity moist GCM to fill the next level of complexity up in the hierarchy from the models of Held and Suarez (1994) and Schneider (2004).

The addition of moisture to a model such as Held and Suarez (1994) unfortunately involves a large addition of complexity. There are different choices available in how to handle this addition (as with all simplified models there are choices of which physical processes to include: the differences between the dry primitive equation models of Held and Suarez (1994) and Schneider (2004) illustrate this point well). In the construction of our intermediate complexity moist GCM, we strive for simplicity and reproducibility of results, but would additionally like our parameterizations to be compatible with full GCM physical parameterizations when possible. With these constraints in mind, we have adopted the path described below in developing a moist GCM.

With a moist atmosphere, an evaporative flux or source of moisture is required. We have chosen to have this flux come from an ocean surface below, rather than simply specifying the flux. If one wants the atmosphere still to perform all the energy transport a mixed-layer ocean is required, which calculates a prognostic surface temperature in order to conserve energy in the time mean. In order to run with a mixed layer, one must have a downward longwave radiation flux at the surface to complete the surface energy budget, which requires a more complicated radiative transfer model than Newtonian cooling. Therefore we utilize a gray radiation scheme, with optical depths specified as functions of latitude and height alone. This radiation scheme makes the model more modular with respect to other GCM parameterizations as well.

The use of gray radiative transfer suppresses any cloud- or water vapor-radiative feedbacks, thus significantly limiting the type of climate problems one can study with this model. However we see this approximation as key because, as described in more detail later, we can vary the moisture content of the atmosphere over a wide range without radiative feedbacks dominating. As described in Pierrehumbert (2002), water vapor has a plethora of effects on the Earth's climate. It is useful to study a model in which the radiative effects of water are suppressed to isolate the dynamical effects of water vapor on the climate.

In addition to the different radiation scheme, surface flux and convection schemes are additionally necessary with moisture. Further, with the gray radiation scheme, the atmosphere is heated strongly from below. Therefore, a boundary layer scheme is additionally necessary to prevent numerical instability close to the surface.

We have designed each of these parameterizations to be mathematically well-posed, in that they will converge to a unique solution as resolution is increased. We also try to minimize the number of empirical parameters in the model, so we can consider model atmospheres very different from our own, over a wide range of parameter space. We have also designed this model to be completely modular, i.e., it can be used as testing grounds for GCM parameterization schemes, e.g., cloud, radiation, or convection schemes. Additionally, the model and model description are presented in a manner that allows for easily reproducible results, so others can build on the results in this body of work.

1.2 Outline

A full description of the model and its associated parameterizations is given in Chapter 2. Additionally in Chapter 2, we provide a full nondimensionalization of the model, and give a complete list of the nondimensional parameters. In Chapter 3, we use the model to study the effect of moisture on midlatitude static stability and eddy length scales within the model. This chapter is joint work with Isaac Held and Pablo Zurita-Gotor, part of which appears in Frierson et al. (2005a). Then in Chapter 4, we study the effect of moisture on meridional fluxes of moist static energy. This chapter is also joint work with Held and Zurita-Gotor, and parts of this appear in Frierson et al. (2005b). In Chapters 5-7, we shift our focus to the tropics, and begin by considering a simpler mathematical model. We develop a simple model of the large scale dynamics of moisture and precipitation in the tropical atmosphere and present a full derivation of this model suitable for an applied mathematics audience in Chapter 5. In Chapter 6, we then use this to study the dynamics of "precipitation fronts," which mark the boundary between precipitating and non-precipitating regions in the model. These two chapters are joint work with Andy Majda and Olivier Pauluis, and parts of these chapters appear in Frierson et al. (2004). In order to study the tropics within the moist GCM, we develop a convection scheme that is based on the same principles as the treatment of moisture in Chapter 5, but is suitable for use in models with full vertical resolution. In Chapter 7 we present this idealized convection scheme, and study the effect of convection on the zonally averaged tropical circulation. Parts of this chapter appears in Frierson (2005). We conclude in Chapter 8. What follows in the remainder of this chapter is an introduction to the problems we study in Chapters 3-7. We provide an introduction to theories for midlatitude static stability, eddy scale, energy fluxes, simple models of moisture in the tropics, and the effect of convection on tropical circulations.

1.3 Midlatitude Static Stability

An understanding of the tropospheric static stability in midlatitudes, although fundamental to any theory of the general circulation, has proven to be difficult to achieve. As in Stone (1972), many theories take the form of expressions for the horizontal component of the large-scale baroclinic eddy sensible heat flux, supplemented by the assumption that the ratio of the vertical to the horizontal components is such as to align the total flux along the dry isentropes in the free troposphere (or, as in Green (1970), at some angle between the horizontal and the isentropic slope). The balance between the radiative destabilization and the upward sensible heat flux then determines the stability.

Held (1982) provide a slightly different framework for the study of this problem, by thinking of the tropopause height and the tropospheric static stability as being simultaneously determined by satisfying two constraints, one radiative and one dynamical. The radiative constraint between the tropospheric lapse rate and the height of the tropopause is generated by a standard radiative-convective model in which the lapse rate is an input parameter. For the dynamical constraint, Held (1982) use a theory for the depth to which unstable quasi-geostrophic baroclinic eddies can penetrate into a stably stratified atmosphere in the presence of vertical shear. Thuburn and Craig (1997) perform tests of this theory using a comprehensive moist GCM, and conclude that the radiative constraint with appropriate absorber distributions is useful in explaining the relation between the tropopause height and static stability, but that the dynamical constraint in Held (1982) is not. However, Schneider (2004) shows that a related dynamical constraint does help explain the behavior of an idealized dry general circulation model. This difference in conclusions is related, at least in part, to the differences in the definition of the dynamical constraint, but potentially also to the differences in the underlying models. The work of Haynes et al. (2001) also supports the view that mixing of PV by baroclinic eddies shapes the extratropical tropopause in idealized dry models.

An alternative perspective on midlatitude static stability is that it is in fact controlled by moist convection, as in the tropics (Emanuel (1988); Juckes (2000)). The following picture is a simplified version of Juckes' argument. In Earth-like conditions, midlatitude eddies typically convect up to the tropopause above the region of low level warm, moist, poleward moving air near the surface, and have approximately neutral moist stability in this sector. Ignoring horizontal temperature gradients near the tropopause, the difference in moist static energy between surface and tropopause in the non-convecting regions is then given by the difference in near surface moist static energy between the warm and cold sectors of the eddy. The near surface RMS moist static energy in midlatitude eddies is then the appropriate measure of the moist stability of these dry regions. Equivalently, the mean dry stability is greater than needed to maintain neutral stability given mean low level temperature and water vapor content, but it is just sufficient to maintain neutrality given values of temperature and water vapor in the typical warm sectors of midlatitude storms. The claim is that baroclinic eddies are unable to stabilize the troposphere efficiently enough to prevent convection in the warm sectors of storms, at least for realistic strengths of radiative destabilization.

Our simplified moist GCM provides a useful framework for testing this picture. Since we have the ability to vary the moisture content by orders of magnitude without radiative effects dominating, we can diagnose whether convection is always fundamental in the determination of the static stability or whether there is a regime in which large-scale theories are sufficient. The "dry limit" of this model (no atmospheric moisture) is also illuminating in this regard. There is nothing inherent to the picture described above that limits its applicability to moist atmospheres.

1.4 Midlatitude Eddy scale

In classical theory, the length scales of baroclinic eddies are thought of as determined by the most unstable mode of the standard linear baroclinic instability problems of Eady or Charney. In the Eady model, this length scale is proportional to the internal radius of deformation, $L_D = \frac{NH}{f}$, where N is the buoyancy frequency, H is the depth of the fluid, and f is the local value of the Coriolis parameter. In the Charney problem, the length scale depends on whether one is in the shallow eddy or deep eddy regime, the transition from the former to the latter occurring when the isentropic slope exceeds $\frac{H\beta}{f}$. Assuming that the deep eddy regime is the only physically relevant one, the most unstable wavelength is once again proportional to the familiar radius of deformation, with H now proportional to the scale height. The dry static stability of the atmosphere (measured by the buoyancy frequency N) is, from this perspective, a key ingredient in any theory for eddy length scales.

Simulations of two-dimensional turbulence develop an inverse cascade of energy to large scales, and the energy containing eddy scale is determined, not by the injection scale, but by whatever factor stops the cascade. In particular, an environmental vorticity gradient can stop the cascade (Rhines, 1975). In the homogeneous turbulence simulations of quasi-geostrophic baroclinically unstable flows described by Held and Larichev (1996), the eddy scale is clearly determined by this process, resulting in an eddy scale that is proportional to the Rhines scale, $L_\beta = \sqrt{v_{RMS}/\beta}$, where v_{RMS} is the square root of the eddy kinetic energy. Full moist GCM simulations described by Barry et al. (2002) provide some evidence that the Rhines scale is also relevant in this more realistic context, even though it is unclear whether anything resembling a well-defined inverse cascade exists in these simulations. In contrast, Schneider (2004) has argued that it is difficult to separate the radius of deformation and the Rhines scale in models in which the static stability in free to adjust (unlike the QG turbulence models described above). The claim by Barry et al. (2002) that the Rhines scale fits their model results better than does the radius of deformation evidently implies that one can separate these scales in their moist GCM.

If the Rhines scale is the relevant scale, then the effect of the static stability on this scale is indirect. A decrease in static stability, for example, could increase the eddy kinetic energy and thereby increase the eddy scale. This is what occurs in the QG homogenous theory of Held and Larichev (1996), for example.

Our concern here is with the effects of latent heat release on eddy scales. Expectations based on linear theory are described by Emanuel et al. (1987), who study a moist Eady model in which regions of upward motion (updrafts) are assumed to be saturated. In the limit of moist neutrality in the updrafts, they find that the width of the updrafts collapses to zero, and that the total wavelength of the shortwave cutoff is roughly divided by two. The dry static stability continues to control the scale of the unstable modes in this limit. The same result would be obtained by considering a single, averaged static stability roughly halfway between the dry and moist values relevant in the downdraft and updraft.

From a rather different perspective, Lapeyre and Held (2004) attempt to extend the results for dry baroclinic QG turbulence to the moist case. For weak latent heating, the solutions can be qualitatively understood in terms of a reduced static stability. However, the eddy scale in this turbulent model can increase as one increases the moisture content, since the flow can become more energetic, and, as alluded to above, the eddy scale can expand due to a more extensive inverse cascade.

We can investigate the role of the static stability and moisture in the determination of eddy scales within our moist GCM by varying the moisture content of the atmosphere. On the one hand, we have found it difficult to relate our results to the body of work outlined above. On the other hand, the results suggest that there are very strong and, we suspect, simple constraints on the midlatitude eddy scale.

1.5 Energy Fluxes

There are several schools of thinking regarding the effect of moisture on midlatitude atmospheric circulations. Firstly, moisture serves as an additional source of available potential energy for baroclinic eddies; therefore it is possible that with increased moisture content baroclinic eddies may increase in strength. On the other hand, in terms of the vertically integrated heat budget of the atmosphere, poleward moisture fluxes serve to decrease temperature gradients equivalently to dry static energy fluxes. If baroclinic eddies are thought of as working off of these temperature gradients, with increased moisture concentration (and increased meridional fluxes of moisture) one might expect a decrease in strength of baroclinic eddies. Closely related to the change in eddy strength are the meridional fluxes of energy, consisting of both dry static energy transports and moisture fluxes. The moist static energy fluxes are of fundamental importance because these determine to a large extent the meridional temperature gradients within the troposphere.

Manabe and coauthors have studied the changes in energy fluxes under different climate model configurations in several studies. For instance, when the ocean component was removed from a coupled GCM and replaced by a mixed layer surface, the total (atmosphere plus ocean) energy fluxes were found to be surprisingly robust (Manabe et al., 1975); the atmospheric energy transport increases to compensate the loss of ocean heat flux almost identically. When mountains are removed from a similar atmosphere-only GCM, the total moist static energy fluxes show little change, even though the partition into stationary eddy and transient eddy fluxes are vastly different Manabe and Terpstra (1974). When continental ice sheets are added to a GCM to simulate an ice age climate, the total moist static energy fluxes are again found to be quite similar (Manabe and Broccoli, 1985). In the ice sheet experiment, despite an increase in the equator-to-pole temperature gradients and dry static energy flux, decreases in moisture fluxes cause the total moist static energy flux to change by less than 0.4 PW. Additionally Manabe et al. (1965) study the removal of moisture from a full GCM. Again the moist static energy fluxes are found to be relatively invariant (15% increase in maximum flux from the dry to the moist simulation); there is a compensating increase in dry static energy fluxes as the moisture fluxes are removed.

Stone (1978b) give a theoretical framework for understanding the relative invariance of the atmospheric moist static energy fluxes (or total atmosphere plus ocean heat fluxes) in these studies. First they show that the structure of the moist static energy fluxes are close to that implied by flat OLR. This structure is seen in observations as well the GCM studies. They additionally show that structure in the OLR function projects only weakly onto the fluxes: essentially only the magnitude of the fluxes is sensitive to the shape of the OLR profile. Stone additionally claims that the similarity of the magnitude of the fluxes to the flux implied by flat OLR is the reason for invariance of fluxes in the above GCM studies.

From another perspective, the determination of moist static energy fluxes are often studied within a diffusive framework (flux proportional to the gradient). This body of work includes the energy balance model studies of Budyko (1969) and Sellers (1969), and the diffusivity scaling theories of Stone (1972), Green (1970), Held and Larichev (1996), Haine and Marshall (1998), and Barry et al. (2002). The local diffusivity argument is evaluated in the dry case by Pavan and Held (1996). There are alternatives to the diffusive framework: for instance baroclinic adjustment theories predict the temperature structure of the atmosphere (that which neutralizes some measure of baroclinic instability) without references to the fluxes required to give this structure.

We evaluate these theories within our moist GCM by varying the water vapor content of the atmosphere, and studying the changes in moist static energy fluxes (and their partition into dry static energy fluxes and moisture fluxes) as moisture content is changed.

1.6 Simple Models of Moisture and Precipitation in the Tropics

Due to the increased moisture content and the primary importance of latent heating in driving the circulations there, moisture is clearly of fundamental importance in the tropics. However many simple theories for the large-scale tropical flow are essentially dry theories: they assume a distribution for the latent heating and calculate the dry atmospheric response to this. Two-layer models using this principle have been successful in simulating the steady Walker circulation, and transient response to heating anomalies (Gill, 1980). Since diabatic heating in the tropics must be balanced thermodynamically with vertical motion (due to the weak temperature gradients in the tropics), these models essentially calculate the rotational part of the flow given the divergent part.

Calculating the divergent part of the flow from sea surface temperatures or surface fluxes, however, is much more difficult. This is, to a large extent, due to the influence of moisture. Latent heating is the dominant diabatic term in moist regions of the tropics, and thus can be considered to drive the flow. However moisture is advected by the large-scale flow as well. An integrated treatment of moisture must be included into any theory for the full large-scale dynamics of tropics.

Another primary role of moisture is to reduce the effective static stability of the atmosphere. Condensational heating warms saturated parcels as they ascend, giving them additional buoyancy. The tropics as a whole are close to zero moist stability (Xu and Emanuel, 1989). Neelin and Held (1987) use the concept of moist stability and postulate that the "gross moist stability" of the tropical atmosphere is small and positive everywhere. Assuming a maximum value for this gross moist stability, and assuming the surface humidity content is determined by the sea surface temperatures, Neelin and Held (1987) are able to simulate the qualitative shape of the tropical convergence zones and their seasonal movement. There has been much subsequent work based on the principle of gross moist stability within simple models. The Quasi-equilibrium Tropical Circulation Model (QTCM) of Neelin and Zeng (2000) is an example of a two-vertical-mode AGCM that is based on the principle of small yet positive gross moist stability.

Another class of idealized models that have been useful for the study of tropical circulations are asymptotically truncated models. A prominent one of these is the weak temperature gradient system (Sobel et al., 2001), a balanced model that filters gravity waves and is analogous to the quasi-geostrophic system in midlatitudes. Bretherton and Sobel (2002) used a simplified QTCM framework with the weak temperature gradient approximation to study steady Walker cell solutions.

An alternative perspective to understanding tropical convergence/divergence regions is that of Lindzen and Nigam (1987). This theory states that sea surface temperatures drive pressure gradients within the boundary layer which must be balanced by friction in this layer. The convergence zones are thus directly determined by the SST profile locally. This is in contrast to the theory of Neelin and Held (1987), where the sea surface temperatures remotely can have an effect on the dynamics.

While the studies of Bretherton and Sobel (2002), Neelin and Held (1987), and Lindzen and Nigam (1987) provides useful frameworks for understanding the steady Walker circulation (and we point out that it is not fully clear to what extent any of these theories are accurate in the real atmosphere), the tropical circulation is by no means steady. The tropics are made up of envelopes of convecting and non-convecting regions on an enormous range of scales. The most prominent of these envelopes is the Madden-Julian Oscillation (Madden and Julian (1971); Madden and Julian (1994)), a 30-60 day eastward propagating wave of suppressed and enhanced convection.

We develop our own simplified model of the tropics in Chapter 5. This is similar to the QTCM, but we provide a full derivation from the Boussinesq equations using a Galerkin truncation to two vertical modes, a framework appropriate for the applied mathematics community. Then in Chapter 6 we present a theory for "precipitation fronts," which mark the border between convecting and non-convecting regions in the tropics. We develop a theory for the movement of these fronts, which provides a first step to understanding the movement of precipitation regions within the tropical atmosphere.

1.7 The Effect of Convection on Tropical Circulation

Our picture of the role of moist convection in the tropics is continually changing with the addition of new observations in this relatively data-sparse region. Many of these recent observations have provided compelling empirical tests for the theoretically based aspects of convection schemes, and the choice of parameters therein. For instance, the study of Brown and Bretherton (1997) demonstrated the correlation between boundary layer moist static energy and free tropospheric temperature, as postulated in the quasi-equilibrium hypothesis, used in many convection schemes. However, the correlations they found were significantly weaker than predicted by the strict quasi-equilibrium hypothesis, which states that convection keeps some measure of instability exactly unchanged as convection occurs. The study of Bretherton et al. (2004) examines the correlations between relative humidity and precipitation in the tropics, and show that these quantities are indeed well-correlated. However, they find that the implied convective relaxation times are larger than those typically used in models such as the Betts-Miller scheme; they find an approximate relaxation timescale of 12-16 h, whereas the Betts-Miller scheme typically utilizes a much shorter relaxation times.

Motivated by these observational findings, we develop a simplification of the Betts-Miller convection scheme, and use this to study the zonally averaged climate of the tropics within our moist GCM. We focus primarily on the effect of convection on the Hadley circulation and the precipitation distribution. Current general circulation models and their convection schemes typically have difficulty in simulating precipitation distributions within the ITCZ and near the equator (Mechoso and coauthors, 1995); in particular most GCM's have a tendency to form a "double ITCZ" that is not observed. There is relatively little theoretical understanding of the reasons for these deficiencies; this is, in part, due to the fact that there has been relatively little study of the zonally averaged tropical circulation within models that bridge the gap between simple theories and full GCM's.

There are several notable examples of studies of the zonally averaged tropical circulation in GCM's of full vertical resolution with moisture. For instance, Numaguti (1993) studies the tropical precipitation distribution and the Hadley circulation within an idealized moist GCM over an aquaplanet lower boundary. This paper emphasizes the importance of the distribution of evaporation for the Hadley circulation and the large sensitivity of the precipitation to small changes in evaporation. They additionally find the convection scheme and the moist static stability plays an important role in the determination of the Hadley circulation system. Hess et al. (1993) obtain similar results in an aquaplanet GCM; this study along with Numaguti (1995) examine the sensitivity of the ITCZ location and strength to SST distribution as well.

From a different perspective, Satoh (1994) presents a theory for the moist Hadley circulation within an axisymmetric aquaplanet model with idealized parameterizations of moisture and radiation. They find that the Hadley cell strength in this model is controlled by the radiative cooling in the dry subtropics. The subsidence determines the strength of the cell, implying the gross moist stability of the atmosphere in the tropics must adjust to satisfy energy and mass balance within the deep tropics. In this sense, convection does not strongly influence the zonally averaged circulation, as the control is limited to the subtropics where no convection occurs; their sensitivity tests to convective parameterization confirms a lack of sensitivity to convective parameterization. However, this theory would not necessarily carry over into an atmosphere in which the subtropics are not completely dry, as clearly is the case in our atmosphere. Our model provides a useful realm for the test of Satoh's theory in a model with axial eddies, and a consistent energy balance and treatment of moisture.

Chapter 2

An Intermediate Complexity Moist General Circulation Model

2.1 Introduction

As mentioned in Chapter 1, the model described herein can be thought of as an extension of the dry model of Held and Suarez (1994) to include latent heat release. The Held and Suarez (1994) model consists of the standard primitive equation dynamical core, along with Newtonian cooling to a specified radiative equilibrium profile, and Rayleigh damping to represent the surface boundary layer. In designing an idealized moist general circulation model, our goal is also to create a framework to which we could sequentially add the various components of a full atmospheric GCM, and to have some flexibility in the choice of a lower boundary condition. To this end we have included an explicit boundary layer model and replaced the Newtonian cooling with a very simple gray radiative model that predicts upward and downward fluxes. In this study we assume that the surface consists of a "mixed-layer ocean," a slab of water of specified heat capacity with no horizontal transport. The model is then energetically closed, which simplifies some of our analysis, especially in our study of the energy transports in Chapter 4.

We have tried to choose a boundary layer model which allows us to pass to a physically interesting dry limit as the moisture in the atmosphere is reduced to zero. The resulting dry model is very different from the sort of model described by Held and Suarez (1994), in that the atmosphere is destabilized very strongly by surface heating, instead of being relaxed to a statically stable radiative equilibrium profile. The dry model is additionally different than that of Schneider (2004): although both of these models use strongly unstable radiative equilibrium profiles, Schneider's "convection" scheme typically relaxes to a stable lapse rate and has no moisture. In his simulations relaxing to the dry adiabatic lapse rate, the boundary layer remains capped at a specified depth and the dry convection scheme performs all the mixing.

We see nothing in our physics formulation that prevents one from computing the solution within other systems of equations or alternate dynamical cores. For instance, we have used these physical parameterizations within a non-hydrostatic model in the study of Garner et al. (2005). Our hope is that the model is well-posed in the sense that the solutions converge to a well-defined limit as resolution is increased, even when deep convection is resolved within the non-hydrostatic model.

In this chapter we present a complete description of this GCM, which includes descriptions of the boundary conditions, radiation scheme, surface fluxes, boundary layer scheme, and our treatment of moisture. As we do not use our simplified Betts-Miller convection scheme until Chapter 7, we defer discussion of this part of the model until that chapter, where we present a full description of this scheme along with tests of the parameters therein.

2.2 Boundary Conditions

The lower boundary condition is an aquaplanet (ocean-covered) surface with no topography. For the ocean surface, we choose an energy-conserving slab mixed layer with shallow depth rather than fixed sea surface temperatures. The mixed layer has a specified heat capacity and single temperature which adjusts satisfying the following equation:

$$C\frac{\partial T_s}{\partial t} = R_{SWd} - R_{LWu} + R_{LWd} - LE - SH \tag{2.1}$$

where C is a specified heat capacity, T_s is the local surface temperature, E is the evaporative flux, SH is the sensible heat flux, and R_{SWd}, R_{LWu}, R_{LWd} are the downward shortwave, upward longwave flux, and downward longwave radiative fluxes respectively. When running over a mixed layer, all the poleward energy transport is performed by the atmosphere (there are no implied oceanic fluxes), making energy budgets easier to analyze. The standard value of the heat capacity parameter is $10^7 JK^{-1}m^{-2}$, corresponding to a depth of 2.4 m.

2.3 Radiation Scheme

Because we are using surface fluxes to drive the slab ocean temperatures we require a radiation module that predicts upward and downward fluxes and not simply heating rates as in the Newtonian cooling scheme commonly used in idealized models. We choose gray radiative transfer with specified absorber distribution as the simplest alternative. Therefore, while water vapor is a prognostic variable in this model, it does not affect the radiative transfer. We regard this as a key simplification; it allows us to study some of the dynamical consequences of increasing or decreasing the water vapor content in isolation from any radiative effects. There are no clouds in this model. Radiative fluxes are a function of temperature only.

We first specify incoming solar radiation at the top of the atmosphere, a function of latitude only. The functional form of the radiation mimics the observed annual and zonal mean TOA net shortwave flux. There is no seasonal cycle or diurnal cycle in the model. The solar flux is

$$R_{sol} = R_{sol0}(1 + \Delta_{sol} p_2(\theta)) \tag{2.2}$$

where

$$p_2(\theta) = \frac{1}{4}(1 - 3sin^2(\theta)) \tag{2.3}$$

is the second Legendre polynomial, which integrates to zero over the sphere, R_{sol0} is the global mean incident solar flux (with standard value of $1360Wm^{-2}$), and Δ_{sol} is the solar insolation gradient parameter that is varied in order to drive the system to larger or smaller meridional temperature gradients.

In the studies presented in Chapters 3-4, we have excluded solar absorption in the atmosphere for simplicity, but also because of a desire to accentuate the strength of the radiative destabilization of the atmosphere, so to more clearly differentiate this model from those such as HS in which the radiative destabilization is very weak. However, as we demonstrate later, this simplification leads to an overly strong hydrologic cycle. This does not detract from our results concerning midlatitude eddies and energy fluxes in Chapters 3 and 4, but is necessary to simulate a realistic tropical climate. Therefore in our studies of tropical convection and the Hadley circulation in Chapter 7, we consider some solar absorption.

We prescribe the solar absorption by specifying short wave optical depths as a function of height. The functional form is

$$\tau_{SW} = \tau_{SW0}(\frac{p}{p_{surf}})^4 \tag{2.4}$$

The optical depth at the surface is τ_{SW0}, which also determines how much solar radiation is absorbed by the atmosphere. This combined with the surface albedo parameter A, which we consider to be uniform across the domain, determine how much radiation is absorbed by the surface. As we will see, the total amount of shortwave radiation that is absorbed by the surface is

$$R_{SWsurf} = (1 - A)R_{solar}exp(-\tau_{SW0}) \tag{2.5}$$

If we use the value of $\tau_{SW0} = .2$, the amount absorbed by the atmosphere is

$$R_{SWatmos} = R_{solar}(1 - exp(-\tau_{SW0})) \tag{2.6}$$

which gives a fraction of .18 (corresponding to observations). If we additionally specify $A = .38$, the fraction of solar radiation that is absorbed by the surface is .51, again corresponding to observations. These are the standard values utilized in Chapter 7. When no solar absorption within the atmosphere is used, an albedo of $A = .31$ is required to have the same net solar absorption by the planet; this parameter set is used in Chapters 3-4.

In the infrared, we specify the atmospheric optical depths as a function of latitude and pressure to approximate the effects of water vapor. The surface values are given the form

$$\tau_0 = \tau_{0eq} + (\tau_{0pole} - \tau_{0eq})sin^2(\theta) \tag{2.7}$$

The structure with height consists of a quartic part and a linear part with pressure:

$$\tau = \tau_0(f_{lin}(\frac{p}{p_{surf}}) + (1 - f_{lin})(\frac{p}{p_{surf}})^4) \tag{2.8}$$

The quartic term approximates the structure of water vapor, the chief greenhouse gas, in the atmosphere. If we use the quartic term in isolation, the stratospheric

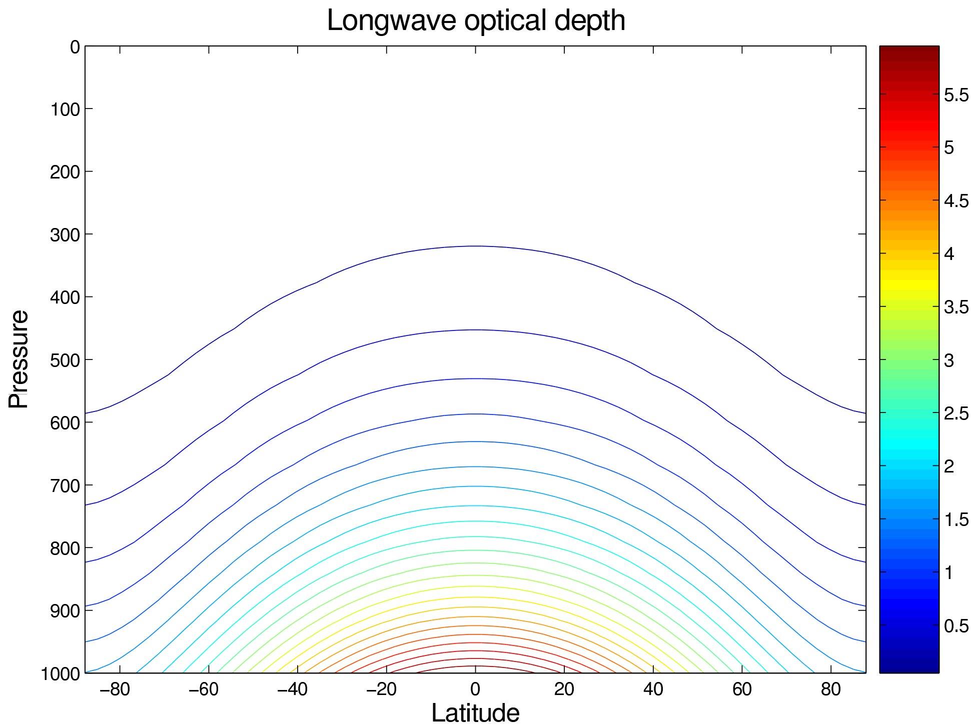

Figure 2.1: Optical depth for longwave radiation.

radiative relaxation time becomes very long, which is both unrealistic and awkward from the perspective of reaching equilibrium within a reasonable length integration. The linear part in our absorber distribution is included to reduce the stratospheric relaxation times. The stratosphere is clearly one of the more unrealistic aspects of this model. The longwave optical depths are depicted in Figure 2.1.

The standard two-stream approximation is used to calculate the radiative fluxes. The radiative equations we integrate are

$$\frac{dU}{d\tau} = (U - B) \tag{2.9}$$

$$\frac{dD}{d\tau} = (B - D) \tag{2.10}$$

where U is the upward flux, D is the downward flux, and $B = \sigma T^4$. The diffusivity factor, commonly taken to equal 1.6, has been folded into the optical depth. The boundary condition at the surface is $U(\tau(z = 0)) = \sigma T_s^4$ and at the top of the atmosphere is $D(\tau = 0) = 0$. The radiative source term in the temperature equation is

$$Q_R = -\frac{1}{c_p \rho} \frac{\partial (U - D)}{\partial z} \tag{2.11}$$

Our choice of a parameter set for the radiation scheme in our control integration is listed in Table 2.1.

Parameter	Explanation	Control Value
R_{sol0}	Solar constant	$1360\ W\ m^{-2}$
A	Albedo	.31
Δ_{sol}	Latitudinal variation of SW radiation	1.4
τ_{eq}	Longwave optical depth at the equator	6
τ_{pole}	Longwave optical depth at the pole	1.5
f_{lin}	Linear optical depth parameter	.1
n_τ	Power-law dependence of $\tau(p)$	4
σ	Stefan-Boltzmann constant	$5.6734 \times 10^{-8}\ W\ m^{-2}\ K^{-4}$

Table 2.1: Complete radiation parameter list

2.3.1 Pure Radiative Equilibrium Calculations

We have performed pure radiative equilibrium calculations (with dynamics and other physics suppressed) using the gray radiation scheme. Figure 2.2 contains plots of the radiative equilibrium temperature, and Figure 2.3 contain plots of potential temperature. The potential temperature reveals that the profiles are locally unstable up to approximately 500 mbar for nearly all latitudes for this choice of parameters. However, the "level of zero buoyancy" for dry ascent from the surface is vastly different for different latitudes: this ranges from above 200 mbar at the equator, to only slightly

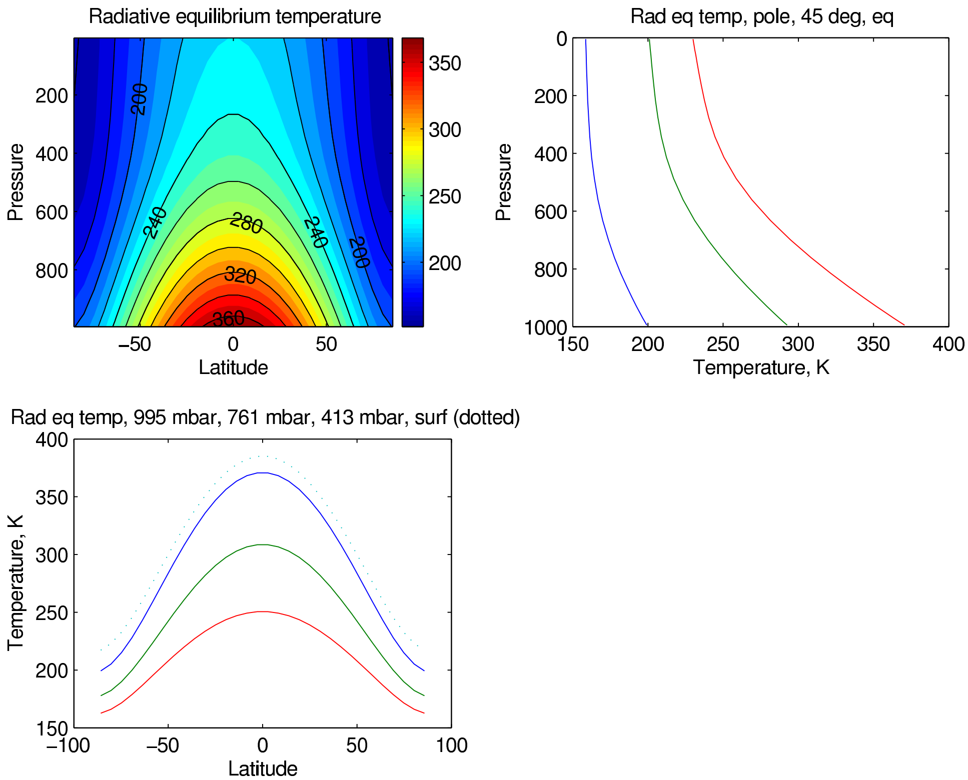

Figure 2.2: Radiative equilibrium temperature.

above 500 mbar at the pole. Another interesting point is that there is a large temperature jump between the surface and the lowest model layer, on the order of 15 K for all latitudes. This discontinuity is smoothed by sensible heat fluxes in simulations with the full GCM.

2.4 Surface Fluxes

We utilize standard drag laws, with drag coefficients that are equal for momentum, temperature, and water. For the surface stress, sensible heat flux, and evaporation, respectively, we have

$$\tau = \rho C|v|\mathbf{v} \tag{2.12}$$

$$H = \rho c_p C|v|(\Theta - \Theta_s) \tag{2.13}$$

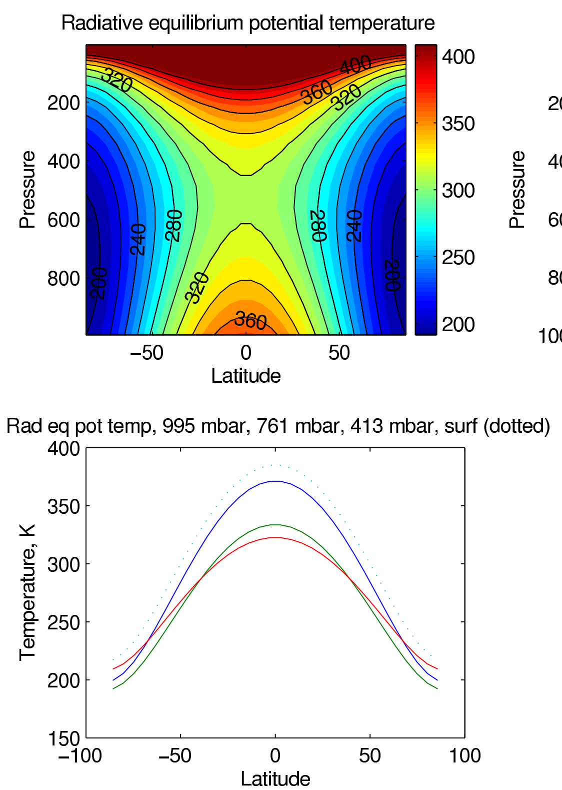

Figure 2.3: Radiative equilibrium potential temperature.

$$E = \rho C|v|(q - q_s) \tag{2.14}$$

where c_p is the heat capacity at constant pressure, Θ_s is the surface potential temperature and q_s is the saturation specific humidity at the surface temperature, while $\mathbf{v}$, ρ, Θ and q are the horizontal wind, density, potential temperature and specific humidity evaluated at the lowest model level.

The drag coefficient is calculated according to a simplified Monin-Obukhov similarity theory. We take a brief aside to explain the basic elements of this commonly used theory for surface fluxes.

2.4.1 Monin-Obukhov Theory

Monin-Obukhov Similarity (MOS) theory is the method used by most general circulation models to compute surface fluxes. It is valid in the "surface layer" where the fluxes are assumed constant. This theory has a great deal of support from observations, within a depth of 10 meters or so. It is for this reason that most GCM's have their bottom layer within 10 m: so MOS can be applied accurately for surface fluxes.

The only relevant parameters in this theory are assumed to be the surface stress, the surface buoyancy flux, and the density. A velocity scale is created from the surface stress and the density. Similarly, a buoyancy scale is created from the buoyancy flux, the velocity scale, and the density. A length scale is created from the buoyancy and velocity scales in the proper ratio.

In the neutral case, the wind shear is assumed to be a function of the stress (i.e., the velocity scale), and the height above the surface.

$$\frac{\partial u}{\partial z} = \frac{u_*}{\kappa_{VK} z} \tag{2.15}$$

The constant κ_{VK} in this relation is the von Karman constant, which is a nondimensional universal constant that takes the value of 0.40.

Equation 2.15 implies a logarithmic velocity profile within the surface layer under neutral conditions (known as the "law of the wall"):

$$u(z) = \frac{u_*}{\kappa_{VK}} ln(\frac{z}{z_0}) \tag{2.16}$$

The constant z_0 in this relation is the "roughness height" and is a function of the surface type. Physically this height is the level at which the wind is assumed to go to zero. Some typical values of the roughness height for various surface types are

$$\begin{aligned}
z_0 &= 0.0002\ m \text{ open water} \\
z_0 &= 0.005\ m \text{ flat land, ice} \\
z_0 &= 0.03\ m \text{ grass or low vegetation} \\
z_0 &= 0.1\ m \text{ low crops} \\
z_0 &= 0.5\ m \text{ forest} \\
z_0 &= 2.0\ m \text{ city center, large forest}
\end{aligned}$$

The method for solving for surface fluxes, under neutral conditions, is as follows. Given the winds at a certain height, and the roughness height, we can invert the law of the wall for the velocity scale. Then the surface drag is obtained from this scale. This procedure amounts to solving the following relations:

$$u_* = \frac{\kappa_{VK} u(z)}{ln(\frac{z}{z_0})} \tag{2.17}$$

$$\tau = \rho_s u_*^2 \tag{2.18}$$

Using the drag law equation for the stress (equation (2.12)), we can write the drag coefficient as

$$
\begin{aligned}
C(z) &= \frac{u_*^2}{(u(z))^2} \\
&= \frac{\kappa_{VK}^2}{ln(\frac{z}{z_0})^2}
\end{aligned}
\tag{2.19}
$$

This completes the theory for the neutral limit, and we can proceed to the case where the buoyancy flux is non-zero, i.e., $b_* \neq 0$. Now we must use the Monin-Obukhov length, defined as

$$L = -\frac{u_*^2}{\kappa_{VK} b_*} \tag{2.20}$$

$L > 0$ under stable conditions (when there is heat flux into the surface). For heights less than the Monin-Obukhov length, the turbulence is primarily mechanically driven, and above the turbulence is buoyancy driven.

The key assumption in the case where the buoyancy flux is nonzero is that the profiles additionally depend on the nondimensional height $\zeta = z/L$, i.e., the height divided by the Monin-Obukhov length. This is accomplished by specifying a function $\Phi_m(\zeta)$ such that

$$\frac{\kappa_{VK} z}{u_*} \frac{\partial u}{\partial z} = \Phi_m(\zeta) \tag{2.21}$$

Similarly, we assume that the buoyancy profile is given by

$$\frac{\kappa_{VK} z}{b_*} \frac{\partial b}{\partial z} = \Phi_b(\zeta) \tag{2.22}$$

As above, integration of this equation will produce another roughness length constant that must be specified. The functions Φ are derived empirically. For reference, the

GFDL atmospheric general circulation model AM2 uses the following functions:

$$\Phi_m = (1 - 16\zeta)^{-\frac{1}{4}} \text{ (unstable case)} \tag{2.23}$$

$$\Phi_b = (1 - 16\zeta)^{-\frac{1}{2}} \text{ (unstable case)} \tag{2.24}$$

$$\Phi_m = \Phi_b = 1 + 5\zeta \text{ (stable case)} \tag{2.25}$$

The functions above are considered to be appropriate for $-5 < \zeta < 1$. Our simplifications of the MOS scheme consists of simplifications to these functions.

The drag coefficients and velocity and buoyancy scales can be found from the above expressions, but this takes some calculation. One can write the following consistency equation:

$$\frac{gz(s_v(z) - s_v(0))}{s_v(0)u(z)^2} = \zeta \frac{F_b(\zeta) - F_b(\zeta z_b/z)}{(F_m(\zeta) - F_m(\zeta z_0/z))^2} \tag{2.26}$$

where $s_v = c_p T_v + gz$ is the virtual dry static energy, with T_v the virtual temperature. This equation, which the left hand side is not a function of the MOS theory (this is known as the bulk Richardson number), can be solved iteratively for ζ. The following can be computed given ζ:

$$u_* = \frac{\kappa_{VK}|u(z)|}{F_m(\zeta) - F_m(\zeta z_0/z)} \tag{2.27}$$

$$b_* = \frac{\kappa_{VK}(b(z) - b(0))}{F_b(\zeta) - F_b(\zeta z_b/z)} \tag{2.28}$$

$$C_m = \frac{\kappa_{VK}^2}{(F_m(\zeta) - F_m(\zeta z_0/z))^2} \tag{2.29}$$

$$C_b = \frac{\kappa_{VK}^2}{(F_m(\zeta) - F_m(\zeta z_0/z))(F_b(\zeta) - F_b(\zeta z_b/z))} \tag{2.30}$$

where $F_m(\zeta) = \int \zeta^{-1}\Phi_m d\zeta$ and the corresponding expression for $F_b(\zeta)$.

2.4.2 Our Simplified Monin-Obukhov Similarity Theory

We utilize a simplified version of MOS theory to calculate drag coefficients. First, we treat the unstable case as if neutral ($\Phi = 1$ for $\zeta < 0$). Therefore for unstable cases, we can calculate the drag coefficient analytically from equation (2.19). This simplification is important for numerical calculations as well: the typical functional forms used on the unstable side are not solvable analytically, and therefore require iteration to produce a solution.

On the stable side, we utilize a stability function of $\Phi = 1 + \zeta$ (for $\zeta > 0$). Again this form requires no iteration to obtain a solution for drag coefficients and velocity/buoyancy scales. With this function, the drag coefficient is reduced with increased surface stability, becoming close to zero for $Ri > 1$.

Using the above specifications of Φ, the drag coefficient obtained from this simplified MOS theory can be written compactly as:

$$C = \kappa_{VK}^2 \left(ln\frac{z}{z_0} \right)^{-2} \left(1 + max(Ri, 0) \frac{(1 - \frac{z_0}{z})}{Ri(1 - \frac{z_0}{z}) - 1} \right)^{-2} \tag{2.31}$$

where κ_{VK} is the von Karman constant, z is the height of the lowest model level, z_0 is the surface roughness length, and $Ri = \frac{gz(s_v(z) - s_v(0))/s_v(0)}{|v(z)|^2}$ is a bulk Richardson number evaluated at the lowest model level, with g the gravitational acceleration and s_v the virtual dry static energy.

We additionally utilize equal roughness lengths for heat, momentum, and water vapor: $z_0 = 3.21 \times 10^{-5}\ m$. This gives a drag coefficient $C_D = .001$ when the winds are specified at $z = 10\ m$ in unstable or neutral situations. We use zero "gustiness" velocity in this model, so that the surface fluxes are allowed to approach zero over small surface winds.

2.5 Boundary Layer Scheme

The boundary layer depth h is set to the height where the bulk Richardson number described in the section above exceeds a critical value. To agree with the surface flux formulation, this is chosen to be the same value as that at which the surface fluxes approach zero when it is achieved at the lowest model level ($Ri = 1$).

Diffusion coefficients within the boundary layer are calculated in accordance with the simplified Monin-Obukhov theory used for the drag coefficient. We match the fluxes to the fixed-flux surface layer below, which is defined as a specified fraction f of the boundary layer depth. The fluxes then go to zero at the boundary layer depth with the following functional forms for diffusivity (Troen and Mahrt, 1986):

$$K = \frac{\kappa_{VK}\sqrt{C}u_s z}{1 - max(Ri_s, 0)\frac{\kappa_{VK}z}{z_s\sqrt{C}}} \text{ for } z < fh \tag{2.32}$$

$$K = \left(\frac{\kappa_{VK}\sqrt{C}u_s z}{1 - max(Ri_s, 0)\frac{\kappa_{VK}fh}{z_s\sqrt{C}}}\right)\left(1 - \frac{z - fh}{(1-f)h}\right)^2 \text{ for } fh < z < h \tag{2.33}$$

where the subscript s denotes the quantity evaluated at the lowest model level, and C is the drag coefficient calculated from equation (2.19). These diffusion coefficients are used for momentum, dry static energy, and moisture.

The boundary layer scheme is key in our simulations with no water vapor (the "dry limit"); in this case the boundary layer scheme provides all of the convective mixing. The model is sensitive to the critical Richardson number parameter in the dry limit. Increasing its value allows more penetrative convection, modifying boundary layer depths and affecting the dry static energy profiles. However, a study of the effects of different choices of this parameter on our results have shown the qualitative results to be robust.

2.6 Large Scale Condensation Scheme

While we have constructed a version of this model with a convection scheme (presented in Chapter 7), the model can also be run with large-scale condensation (LSC) only. This version of the model is used in Chapters 3-4. Results from other simulations run with no convection scheme include Donner et al. (1982) and Donner (1986). Humidity and temperature are only adjusted when there is large-scale saturation of a gridbox, i.e., when the specific humidity exceeds its saturation value, $q > q_s$. As is standard, the adjustment is performed implicitly using the derivative $\frac{dq_s}{dT}$, so that condensation does not cause the gridbox to become undersaturated:

$$\delta q = \frac{q_s - q}{1 + \frac{L_v}{c_p}\frac{dq}{dT}} \tag{2.34}$$

where δq is the adjustment to the specific humidity q, q_s is the saturation specific humidity, and L_v is the latent heat of vaporization.

The large scale condensation is accomplished by adjusting the humidity in supersaturated regions to the saturated values immediately, with temperatures adjusted to reflect this condensation. The precipitation falls out immediately, but is re-evaporated below. We use the rather extreme assumption that each layer below the level of condensation must be saturated by re-evaporation for the rain to fall below this level, so the column must be saturated all the way down for precipitation to reach the ground. By maximizing re-evaporation is this way, we are likely compensating for excessive dryness due to the absence of a source of water/condensate from a convection scheme.

We use an expression for the saturation vapor pressure e_s that follows from the Clausius-Clapeyron equation assuming fixed latent heat of vaporization L_v:

$$e_s(T) = e_{s0} exp(\frac{-L_V}{R_V T}) \tag{2.35}$$

with the constant e_{s0} left as a model parameter that we vary in order to change the humidity content of the atmosphere. The saturation specific humidity is calculated from

$$q_s = \frac{\epsilon e_s}{p} \tag{2.36}$$

where $\epsilon = \frac{R_v}{R_d}$ and $p =$ pressure. No freezing is considered in the model. An alternative method to changing the importance of moisture is by varying the latent heat of vaporization L_V in all equations except the Clausius-Clapeyron relation. This is equivalent to varying the e_{s0} parameter except for the virtual temperature effect, as the atmospheric moisture content is different with these two methods.

The resulting model is sensitive to horizontal resolution in the tropics, but midlatitudes are quite insensitive to resolution. Since we focus on midlatitudes in Chapters 3-4, we have chosen to utilize this simplest of models to avoid the additional complexity introduced by the convective parameterization. The simplified Betts-Miller convection scheme we have developed is presented in Chapter 7. We examine the dependence of the tropical circulation on convection scheme in detail in Chapter 7, comparing with LSC only and moist convective adjustment, and among various parameter regimes of the simplified Betts-Miller scheme.

2.7 Dynamical Core

We use the primitive equations for the dynamical core:

$$\begin{aligned}
\frac{\partial u}{\partial t} + \mathbf{v}\cdot\nabla u + \omega\frac{\partial u}{\partial p} &= fv + \frac{uvtan(\theta)}{a} - \frac{1}{acos\theta}\frac{\partial\Phi}{\partial\lambda} - S_u && (2.37)\\
\frac{\partial v}{\partial t} + \mathbf{v}\cdot\nabla v + \omega\frac{\partial v}{\partial p} &= -fu - \frac{u^2tan(\theta)}{a} - \frac{1}{a}\frac{\partial\Phi}{\partial\theta} - S_v && (2.38)\\
\frac{\partial T}{\partial t} + \mathbf{v}\cdot\nabla T + \omega\frac{\partial T}{\partial p} &= \frac{\kappa T\omega}{p} + Q_R + Q_C + Q_B && (2.39)\\
\frac{\partial\Phi}{\partial lnp} &= -R_dT_v && (2.40)\\
\nabla\cdot\mathbf{v} + \frac{\partial\omega}{\partial p} &= 0 && (2.41)
\end{aligned}$$

where $\omega = \frac{Dp}{Dt}$ pressure velocity, T = temperature, $T_v = T/(1-(1-R_d/R_v)q)$ = virtual temperature (which takes into account the density difference of water vapor), R_d = ideal gas constant for dry air, R_v = ideal gas constant for water vapor, $\kappa = \frac{R}{c_p}$, and c_p = specific heat of dry air. Additionally there are the source terms which are calculated from the parameterizations described above: S_u, S_v and Q_B are the surface flux and boundary layer tendencies, Q_R is the radiative heating/cooling, and Q_C is the convective heating/cooling. Additionally the moisture equation is

$$\frac{\partial q}{\partial t} + \mathbf{v}\cdot\nabla q + \omega\frac{\partial q}{\partial p} = g\frac{\partial E}{\partial p} - \frac{1}{L}Q_C \qquad (2.42)$$

where E is the boundary layer flux of humidity.

To integrate these equations numerically, we run with a standard Eulerian spectral dynamical core with triangular truncation, using leapfrog time integration with Robert filter, and 4th order hyperdiffusion. We run with resolutions varying up to T170 (corresponding to 0.7 degree horizontal resolution).

We use sigma coordinates, with 25 unequally spaced levels, with additional resolution in the stratosphere and the boundary layer. The standard spacing of sigma

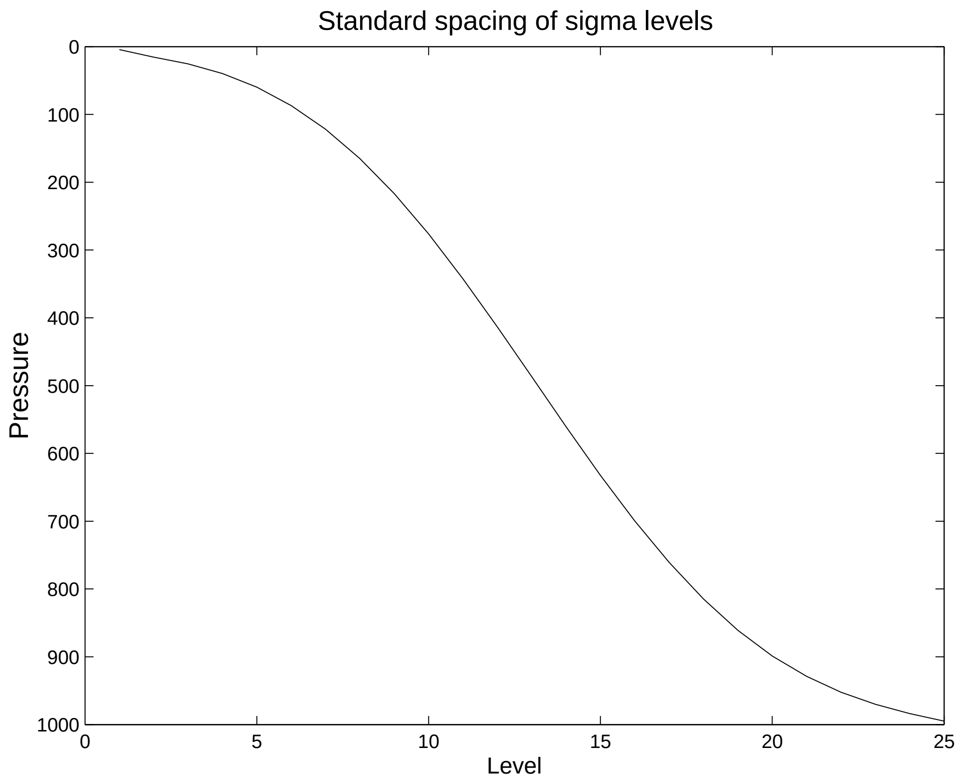

Figure 2.4: Standard spacing of sigma levels.

levels we utilize is given in Figure 2.4. We use the piecewise parabolic method (Collela and Woodward, 1984) for vertical advection of water vapor. The virtual temperature effect is used when calculating the geopotential. We ignore the fact that the mass of the atmosphere should be changed by precipitation.

Energy and moisture are both corrected by a multiplicative factor to ensure exact conservation by dynamics. Due to the nature of the numerical method and typical profiles of velocity and humidity, the moisture correction produces a systematic sink of water vapor, the strength of which is a strong function of resolution (with less correction necessary at higher resolution). At low resolutions, this causes the stratospheric water vapor to be constrained very close to zero. Since water vapor does not feed back into our radiation calculation, this has little effect on the troposphere of our model, with the exception of small relative humidity differences in the upper troposphere.

2.8 Complete Parameter List and Nondimensionalization

We now give a complete list of all parameters used in our control simulation. The parameters for the radiation scheme are in Table 2.1; the remaining parameters are presented in Tables 2.2 and 2.3.

Parameter	Explanation	Control Value
	Numerics and Dynamics parameters	
ν	Hyperdiffusion coefficient	$10^{16}\ m^4\ s^{-1}$
r	Robert coefficient	.03
Ω	Earth rotation rate	$7.292 \times 10^{-5}\ s^{-1}$
g	Gravitational acceleration	$9.8\ m\ s^{-2}$
a	Earth radius	$6.376 \times 10^{6}\ m$
c_p	Specific heat of dry air	$1004.64\ J\ kg^{-1}\ K^{-1}$
R_d	Gas constant for dry air	$287.04\ J\ kg^{-1}\ K^{-1}$
p_{s0}	Mean atmospheric surface pressure	$10^5\ Pa$
	Boundary condition parameters	
d_{ML}	Oceanic mixed layer heat capacity	$10^7\ J\ K^{-1}\ m^{-2}$

Table 2.2: Complete parameter list (part 1)

However, not all the parameters given in Tables 2.1-2.3 are independent. It is therefore interesting to consider the nondimensional parameters of our model, to get an idea of the full range of parameter variations we can obtain. Unfortunately this

Parameter	Explanation	Control Value
	MOS parameters	
κ_{VK}	Von Karman constant	.4
z_0	Roughness length	$3.21 \times 10^{-5}\ m$
Ri_{stabl}	Critical Richardson number for	
	stable mixing cutoff	1
	Boundary layer parameters	
f	Surface layer fraction	.1
	Moisture parameters	
L	Latent heat of vaporization of water	$2.5 \times 10^{6}\ J\ kg^{-1}$
R_v	Gas constant for water vapor	$461.5\ J\ kg^{-1}\ K^{-1}$
e_{s0}	Saturation vapor pressure at 273.16 K	$610.78\ Pa$

Table 2.3: Complete parameter list (part 2)

is a difficult task due to the complexity of the PDE's and physical parameterizations of the model. We therefore begin by nondimensionalizing the dry dynamical core model of Held and Suarez (1994), and continue by adding physical parameterizations sequentially.

2.8.1 Nondimensionalization of Dry Benchmark-Type Models

The dry benchmark model (Held and Suarez 1994) is the primitive equations on the sphere forced by Newtonian cooling and Rayleigh friction, with specified equilibrium temperatures and relaxation times. The equations are the same as we integrate, equations (2.38)-(2.41), with the following physical parameterizations:

$$\begin{aligned} S_{\mathbf{v}} &= \frac{-\mathbf{v}}{\tau_D} && (2.43) \\ Q_R + Q_C + Q_B &= -\frac{T - T_{eq}}{\tau_H} && (2.44) \end{aligned}$$

The parameters in this set of equations are the following: $a, p_s, \Omega, R, \kappa, \tau_H, \tau_D$, and T_{eq}. We point out here that the parameters g and c_p (except in κ) do not appear when the equations are written in this way; therefore these parameters cannot possibly influence the dynamics. Varying g changes the implied vertical coordinates, in a manner that the geopotential remains the same. The model evolution is identical if either the model is run in pressure coordinates, or the vertical levels are changed appropriately if in z-coordinates.

The units in the model are the following: m, s, kg, K. The Buckingham Pi Theorem therefore tells us that there will be $8 - 4 = 4$ independent nondimensional parameters. Since surface pressure p_s is the only parameter with kg in its units, this clearly will not be in any of these. One spanning set of these nondimensional parameters is

$$\left(\frac{\sqrt{RT_{eq}}}{\Omega a}, \frac{1}{\Omega \tau_D}, \frac{1}{\Omega \tau_H}, \kappa \right) \tag{2.45}$$

The first is the ratio of Rossby radius to the Earth radius. The second two are nondimensional timescales. The last is the parameter $\kappa = \frac{R}{c_p}$, which gives the importance of adiabatic cooling to the circulation. We point out again the constants which do not appear in any nondimensional parameters, and therefore do not affect the dynamics: the surface pressure p_s, gravity g, and the specific heat of dry air, c_p (although this appears in κ).

Interestingly, if the equations are made nonhydrostatic, g is no longer unimportant for the dynamics. This can be seen from the nonhydrostatic vertical momentum equation in pressure coordinates,

$$\frac{1}{g^2}\frac{\partial\Phi}{\partial lnp}\frac{D^2\Phi}{Dt^2} = RT + \frac{\partial\Phi}{\partial lnp} \tag{2.46}$$

The equations can no longer be written without referencing g; therefore an additional nondimensional parameter is necessary, for instance, $\frac{\Omega^2 RT_{eq}}{g^2}$. In Garner et al. (2005), we describe a method of increasing the nonhydrostaticity of a model by changing this nondimensional parameter, creating a "hypohydrostatic" model. By varying g and making other changes (discussed below) we can make the nonhydrostatic term more important without altering the hydrostatic model at all. This acts to increase the timescale of convective events. We use this to investigate the feasibility of performing climate sensitivity tests with global cloud resolving models with current computing power.

2.8.2 Adding Moisture

We now add surface fluxes of moisture, a humidity equation, and large scale condensation (i.e., a Clausius-Clapeyron equation). Then the precipitation is considered to be an additional heat source. The equations are the primitive equations above, plus the water vapor equation

$$\frac{\partial q}{\partial t} + \mathbf{u}\cdot\nabla q + \omega\frac{\partial q}{\partial p} = g\frac{\partial E}{\partial p} - P \tag{2.47}$$

where the evaporative flux is parameterized as

$$E = \rho C_D|\mathbf{v}|(q_s - q) \tag{2.48}$$

within the surface layer. We will begin by considering a fixed drag coefficient C_D, and we will look in the surface layer only to isolate the effect of the moisture equation and its surface flux, and remove all boundary layer scheme parameters. We derive with the full surface flux and boundary layer scheme in the next section.

The additional equations are the following: first, for saturation specific humidity

$$q_s = \frac{\epsilon e_s}{p} \tag{2.49}$$

The Clausius-Clapeyron equation is

$$e_s = e_{s0} exp(-\frac{L}{R_v T}) \tag{2.50}$$

Precipitation occurs when there is large-scale saturation, i.e.,

$$P = \lim_{\tau \to 0} \frac{(q - q_s)^+}{\tau} \tag{2.51}$$

The additional term on the right hand side of the temperature equation is:

$$+\frac{LP}{c_p} \tag{2.52}$$

There are several new parameters that have been introduced, with all the same units. From the Pi Theorem, one would think that there will be a new nondimensional parameter for each of these new parameters. However some of the parameters only appear in tandem so this gives an overestimate. The new parameters introduced are $g, C_D, \epsilon, e_{s0}, L, R_V$, and c_p. However, g and C_D appear only as a product and ϵ, e_{s0}, and c_p appear only as a product as well. Therefore we require three new independent nondimensional parameters; these can be written as

$$\left(\frac{gC_D a}{RT_{eq}}, \frac{L\epsilon e_{s0}}{p_s c_p T_{eq}}, \frac{L}{R_v T_{eq}} \right) \tag{2.53}$$

The first is a drag coefficient parameter. The drag coefficient itself is nondimensional, and this parameter is the drag coefficient times an aspect ratio (radius of the earth divided by a typical geopotential height scale from the hydrostatic equation). The second is the typical moist energy variation divided by the dry energy variation. The last is the Clausius-Clapeyron variation parameter.

It is interesting to note that now all of the physical constants which did not appear in the dry benchmark nondimensional parameters appear here. Gravity appears along with the surface drag, and the surface pressure and c_p appear in the energy ratio parameter.

2.8.3 Adding Variable Drag, and Boundary Layer Scheme

First of all, adding sensible heat fluxes and momentum drag within the surface layer give exactly the same nondimensional parameters as the evaporative flux, if the drag coefficients are taken to be the same. We can generalize to a variable drag coefficient by considering the expression for the drag coefficient, equation (2.31). Here it is clear that two additional parameters are used, and new nondimensional parameters are necessary for each. These are

$$\left(\kappa_{VK}^2, \frac{RT_{eq}}{gz_0}\right) \tag{2.54}$$

The former then replaces C_D within the first expression in the set (2.53).

When boundary layer diffusive fluxes are considered as well (see equation (2.33)), we add only the nondimensional namelist parameters f (the fraction of the boundary layer depth that is considered to be the surface layer) and Ri_{stabl}, which is used to calculate the boundary layer depth.

2.8.4 Adding Radiation

We now add the full gray radiation scheme. The optical depths are an additional nondimensional parameter. The divergence of the radiative flux term adds another parameter; this term is the following (written as it appears as a source term in the temperature equation):

$$Q_R = \frac{g}{c_p}\frac{\partial F}{\partial p} \tag{2.55}$$

where F is the radiative flux, proportional to σT^4. The new nondimensional parameter is therefore

$$\frac{g\sigma T_{eq}^4}{c_p p_s} \tag{2.56}$$

2.8.5 Nondimensional Parameter Summary

We summarize the nondimensional parameters of our model.

Dynamics parameters:

$$\left(\frac{\sqrt{RT_{eq}}}{\Omega a}, \kappa\right) \tag{2.57}$$

Moisture parameters:

$$\left(\frac{g\kappa_{VK}^2 a}{RT_{eq}}, \frac{L\epsilon e_{s0}}{p_s c_p T_{eq}}, \frac{L}{R_v T_{eq}}\right) \tag{2.58}$$

Surface flux parameters:

$$\left(\frac{RT_{eq}}{g z_0}\right) \tag{2.59}$$

Boundary layer parameters:

$$(f, Ri_{stabl}) \tag{2.60}$$

Radiation parameters:

$$\left(\tau, \frac{g\sigma T_{eq}^4}{c_p p_s}\right) \tag{2.61}$$

Additionally all parameters that describe the structure in space of a quantity (e.g., the latitudinal structure of the radiative heating or the optical depths) are nondimensional parameters of the model.

“Deep Earth” scaling

The “deep Earth” scaling used in Garner et al. (2005), which reproduces hydrostatic solutions exactly but enhances nonhydrostaticity in a nonhydrostatic model is the following:

$$g \rightarrow \frac{g}{r} \tag{2.62}$$

$$\kappa_{VK} \rightarrow \sqrt{r}\kappa_{VK} \tag{2.63}$$

$$z_0 \rightarrow rz_0 \tag{2.64}$$

$$p_s \rightarrow \frac{p_s}{r} \tag{2.65}$$

$$e_{s0} \rightarrow \frac{e_{s0}}{r} \tag{2.66}$$

With this scaling, all nondimensional parameters in the hydrostatic system remain identical. Therefore the solutions are reproduced exactly. The additional nonhydrostatic nondimensional parameter, however, is increased by a factor of r^2. This term is

$$\frac{\Omega^2 RT_{eq}}{g^2} \tag{2.67}$$

The variables are then scaled by the following:

$$z \rightarrow rz \tag{2.68}$$

$$p \rightarrow \frac{p}{r} \tag{2.69}$$

$$w \rightarrow rw \tag{2.70}$$

$$\omega \rightarrow \frac{\omega}{r} \tag{2.71}$$

with all others (temperature, velocity, humidity, time) remaining the same. The vertical coordinate is stretched, with increases in vertical velocity. Pressure is reduced only to make the radiative fluxes equivalent.

An alternate method of performing the same scaling (a similar method was used by Kuang et al. (2005)) is

$$\Omega \rightarrow r\Omega \tag{2.72}$$

$$a \rightarrow \frac{a}{r} \tag{2.73}$$

$$\kappa_{VK} \rightarrow \sqrt{r}\kappa_{VK} \tag{2.74}$$

$$\nu \rightarrow \frac{\nu}{r^3} \tag{2.75}$$

where ν is the hyperdiffusion coefficient. This results in the following scaling for variables:

$$t \rightarrow \frac{t}{r} \tag{2.76}$$

$$x, y \rightarrow \frac{x, y}{r} \tag{2.77}$$

$$w \rightarrow rw \tag{2.78}$$

In this method the Earth is made smaller, and the timescales sped up. However temperature and velocities all remain the same. Again vertical velocities are increased.

Chapter 3

Static Stability and Eddy Scales in the Moist GCM

3.1 Introduction

The moist GCM we have described in Chapter 2 is an ideal setting for study of the effect of moisture on midlatitude static stability and eddy scales. As mentioned in Chapter 1, most theories for static stability are based on dry dynamics. These have involved parameterizations of vertical baroclinic eddy fluxes (e.g., Green (1970), Stone (1972)), baroclinic adjustment (e.g., Stone (1978a)), depth scales of baroclinic eddies (e.g., Held (1982)), or diffusive arguments (Schneider, 2004). These dry theories all give a common result that the normalized isentropic slope of the atmosphere should be near 1, i.e., that the isentrope beginning in the boundary layer in the subtropics should reach the tropopause at the pole, which is observed.

A notable exception to the dry arguments above is the theory of Juckes (2000), which considers moisture and moist convection to play a dominant role in the determination of midlatitude stability. In this theory, the stability above the moist adiabat is determined by the surface variance of moist static energy, as convection occurs within the warm cores of all baroclinic eddies, and roughly determines the tropopause temperature. The static stability within this framework increases both if the atmospheric moisture content is increased (as the moist adiabat would be more stable), or if baroclinic eddies become stronger (as the surface variance would increase).

Tests of the static stability theory of Held (1982) have been performed within a full GCM by Thuburn and Craig (1997); this indicates that the dynamical constraint of Held (1982) was not accurate within their GCM. Recent results of Cabellero and Langen (2005) additionally show that as surface temperatures are increased in their GCM, the atmosphere becomes more stable (which would presumably support Juckes' hypothesis and go against the dry theories).

Our model provides a useful framework to test the importance of moisture in the determination of the static stability. Since our gray radiation scheme does not respond to moisture concentration, we can vary the water vapor content of the atmosphere by orders of magnitude without radiative feedbacks dominating. Such wide variations allow for clear examination of whether moisture affects the static stability.

We can then study the effect of static stability changes on eddy length scale within the model. If the Rossby radius of deformation is important in determining eddy length scales, the length scales would increase in proportion to the buoyancy frequency. Since eddy kinetic energy also changes significantly as we vary moisture, we can evaluate the importance of the Rhines scale in determining the length scale.

In this chapter, we present simulations in which we vary the water vapor content of the atmosphere from dry to ten times a control value. Since we focus on midlatitude dynamics, we run without a convective parameterization, i.e., with large scale condensation only. Since many aspects of the climatology change significantly as the water vapor content is changed, we first present the basic climatology of these cases in Section 3.2. We examine the sensitivity to horizontal resolution in this section as well.

We then study the static stability in Section 3.3. Since it is more easily examined in the dry limit, this is presented in Section 3.3.1; then the moist cases are considered in Section 3.3.2. We study the eddy length scales in Section 3.4, and conclude in Section 3.5. This chapter is joint work with Isaac Held and Pablo Zurita-Gotor. Parts of this chapter appear in Frierson et al. (2005a).

3.2 Basic Climatology

Integrations have been performed with $e_{s0} = \xi e_{s0}(control)$, with $\xi = 0.0$, 0.5, 1.0, 2.0, 4.0, and 10.0, and with $e_{s0}(control) = 610.78\ Pa$. All experiments have been integrated at T85 resolution, with $\xi = 0$, 1, and 10 also integrated at T170, all with 25 vertical levels. Each of these are run for 1080 days. The simulations start with uniform temperature, and the first 360 days are discarded as spinup. The last 720 days are used for averaging. All time mean quantities are calculated from averages over each time step of the model, whereas spectra are calculated using instantaneous values, sampled once per day. The experiments with $\xi = 10$ are referred to as 10X, etc., and the case with $\xi = 1$ as the control in the following.

Snapshots of the precipitation distribution for the control run at T170 and at T85 resolution are given in Figure 3.1. The primary effect of not having a convection scheme is the presence of small scale storms (often 3-4 gridpoints in size) exploding throughout the tropics. Some of these storms propagate into the subtropics and take on some features expected of tropical storms. In midlatitudes, by contrast, the precipitation is characterized by baroclinic wavelike structures.

To examine convergence with resolution in midlatitudes, we plot the zonal mean surface winds and the vertically averaged spectrum for the meridional velocity (discussed in detail in Section 3.4) for T42, T85, and T170 for the control run in Figure 3.2. In these fields, T42 departs significantly from T85 and T170; the maximum

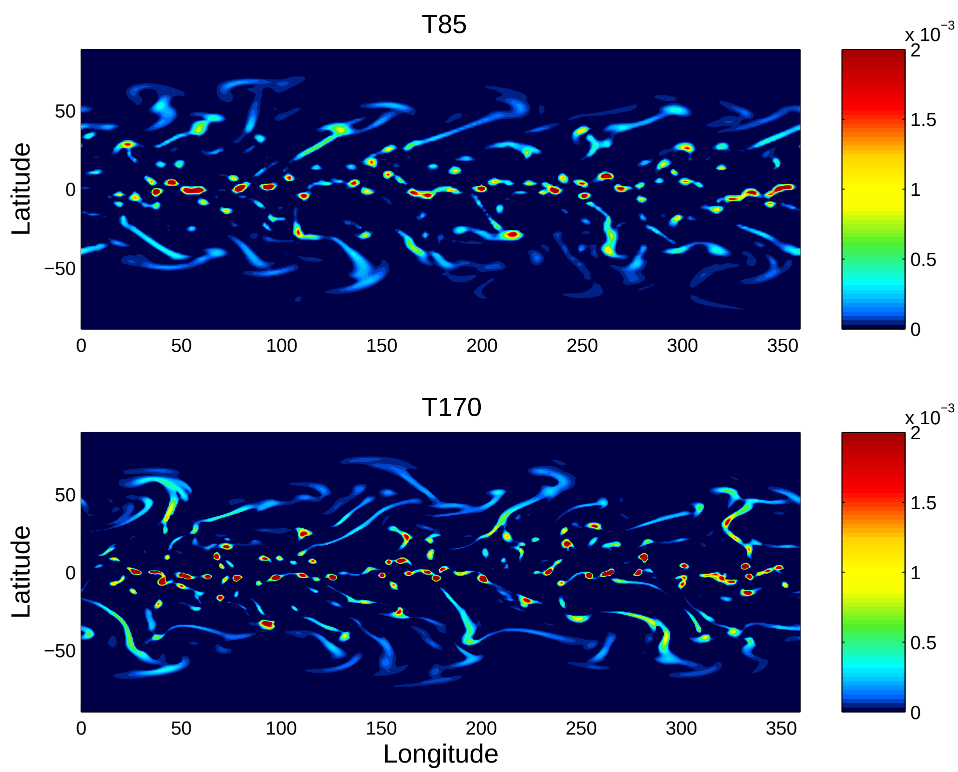

Figure 3.1: Instantaneous precipitation distributions (in $kg\ m^{-2}\ s^{-1}$) for the control case at T85 resolution and at T170 resolution.

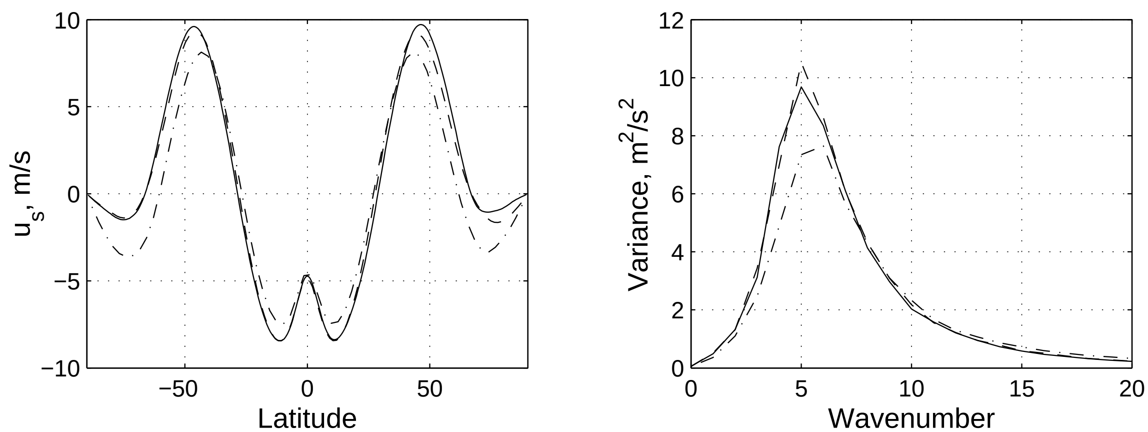

Figure 3.2: Left: Resolution dependence of time mean zonal mean surface zonal winds. Right: Resolution dependence of zonal wavenumber spectra for $< v >$ at 45 degrees latitude. T170 (solid), T85 (dashed), and T42 (dash-dot).

surface winds are weaker and shifted equatorward, and the spectrum displays a less peaked maximum. The T42 case has slightly smaller eddy length scale than the higher resolution cases.

Figure 3.3a shows the zonally averaged zonal winds as a function of pressure in the control case. The maximum zonal wind of 30.0 $m\ s^{-1}$ occurs at $(42.5°, 217hPa)$, the maximum surface winds of 9.7 $m\ s^{-1}$ at 47°, and the strongest easterlies at $(11°, 900hPa)$, with magnitude $-9.8\ m\ s^{-1}$. There is evidence of separation of the Hadley cell, or subtropical, jet with maximum near 25°, and an eddy-driven jet, with maximum near 45° .

Virtual dry static energy (divided by c_p) is shown in Figure 3.4a. There is a $53K$ temperature difference at the lowest model level. Midlatitudes are stable for dry disturbances, with $d\theta/dz = 4.1K/km$ averaged from 30 to 60 degrees between the surface and the tropopause. On the same figure, we plot the tropopause based on the WMO definition: the lowest level where the lapse rate reaches (and stays above) $2K/km$. The tropical and extratropical tropopauses are clearly distinguished. The tropopause height is found to be relatively insensitive to the lapse rate criterion, except in polar regions. The moist stability of the model is described in Section 3.3.

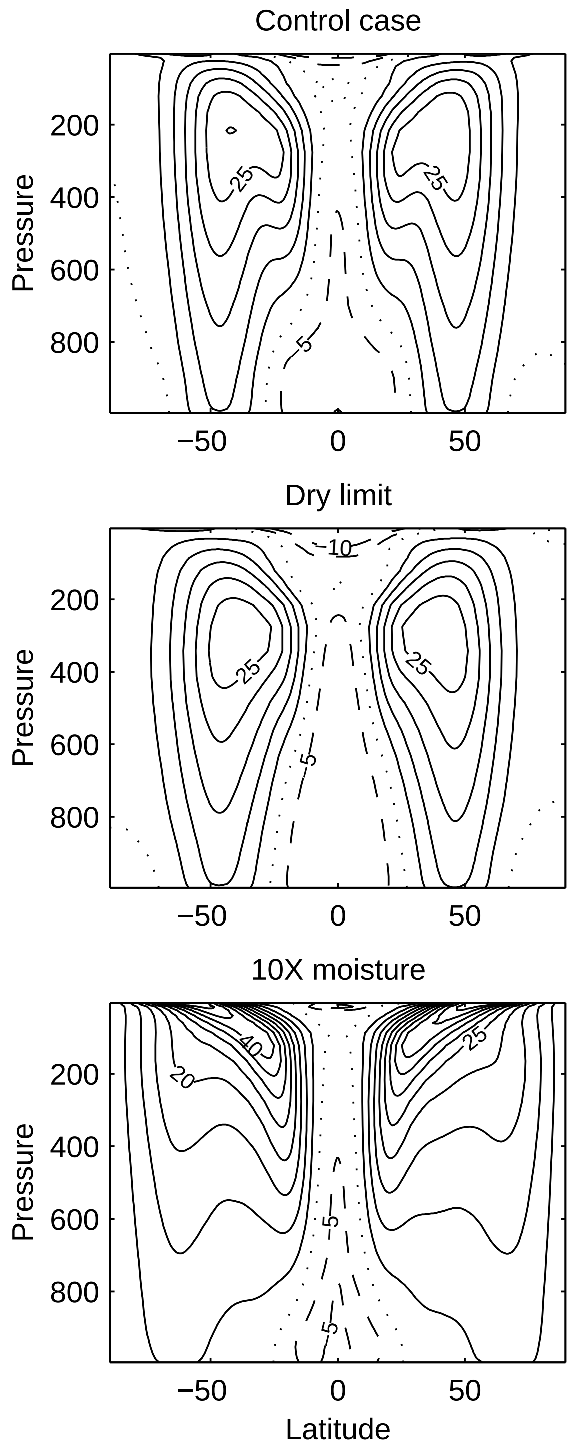

Figure 3.3: Time mean zonal mean zonal winds (m/s) for the control case, the dry limit, and the 10X case. The contour interval is 5 m/s and the zero contour is shown with dotted lines.

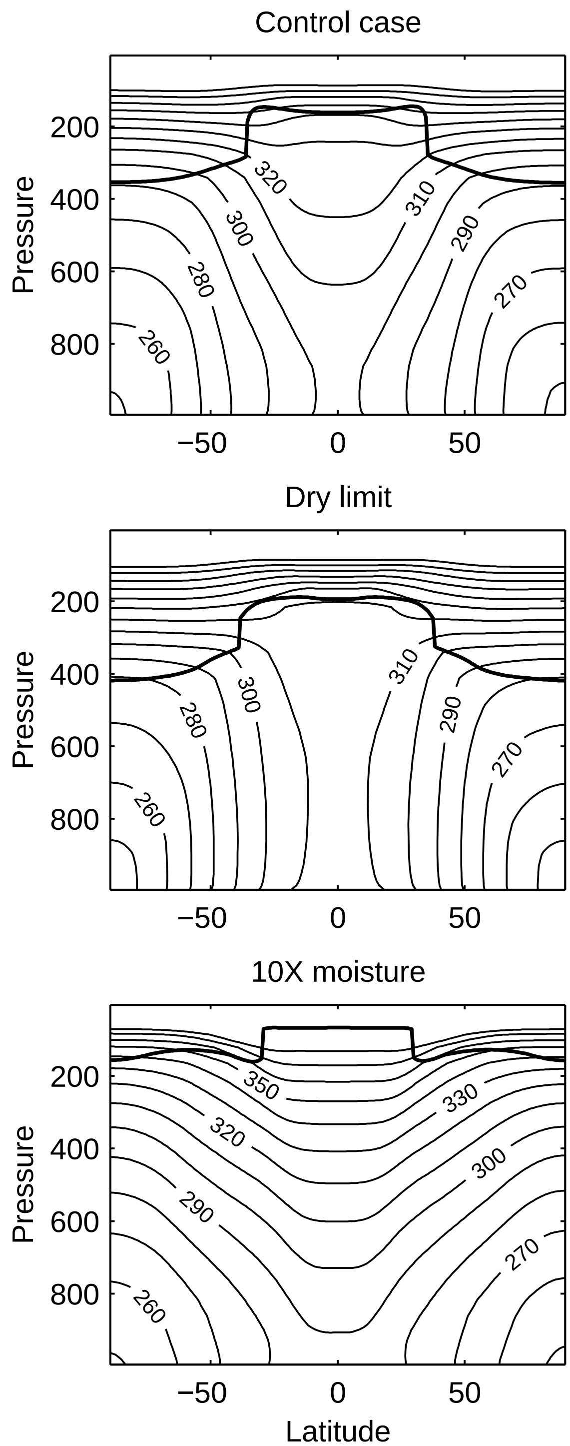

Figure 3.4: Time mean zonal mean virtual dry static energy (K) for the control case, the dry limit, and the 10X case. The contour interval is $10K$. The WMO tropopause is shown with the bold line.

The standard Eulerian meridional overturning streamfunction is plotted in Figure 3.5a (note the different contour intervals for direct and indirect circulations). There is a very strong Hadley cell, with maximum strength of 260 $Sv = 2.6 \times 10^{11} kg\ s^{-1}$. This is more than 3 times the observed annual mean strength. The Ferrel cell, with a maximum strength of 54 Sv at 40 degrees, is comparable to that in annual mean observations. The Hadley cell strength is somewhat sensitive to model resolution (285 Sv at T85, 265 Sv at T42).

There are at least three aspects of our model formulation that conspire to create a very strong Hadley cell: absence of oceanic heat transport, absence of a convective parameterization scheme, and absence of absorption of solar radiation within the atmosphere. In experiments in which we include the latter two effects (Chapter 7), the Hadley cell is reduced to the still large value of 180 Sv; this depends somewhat on the convective parameterization and parameters within this scheme. The sensitivity of the Hadley circulation to convection scheme is discussed in detail in Chapter 7. Over observed sea surface temperatures (which includes an implied ocean heat flux to sustain the SST's) and with a convection scheme, the Hadley cell attains a value similar to observations.

Finally, the relative humidity distribution is plotted in Figure 3.6a. The deep tropics are close to saturation everywhere. The local minimum in the subtropical subsidence regions is 43%, significantly larger than observations, despite the strength of the overturning. In the polar regions, the relative humidity is quite high, above 70% relative humidity for almost the entire troposphere from 55 degrees poleward.

Returning to Figs. 3.3-3.6, we have also plotted the corresponding figures for the dry and 10X simulations. The similarity of the zonal mean winds (Figure 3.3) in the dry and control cases is remarkable. The hint of a two jet structure present in the control is absent in the dry limit, however. In the 10X model in contrast, the circulation has shifted poleward substantially and has weakened. We plot in Figure 3.7

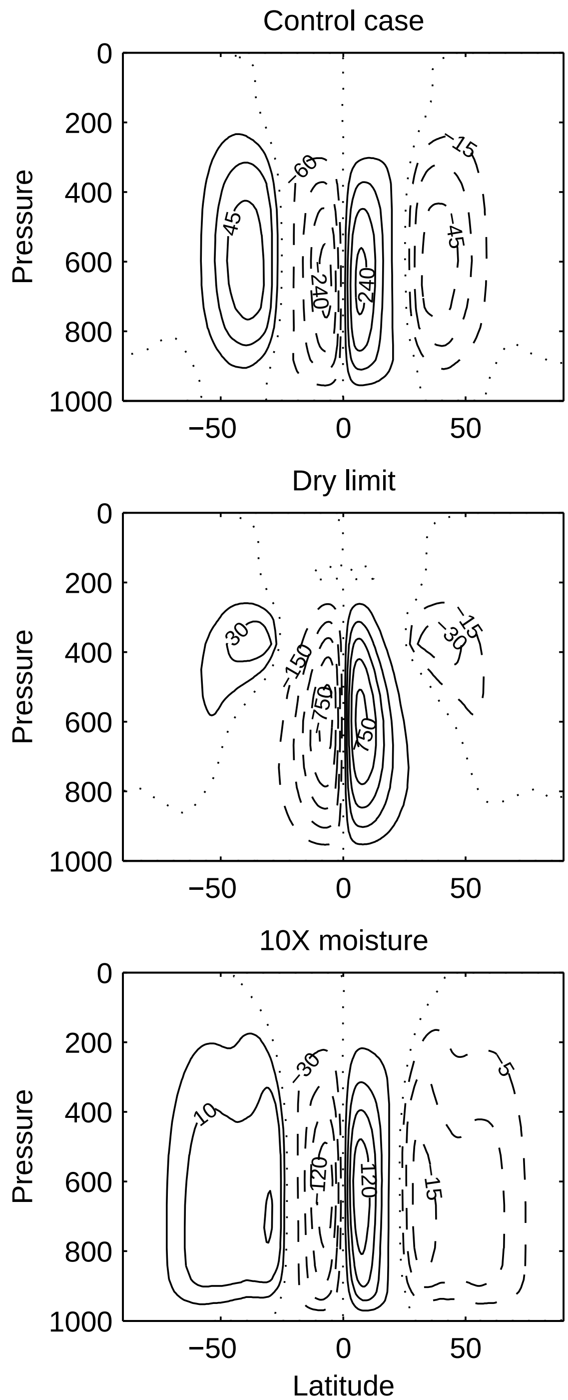

Figure 3.5: Time mean zonal mean streamfunction (in $10^9 kg/s$) for the control case, the dry limit, and the 10X case. Note the different contour intervals for direct and indirect circulations for each plot. The contour intervals for (direct, indirect) circulations are (60, 15) for the control case, (150, 15) for the dry limit, and (30, 5) for the 10X case (all expressed in $10^9 kg/s$).

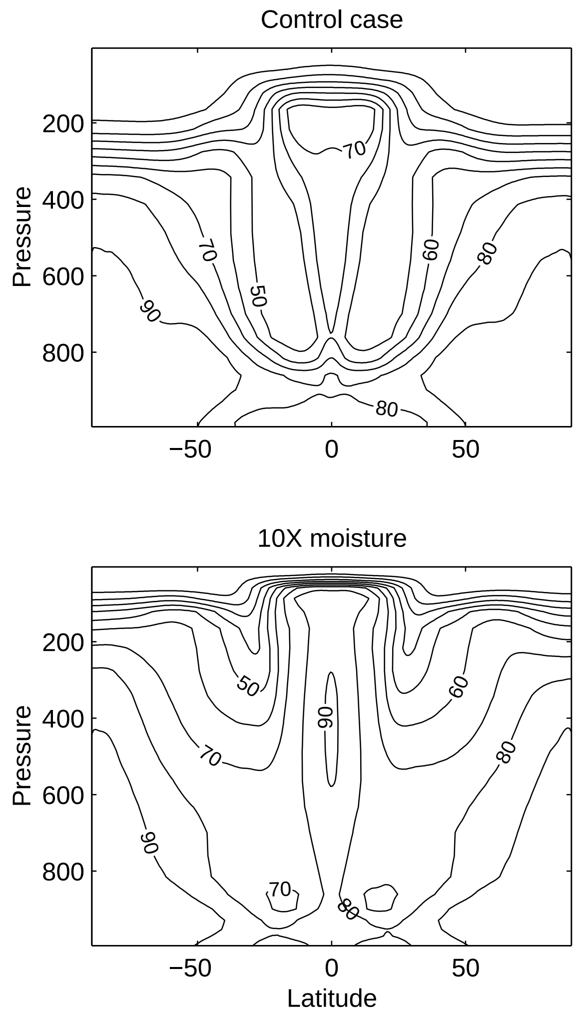

Figure 3.6: Time mean zonal mean relative humidity (%) for the control case, and the 10X case. The contour interval is 10%.

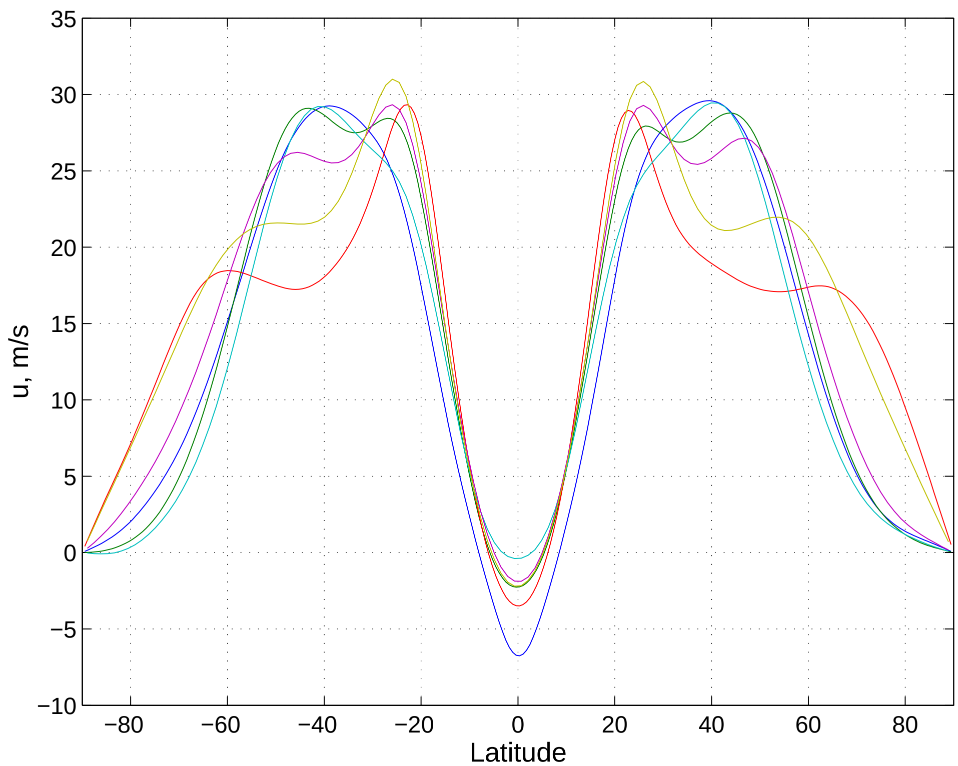

Figure 3.7: Zonal winds at 276 mbar for $\xi = 0$ (blue), $\xi = 0.5$ (cyan), $\xi = 1$ (green), $\xi = 2$ (magenta), $\xi = 4$ (yellow), and $\xi = 10$ (red).

the profiles of upper tropospheric winds for all values of ξ examined. The poleward shift and weakening occur gradually as ξ increases beyond unity. There is only a slight hint of equatorward movement and strengthening when we reduce the moisture content of the atmosphere below that in the control. The upper tropospheric winds in the tropics and subtropics change very little with moisture content, despite, as we will see, a large change in the Hadley circulation.

Upper tropospheric tropical temperatures are significantly colder in the dry limit, because the lapse rate, fixed at dry adiabatic throughout the tropics, is now larger. This can be seen in the plot of dry static energy for the dry limit, Figure 3.4b. The isentropes are nearly vertical for a large part of the troposphere. Again we overlay the tropopause height, calculated from the WMO criterion: the tropopause is slightly lower than in the control case everywhere. In this case the average vertical gradient of potential temperature below the tropopause from 30 to 60 degrees is $\frac{\partial\theta}{\partial z} = 2.2K/km$ with most of this stability contributed by the layer just beneath the tropopause.

The equator-pole temperature difference at the lowest model level is much greater in the dry limit (Figure 3.8): $71K$ compared to $53K$ in the control case. This value is, however, smaller than the lowest level moist static energy contrast of the control ($89K$). The dry-limit equator-pole temperature difference at the surface (as opposed to the lowest atmospheric level) is $85K$, implying an increased temperature jump between the surface and lowest model level in the tropics. This jump provides a much larger sensible heat flux, compensating for the lack of evaporative cooling of the surface. Surface temperatures at the pole are roughly equal in the control and dry models, whereas tropical surface temperatures are much larger in the dry case. In the 10X run, the equator-to-pole temperature contrast at the lowest model level is weakened to 40 K and there is a smaller temperature jump at the surface as well. Figure 3.8 summarizes the pole-to-equator temperature and moist static energy differences at the surface, and in the lowest model level, as a function of ξ for all cases. There is a gradual decrease of the temperature gradient and increase of the moist static energy gradient as ξ is increased. We discuss factors controlling the low level moist static energy gradient in Chapter 4.

Examining the streamfunction (Figure 3.5b-c, note the different contour intervals for direct and indirect circulations, and for each plot), we see the presence of a much stronger Hadley cell in the dry case, extending further poleward as well. The strength of the overturning is 810 Sv, exceeding the value in the control case by a factor of three. This corresponds to meridional winds of nearly 8 $m\ s^{-1}$ in the time mean in both the upper and lower troposphere. In this case, a direct circulation exists for all latitudes within the boundary layer. A small region of indirect circulation remains, but only in the midlatitude upper troposphere. This Ferrel cell, weakened to 40 Sv, cannot penetrate into the area dominated by boundary layer mixing, where

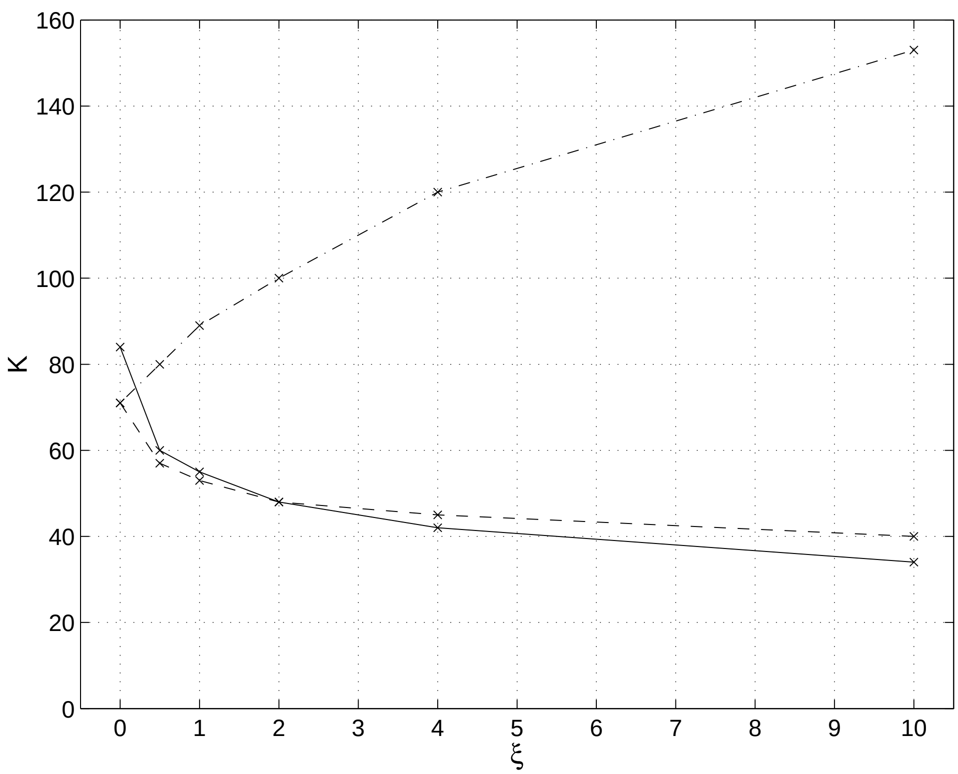

Figure 3.8: Equator-to-pole virtual temperature difference at the surface (solid), at the lowest model level (dashed), and moist static energy difference at the lowest model level (dash-dot) for all cases.

diffusive momentum fluxes dominate over the large-scale eddy fluxes. Poleward energy transport in the tropics is similar in the two models despite the very different Hadley cell strengths (see Chapter 4). The Hadley cell in the 10X case is weakened to 145 Sv, but we caution the reader that this value is sensitive to resolution. Additionally the Ferrel cell is much weaker (12 Sv), is displaced poleward, and shows evidence of splitting into two cells.

The relative humidity for the 10X case is plotted in Figure 3.6b. With the exception of the area just above the boundary layer and part of the midlatitude free troposphere, the 10X case has higher relative humidity than the control case. In particular, the subtropics and tropical regions are both significantly closer to saturation; the 10X case exceeds the control case by 33% RH at the location of minimum relative humidity in the subtropics.

The simulations show increasing separation between the subtropical and eddy-driven jets as the atmosphere is moistened. These two jets are merged in the dry run, show a hint of separation in the control, and separate for larger values of ξ. As moisture is increased the subtropical jet tightens and the eddy-driven jet moves poleward. This is illustrated in Figure 3.9, which shows the location of the maximum surface westerlies as a function of ξ. Figure 3.10 shows the vertically-integrated eddy kinetic energy (EKE) as a function of latitude for different values of ξ. Not surprisingly, the eddies also move poleward with the jet.

The poleward shift in this model can be explained, we believe, in terms of the preferential stabilization of baroclinic eddies at low latitudes. As moisture is added, the meridional temperature gradient decreases and the static stability increases, both effects leading to a flattening of the (dry) isentropic slope and a weakening of the eddies. The reduction in global-mean EKE is apparent in Figure 3.10; however, it is also apparent in that figure that this stabilization occurs primarily at low latitudes. There are at least two reasons for this. First, the meridional temperature gradient

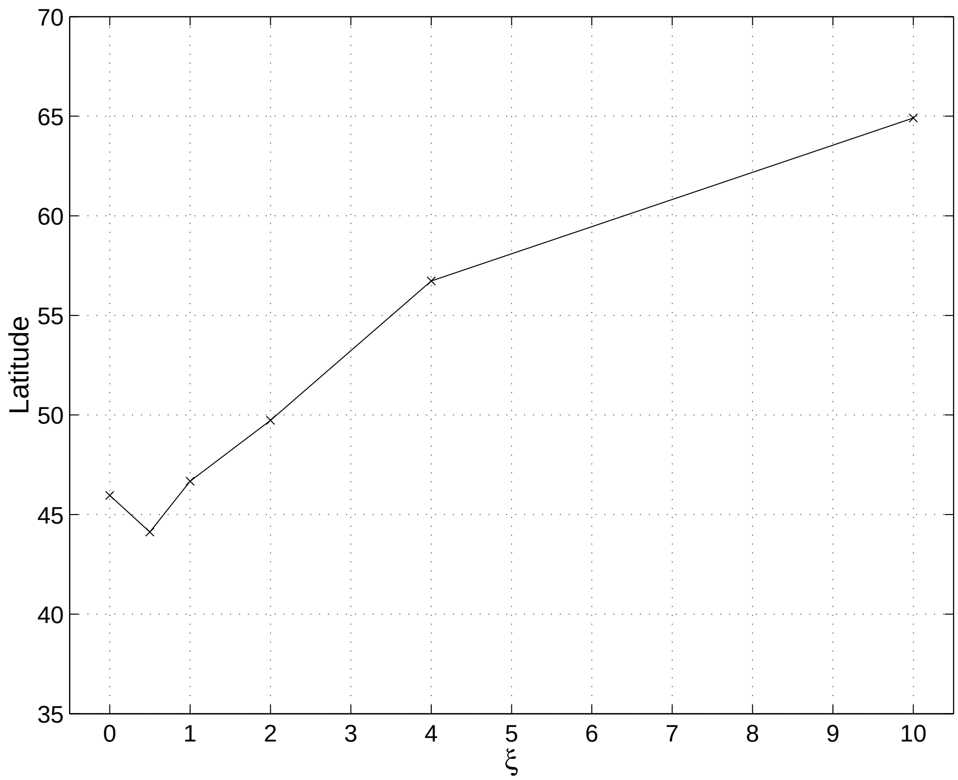

Figure 3.9: Latitudinal position of maximum surface westerlies as a function of moisture content ξ.

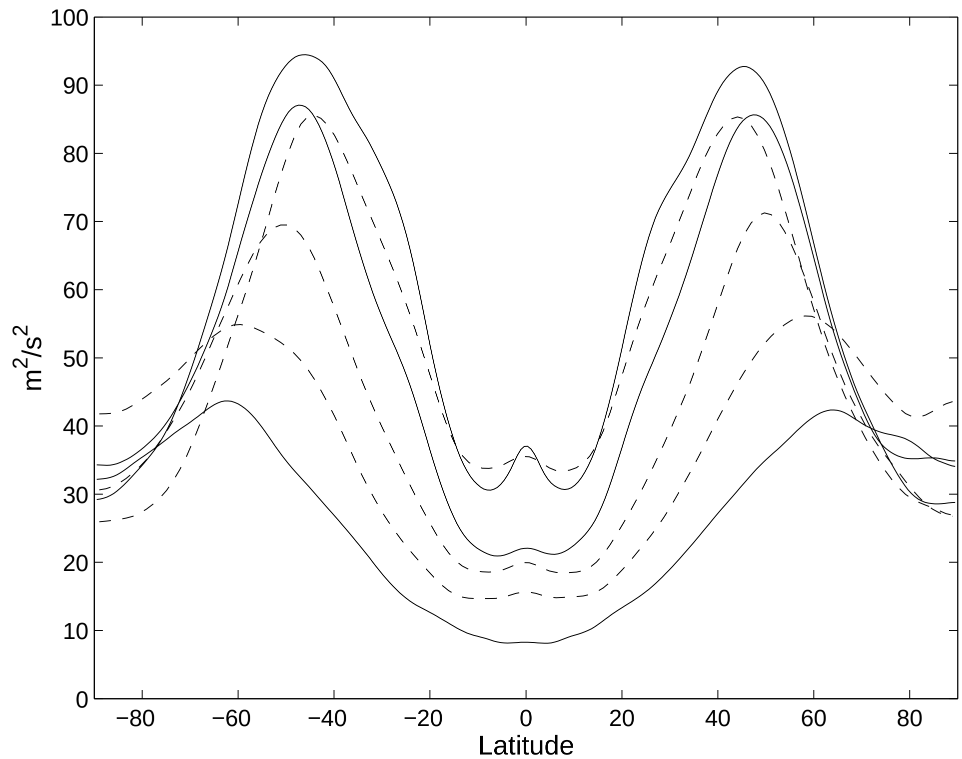

Figure 3.10: Eddy kinetic energy, averaged over pressure, for the control case, the dry limit, and the 10X case at T170 (solid lines, maxima decrease with moisture), and the 0.5X case, 2X case, and 4X case at T85 (dashed lines, maxima decrease with moisture).

is weakened the most at low latitudes (where moisture represents a larger fraction of the moist static energy). Additionally, the stabilizing effect of β is strongest at low latitudes, so these latitudes are stabilized most strongly when the isentropic slope is reduced (for instance, using the two-layer stability criterion, the critical isentropic slope increases equatorward with $\beta H/f_0$). In the experiments with $\xi < 1$, it appears that the the eddy-driven jet cannot move further equatorward, as it encounters the very weak temperature gradients maintained by the Hadley cell.

3.3 Static Stability

3.3.1 Dry Limit

We first examine the static stability in the dry limit. In this case the convection is simply boundary layer diffusion, which has a well-defined top, the boundary layer depth. As seen in an instantaneous plot of boundary layer depth (Figure 3.11a), depths approaching the tropopause height are observed out to midlatitudes. We plot the probability density function of the planetary boundary layer depth on top of the time-mean dry static energy in Figure 3.11b. In the tropics there is almost always dry convection to the tropopause. In midlatitudes, there is naturally little mean stratification in the lower troposphere, in regions where the boundary layer is almost always present, but there is some mean stratification in the upper troposphere, where the convective mixing penetrates more sporadically. The boundary layer extends to the tropopause on occasion. This is true for all latitudes equatorward of 60°. In high latitudes, the radiative equilibrium is more stable, and the static stability is determined by a balance between radiation and the large-scale eddy fluxes. There, as in the control run, the isentropes are quasi-horizontal, and convection does not reach to the tropopause as conventionally defined (but the tropopause is less well-defined at these latitudes).

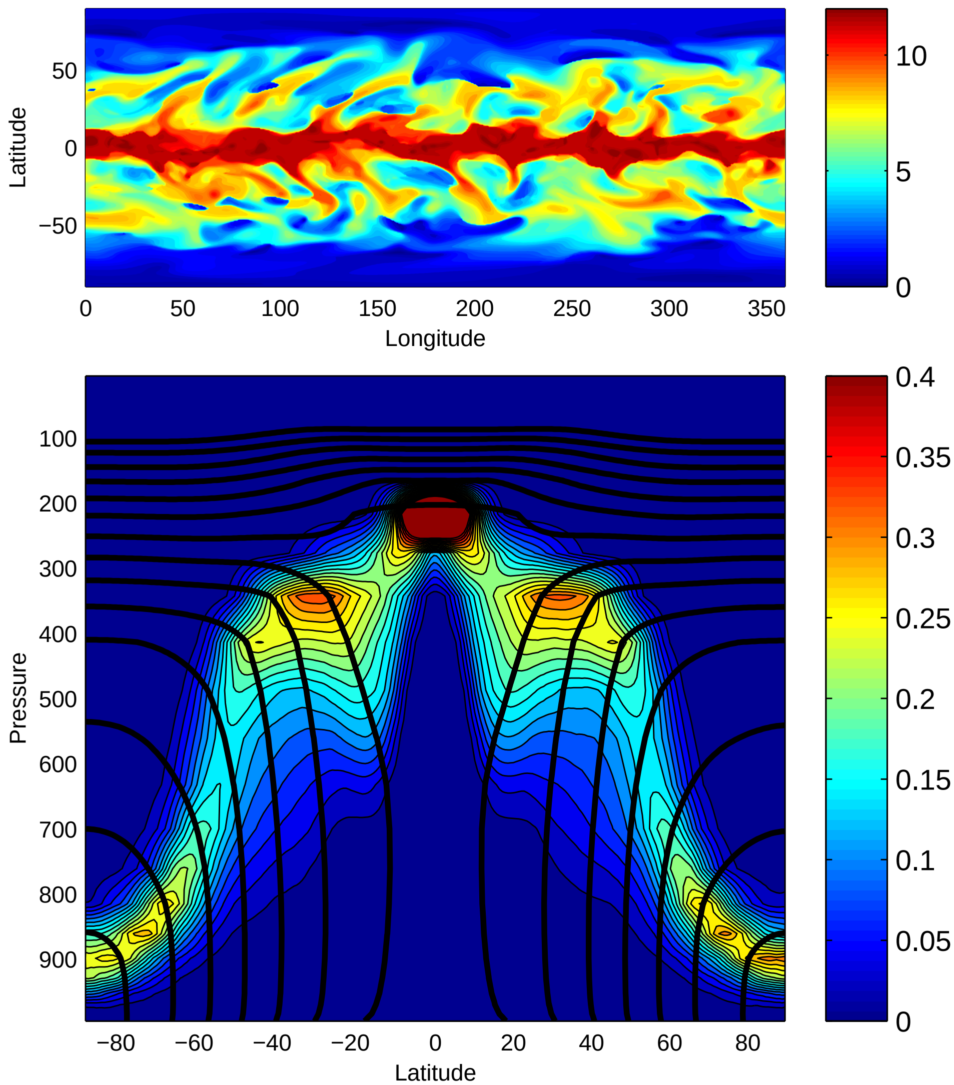

Figure 3.11: Top: Instantaneous planetary boundary layer depth (in km) for the dry limit. Bottom: Probability density function of boundary layer depth at each latitude (shading) and dry static energy (contours) for the dry limit. Contour interval for DSE is $10K$.

The picture that emerges seems consistent with the argument of Juckes (2000), with the tropopause supported by the deepest convection in the favorable sectors of extratropical eddies. We have made an initial attempt to vary the importance of the large-scale eddies by varying the parameter Δ_{sol} which controls the meridional variation of the solar heating, thereby modifying baroclinicity and eddy amplitudes. In addition to the control case (1.4), we have analyzed cases with both decreased (1.0) and increased (1.8) insolation gradients, at T85 resolution. (We find that the dry model is very well converged at this resolution). We cannot increase the insolation gradient further, given our functional form, without creating negative solar heating at the poles. Eddy kinetic energy increases by 15% in the increased solar gradient case, and decreases by 16% in the reduced gradient integration. Since these changes are relatively small, we do not expect changes in the dominant balances, but we can check for consistency with expectations based on a picture of convection-dominated static stabilities.

The dry static energy and the pdf of the boundary layer depth remain qualitatively unchanged in these integrations. The case with increased insolation gradient is slightly more stable; however convection still extends to the tropopause equatorward of 60°, even though the temperature contrast has been increased to $88K$ at the lowest model level. We plot the PDF's at 45° for the standard dry limit, and for $\Delta_{sol} = 1.8$ and 1.0 in Figure 3.12a. The variance of the boundary layer depth increases with increased solar gradient. As anticipated from Juckes (2000), increased variance in the depth of convection corresponds to increased stability.

We plot the difference between the dry static energy and the dry static energy at the lowest model level at 45° for these three dry cases in Figure 3.12b. Increasing the solar gradient increases the bulk stability (tropopause minus surface dry stability) at this latitude from $1.4K/km$ to $1.7K/km$ to $2.1K/km$ in the three cases. This bulk stability increases at all latitudes.

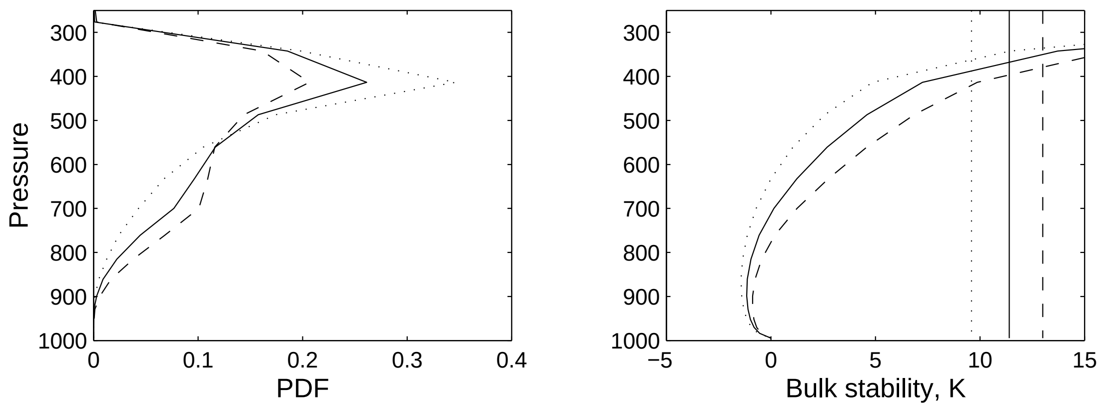

Figure 3.12: Left: Probability density function of boundary layer depth at 45 degrees latitude. Right: Dry static energy minus its surface value at 45 degrees latitude. The vertical lines indicate twice the standard deviation of surface moist static energy. $\Delta_{sol} = 1.4$ (solid), 1.8 (dashed), and 1.0 (dotted), all dry simulations.

Juckes relates the stability to the standard deviation of the surface static energy. The values of this quantity at 45° are 4.8 K, 5.7 K, and 6.5 K for $\Delta_{sol} = 1.0$, 1.4, 1.8. We indicate two times this standard deviation by vertical lines in Fig 3.12b. Although it is difficult to make a precise comparison due to the arbitrariness of the determination of the tropopause, we note that these values are similar in both magnitude and relative changes to the upper tropospheric bulk stabilities.

In order to create a transition to a large-eddy dominated midlatitude thermal structure, in which it is clear that no convection reaches the tropopause, it appears that we would need to increase the strength of the eddies, or decrease the intensity of convection by dramatically reducing the radiative destabilization of the atmosphere. We have not obtained a clear transition of this sort to date. It is important to do so to make contact with dry simulations such as that of Schneider (2004). We also note that this qualitative behavior, in which stability increases as the horizontal temperature gradients increase, is also predicted by baroclinic adjustment theories (Held (1982) and Schneider (2004), in which the isentropic slope is constrained to remain approximately unchanged.

3.3.2 Moist Cases

There is no simple diagnostic similar to the boundary layer depth for the moist cases. We examine a bulk moist stability similar to the bulk dry stability presented in the previous section, using the difference between the saturated moist static energy and the moist static energy at the surface, again all accounting for the virtual temperature effect. These are plotted for the control case, 10X case, and dry limit in Figure 3.13a-c. All three simulations are seen to be rather similar in bulk moist stability, and the level of zero buoyancy is very similar for the three cases. The large amount of conditional instability in the deep tropics is decreased greatly when we utilize a convection scheme; poleward of this the stabilities remain similar. Above the unstable region, the 10X case is the most stable, while the dry limit is the least stable. This increased moist stability with increasing moisture can be seen in Figure 3.14), where we can see that the bulk stability at the tropopause, the midtropospheric moist lapse rates, and the amount of CAPE all increase as moisture is added.

To explain this increased moist stability, we examine the surface standard deviation of the moist static energy. At 45°, these are 5.8 K, 7.4 K, and 12.8 K, for the dry limit, control case, and 10X case, respectively. Again we plot twice these standard deviations as vertical lines in Figure 3.14. The precise comparison depends on the definition of the tropopause once again. Using the WMO tropopause, the bulk moist stability at the tropopause is approximately 2-2.25 times the surface MSE standard deviation for each case. We can relate the standard deviation of surface moist static energy to the gradient of this quantity at the surface, setting

$$|m'| \sim L\frac{\partial m}{\partial y} \tag{3.1}$$

where L is a mixing length. The equator-to-pole moist static energy gradient increases by 25% from the dry limit to the control case, and 72% from the control case

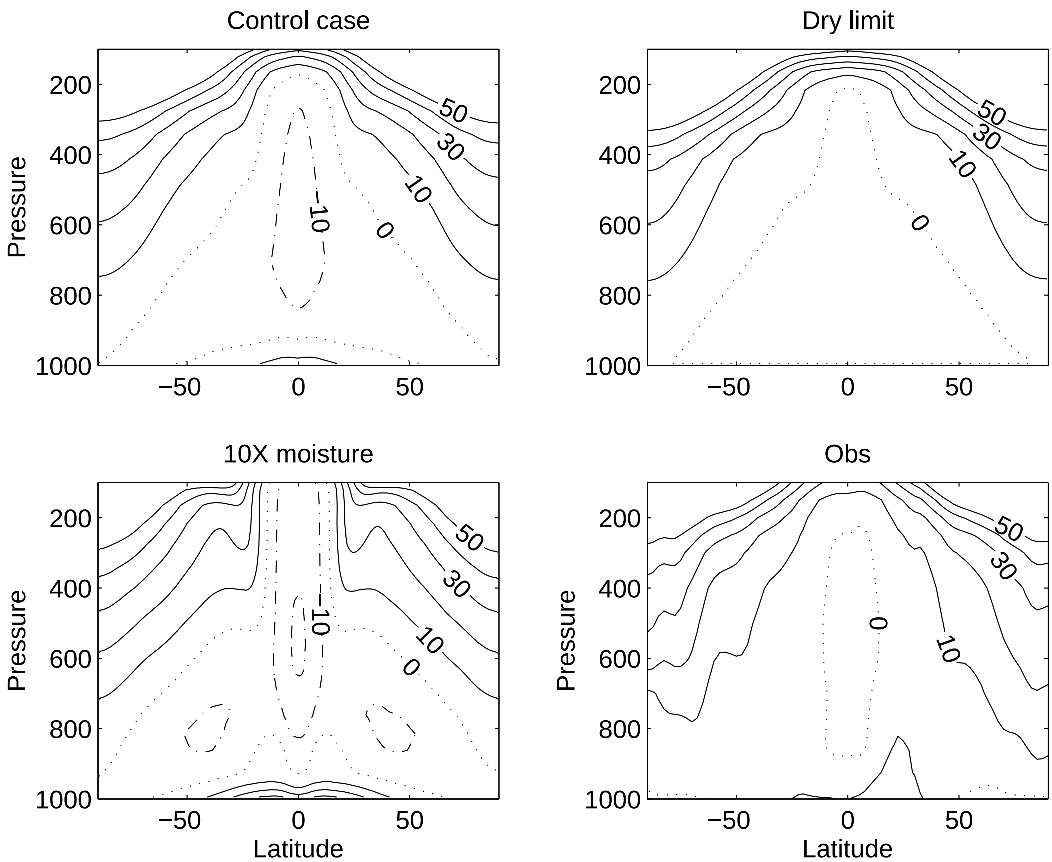

Figure 3.13: Bulk moist stabilities, defined as saturated MSE minus MSE at the surface for the control case, the dry limit, the 10X case, and the NCAR/NCEP reanalysis data, 2000-2004. Contour interval is 10 K.

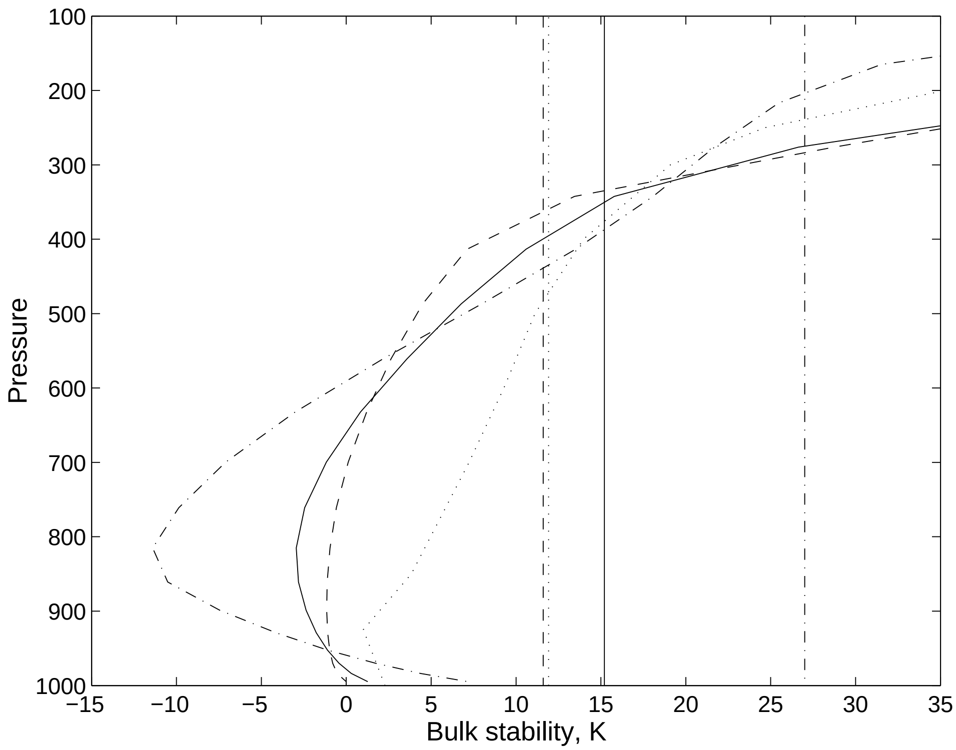

Figure 3.14: Bulk moist stability at 45°, with twice the surface moist static energy standard deviation indicated by the dotted lines for the control case (solid), the dry limit (dashed), the 10X case (dash-dot), and the NCAR/NCEP reanalysis data at 45° S, 2000-2004 (dotted).

to 10X case, suggesting that to first order, the increase in the moist static energy standard deviation (by 28% and 73%) can be understood as due to the increased surface gradient with fixed mixing length. We further discuss length scales in Section 3.4, and low level moist static energy gradients in Chapter 4.

Stability quantities for the NCAR/NCEP reanalysis data averaged zonally and between 2000 and 2004 are presented in Figures 3.13d and 3.14. Especially in the Southern Hemisphere, the atmosphere has a neutrality to moist convection similar to the control case. The Southern Hemisphere, being more ocean-covered, provides a somewhat closer analog to the aquaplanet model than does the Northern. A notable difference is the lack of CAPE away from the deep tropics in observations. The surface standard deviation of moist static energy at 45 degrees is 6.0 K, and multiplying by two again gives a relatively good approximation for the tropopause minus surface difference in m at this latitude.

The tropopause height increases with increasing water vapor in these simulations; it is twice as high in the 10X case as in the control, in particular. These variations can be explained in terms of the radiative constraint between tropopause height and lapse rate, or equivalently a radiative-convective equilibrium model with a moist convective adjustment (as in Thuburn and Craig (1997)). The decreased lapse rates in the cases with more moisture require convection to penetrate more deeply before matching smoothly onto the radiative equilibrium temperatures in the stratosphere.

3.4 Eddy Length Scales

We estimate characteristic eddy length scales using the pressure averaged wavenumber spectrum of the meridional velocity. In Figure 3.15a, we plot the spectrum of this quantity at 45 degrees as the moisture content of the model is varied. Figure 3.2b gives an idea of the typical change in this quantity with resolution; with the primary differences seen in the 10X case, where scales become larger with increased resolution. It is clear from this figure that the typical scales of eddies change remarkably little as we vary the moisture content. The wavenumber of maximum variance is at wavenumber 5 for all cases but the 0.5X case, which has a maximum at wavenumber 6. Further, the spectral shape is nearly unchanged. A closer look shows that the 10X has a slightly flatter spectrum, with more fractional variance at lower wavenumbers and at higher wavenumbers than the other cases, but we do not see this clearly in the intermediate moisture cases. There is little support here for the idea that increased moisture preferentially strengthens smaller scale storms.

For better comparison with various theories for the eddy scale, we define the average wavenumber of the disturbances as

$$\bar{k} = \frac{\int kE(k)dk}{\int E(k)dk} \tag{3.2}$$

where $E(k)$ is the spectrum shown in Figure 3.15a. We plot the average length scale for this wavenumber,

$$\bar{L} = \frac{2\pi a cos(\theta)}{\bar{k}} \tag{3.3}$$

in Figure 3.15b. In the tropics the moister cases have smaller scales. However, from the subtropics to the polar regions, the average length scales are very similar. The mean length scale is remarkably constant at around 4000 km over the entire midlatitude and subtropical region for all cases. As the moisture content is increased, the mean length scale is decreased slightly. In polar regions several of the simulations have larger length scales, but there is sampling error at these latitudes, as can be seen from the asymmetry between hemispheres.

The maximum separation among the three T170 cases in the extratropics occurs at 33°, where the scales decrease with moisture but are still within 7% of each other. The variations with resolution may be significantly different at the two resolutions,

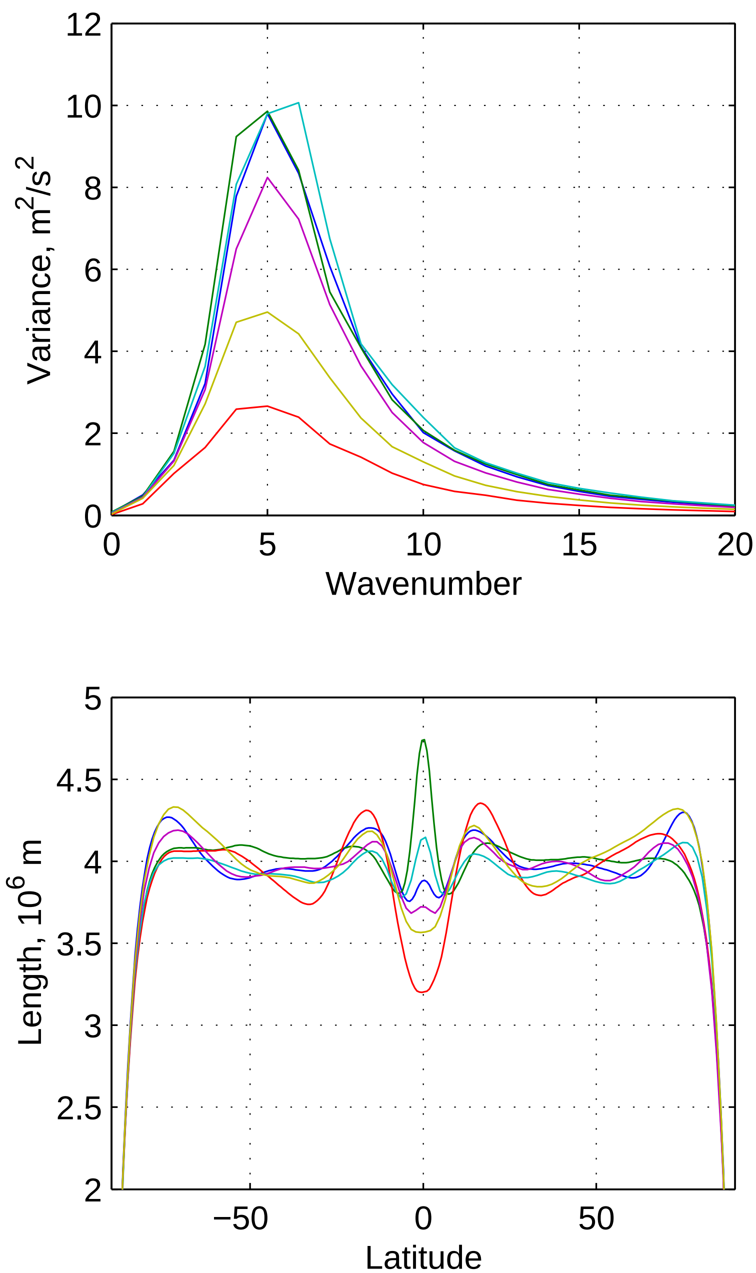

Figure 3.15: Top: Zonal wavenumber spectra for $< v >$ at 45 degrees latitude for the dry limit (blue), control case (green), and 10X case (red), all at T170 resolution; and the 0.5X case (cyan), 2X case (magenta), and 4X case (yellow), all at T85 resolution. Bottom: Mean length scale $\bar{L}$ as a function of latitude (see text for definition), same color scheme.

but they are very small in all cases. The resilience of the length scale to change with moisture is quite remarkable given the large changes in static stability.

We compare these mean length scales with two different Rossby radii and a Rhines scale. We define the Rossby radius of deformation using the tropopause height,

$$L_{DT} = 2\pi \frac{N H_T}{f_0} \tag{3.4}$$

where N is the average buoyancy frequency below the WMO tropopause, H_T is the WMO tropopause height discussed above, and f_0 is the local value of the Coriolis parameter; the Rossby radius using a scale height instead of the tropopause height,

$$L_{DS} = 2\pi \frac{N H_s}{f_0} \tag{3.5}$$

where N is calculated as above, and H_s is taken to be 8 km; and a Rhines scale

$$L_{\beta} = 2\pi \sqrt{\frac{v_{RMS}}{\beta}} \tag{3.6}$$

A comparison of these length scales for the T170 cases is found in Figure 3.16. The theoretical Rossby radii all increase sharply at the subtropical jet, where there is a jump in tropopause height. Here we focus on the latitudes poleward of the subtropical jet. Clearly the Rossby radii vary much more with moisture than $\bar{L}$. If L_{DT} is used, the predicted increase of length scales at 45° from dry limit to 10X case is a factor of 3.5. Using L_{DS} significantly decreases the scales in the 10X case, but still predicts an increase in scale of 75% from the dry limit to 10X. Since eddies reach significantly higher in the atmosphere as the moisture content is increased (up to the tropopause in all cases), it is presumably unjustified to use an even smaller height scale in the cases with more moisture.

We have computed a moist Rossby radius by substituting a bulk moist stability for

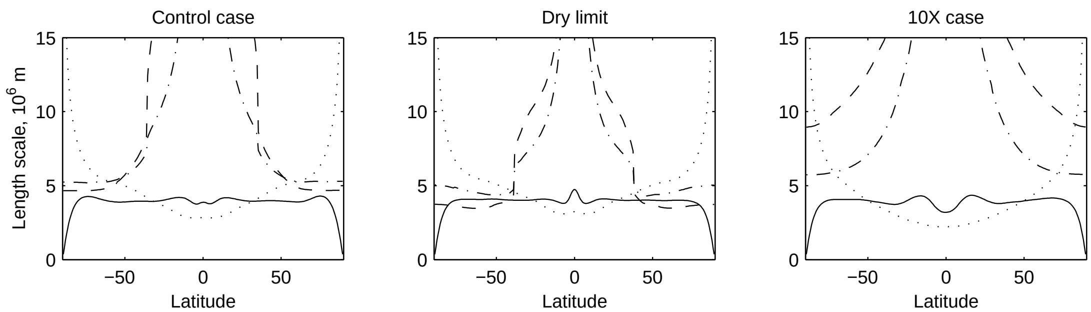

Figure 3.16: Comparison of mean length scale (solid) with theoretical predictions of length scales for the control case, dry limit, and 10X case: Rossby radius using tropopause height (dashed), Rossby radius using scale height (dash-dot), and Rhines scale (dotted).

the bulk dry stability between the surface and tropopause. It exhibits less variation with moisture than the dry stability, but the predicted change in scale is still too large (and in the wrong direction if we accept the small variations in the T170 cases). For instance, it predicts an increase of length scale of approximately 25% from dry to 10X at 45 degrees. These moist Rossby radii do vary relatively little for all of the cases with intermediate values of moisture (6% at 45 degrees); the dry and 10X cases are the primary outliers. We know of no theoretical justification for this choice in any case. As discussed in the introduction, in the Emanuel et al. (1987) theory for the moist Eady model (see also Zurita-Gotor (2005)), the dry stability still controls growth rates and cutoff wavenumbers.

For the dry limit, the Rhines scale is slightly larger than the Rossby radius for all latitudes poleward of the tropopause jump. This difference is small, and we do not see the spectral shapes consistent with an inverse energy cascade that are found in turbulence simulations. Nor do we see clear signs of an inverse energy cascade in our moist simulations. The dry case appears to be broadly consistent with the results of Schneider (2004), in which the static stability adjusts to prevent the supercriticality required to maintain an inverse cascade, and in which there is no separation between the radius of deformation and the Rhines scale. It is possible that our moist experiments could be interpreted in the same terms, if we knew how to best define an appropriate radius of deformation.

The mean length scales of the GCM $\bar{L}$ are on the same order as the Rhines scale in general (but somewhat smaller poleward of the subtropics). Further, the Rhines scale decreases as moisture is added, which is the same behavior as $\bar{L}$ for the T170 cases. However, at any given latitude the Rhines scale varies much more with moisture than does $\bar{L}$, decreasing by 23% at 45° between the dry limit and the 10X case). Another obvious difference is that, while the observed eddy scale $\bar{L}$ is nearly independent of latitude, the Rhines scale increases strongly with increasing latitude.

We suspect that an important factor in determining the length scales in these experiments is the poleward shift of the jet with increased moisture mentioned in Section 3.2. Whereas at 45° latitude the eddy kinetic energy (EKE) is significantly smaller for the 10X case, poleward of the EKE maximum these quantities become similar (see Figure 3.10). The latitudes of maximum EKE are (46, 44, 47, 50, 60, 63) for ξ = (0, 0,5, 1, 2, 4, 10). When we consider the Rhines scale at the latitude with maximum EKE, then these scales are found to be virtually identical. Usage of this scale in the 10X case increases the length scale both by increasing the value of the velocity variance, and, more importantly, by decreasing the value of β. When this expression is used, the theoretical predictions of the length scale for the T170 cases fall within 1% of each other. For the intermediate cases using this scale predicts changes in length of up to 3%, in the correct sense as the observed changes. A summary of all the predicted length scales with ξ, expressed as ratios to the control value, is given in Figure 3.17. Additionally, the increase in EKE can explain the increase in scale seen as resolution is increased from T85 to T170. We believe that the Rhines scale at the latitude of maximum EKE provides a plausible explanation for the observed length scales.

The question of whether there is any additional constraint that makes the length

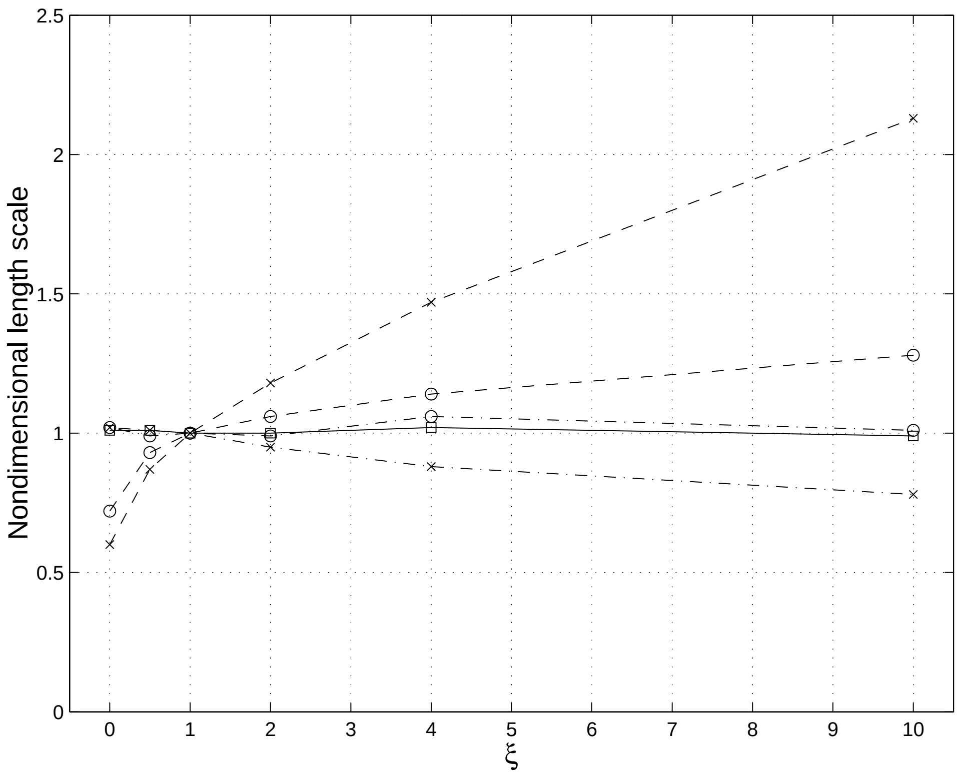

Figure 3.17: Moisture dependence of all length scales discussed in the text, normalized by their respective control values: $\bar{L}$ (solid line with squares), L_{DT} at 45° (dashed line with x's), L_{DS} at 45° (dashed line with o's), L_β at 45° (dash-dot with x's), and L_β at latitude of maximum EKE (dash-dot with o's).

scales invariant remains to be answered. One is tempted to think that the eddy scale is just constrained by the geometry, but it changes when one changes the insolation gradient – it decreases by 10% from the control for $\Delta_{sol} = 1.0$ and increases by 8% for $\Delta_{sol} = 1.8$. It can also be increased by reducing the rotation rate.

3.5 Conclusions

By varying the moisture content of the atmosphere from dry to ten times a control value, we have studied the effect of moisture on the static stability and eddy scales of our moist GCM. The dry stability in the midlatitudes increases significantly as moisture content is increased, suggesting moisture plays a dominant role in determining static stability. To first order, the dry stability of the atmosphere can be approximated by an appropriate moist adiabat. There is additionally some moist stability, which we understand to be determined by the surface variance of moist static energy, as in Juckes (2000). Hence the moist stability increases with moisture content as well, in addition to the large increase in dry stability. Comparisons with observations indicate that the real atmosphere is not far from a moist adiabat as well, and convection could control the static stability. This would indicate that with increased moisture content, we can expect the atmosphere to become more stable to dry perturbations.

Since the dry stability varies greatly with moisture content, we can evaluate the effect of this quantity on eddy scales. Despite the large increase in stability with moisture, the typical eddy length scales (calculated as the vertically integrated spectrum for v') exhibit little variation, with moisture or with latitude. Since the depth of eddies increases significantly with moisture as well, clearly the standard dry Rossby radius is not appropriate. Even a moist Rossby radius, using a constant scale height instead of the tropopause height, cannot capture the proper variation of length scales. Since eddy kinetic energy decreases significantly as moisture is increased, a standard

Rhines scale is not appropriate either. However, when the Rhines scale at latitude of maximum eddy kinetic energy is used, the scale can be accurately predicted. This takes into account the large poleward shift of the jet as moisture is increased, which allows β to increase to compensate.

In the next chapter, we investigate the meridional fluxes fluxes of moist static energy within these same simulations. We additionally propose a theory for the decrease in eddy kinetic energy as moisture is increased, as well as a theory for the latitude of maximum eddy kinetic energy.

Chapter 4

Energy Transports in the Moist GCM

4.1 Introduction

In this chapter we focus on changes in the meridional flux of moist static energy with moisture content. The determination of energy fluxes and meridional temperature gradients is a key problem in climate dynamics, and the effect of moisture on these quantities is particularly important for determining changes in atmospheric circulations in the near future. As temperatures increase with global warming, the moisture content is expected to increase (along with the Clausius-Clapeyron relation, Equation (2.35)), an expectation backed up robustly in global warming forecast models. The increased moisture content gives a larger potential for energy fluxes given the same strength of baroclinic eddies.

The changes in the meridional flux of moist static energy then determine the change in temperature gradients in the atmosphere, i.e., whether the poles will warm more than the tropics, and vice-versa. Although radiative feedbacks (e.g., ice-albedo feedback) are important in the determination of the equator-to-pole temperature difference changes, the dynamical effect of water vapor plays an important role in determining these fluxes as well. Baroclinic eddies then respond in strength to the temperature gradients and help determine the energy fluxes, closing the feedback loop which we study here.

We study the influence of water vapor on the meridional energy transports of energy by varying the moisture content of the atmosphere. We use the same simulations as in Chapter 3, and study the MSE, DSE, and moisture fluxes, and partition into mean and eddy in Section 4.2. We present theories for the changes in fluxes in Section 4.3. Then we examine theories for the diffusivity in Section 4.4, and conclude in Section 4.5. This chapter is joint work with Isaac Held and Pablo Zurita-Gotor. Parts of this chapter appear in Frierson et al. (2005b).

4.2 Energy Transports Varying Water Vapor Content

We present here the energy fluxes from the same simulations as in Chapter 3. Figure 4.1 contains the vertically integrated meridional moist static energy (MSE) fluxes, dry static energy (DSE) fluxes, and moisture fluxes with latitude for $\xi = 0, 1$, and 10 at T170. The intermediate cases $\xi = 0.5, 2$, and 4 are additionally plotted in the DSE and moisture flux plots. Despite the large changes in moisture among the three simulations, the moist static energy transport is nearly identical at every latitude. The moisture transport increases greatly as we increase ξ. However, there is a large amount of compensation of this change in flux by the dry static energy fluxes. A useful method to measure the degree of this compensation is to examine the partition into sensible and latent energy fluxes at the latitude of maximum flux. This latitude is approximately the same for all of the simulations; it is always located between 35 and 37 degrees, as is the total (atmosphere plus ocean) poleward heat transport in observations (Trenberth and Caron, 2001). Table 4.1 lists the fluxes at this latitude for the T170 cases, and Table 4.2 contains the T85 cases. We point out that the amount of compensation (defined by the change in sensible flux divided by the change in latent flux) is almost 99% when going from the dry limit to the control case, and approximately 93% when going from the dry limit to the 10X case. The fluxes are somewhat a function of resolution, especially for the cases with higher moisture content. We note that the compensation improves as resolution is increased. We present theories for this compensation in Section 4.3.

Simulation	MSE flux	DSE flux	Moisture flux	Compensation
$\xi = 0$	5.61	5.61	0	
$\xi = 1$	5.64	2.95	2.69	98.9%
$\xi = 10$	6.03	0.09	5.94	92.9%

Table 4.1: Partition of vertically integrated moist static energy fluxes into sensible and latent components at the latitude of maximum flux (this occurs at 35.4 degrees for the dry limit, 36.1 degrees for the control case, and 36.8 degrees for the 10 times moisture case). Units are $PW = 10^{15}\ W$ for all simulations. Resolution is T170 for all cases.

Despite summing to almost equal MSE fluxes, the DSE and moisture fluxes vary greatly from case to case. In the current climate, the mechanisms which determine the partition into DSE and moisture flux with latitude, combining to create a "seamless" profile of the moist static energy flux have been well-established in observations (Trenberth and Stepaniak (2003a), Trenberth and Stepaniak (2003b)). However as we vary moisture content in these simulations, these mechanisms change vastly, still creating the seamless profile. Clearly since the dry limit has no moisture, its DSE fluxes are the same as the MSE fluxes; these are vastly different from the DSE fluxes with moisture however. The cases with moisture have a well-defined Hadley cell region out to approximately 20 degrees, with strong equatorward transport of moisture, compensated by poleward dry static energy flux. The fluxes within this Hadley

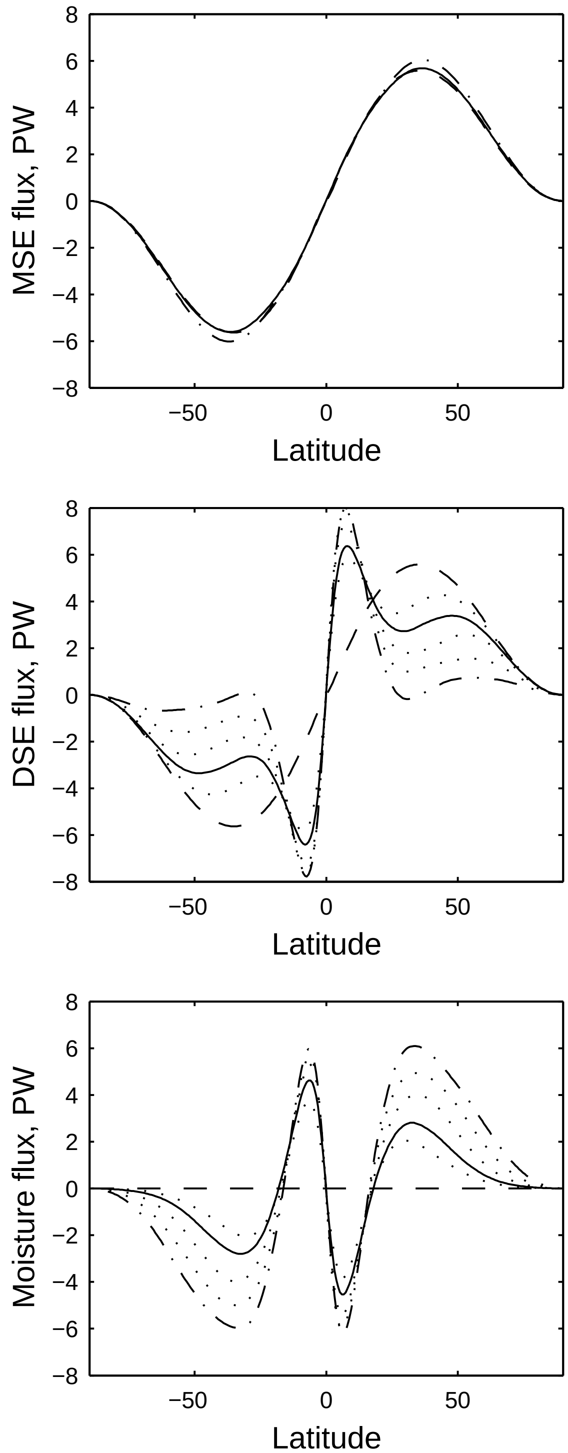

Figure 4.1: Vertically integrated energy transports for the control case (solid), dry limit (dashed), and 10X case (dash-dot). (a) Moist static energy, (b) Dry static energy, and (c) Moisture. Units are $PW(10^{15}\ W)$

Simulation	MSE flux	DSE flux	Moisture flux	Compensation
$\xi = 0$	5.61	5.61	0	
$\xi = 0.5$	5.85	3.99	1.86	87.1%
$\xi = 1$	5.87	2.95	2.92	91.1%
$\xi = 2$	5.85	1.93	3.93	93.64%
$\xi = 4$	6.00	1.11	4.89	92.0%
$\xi = 10$	6.40	0.19	6.21	87.3%

Table 4.2: Partition of vertically integrated moist static energy fluxes into sensible and latent components at the latitude of maximum flux (this occurs at 35.4 degrees for the dry limit, 36.1 degrees for the control case, and 36.8 degrees for the 10 times moisture case). Units are $PW = 10^{15}\ W$ for all simulations. Resolution is T85 for all cases.

cell region only changes slightly in the cases with moisture: there is an increase of approximately 30% in moisture flux from the control case to the 10X case.

Poleward of the Hadley cell, the DSE fluxes decrease and shift poleward as moisture content increases. The 10X case DSE fluxes in the extratropics are nearly zero (actually becoming slightly equatorward around 30 degrees). The latitude of maximum dry static energy flux in the extratropics shifts significantly poleward as moisture content is increased, from 36° in the dry limit to 62° in the 10X case. The moisture flux maxima all occur at approximately the same latitude: between 30° and 34° for all cases. The moisture fluxes increase significantly in the extratropics for the cases with moisture, but not by a factor of 10. Between 20 and 40 degrees, the moisture fluxes are approximately twice as much in the 10X case compared to the control case. This ratio of moisture fluxes between the 10X case and control case then increases to a factor of 7 near the pole.

There are several reasons why the moisture fluxes increase by so much less than a factor of ten when the saturation vapor pressures are increased by this factor. A key element of this involves the changes in temperatures in the 10X case and other cases with higher moisture content. The lower tropospheric temperatures decrease strongly in the 10X case, while in the upper troposphere there is a significant increase (the mean temperature cannot change much because the insolation is the same, and the vertical structure changes are due to changes in the moist adiabat). Due to this decrease in lower tropospheric temperatures, the moisture content of the atmosphere only increases by around a factor of 5 to 6 for much of the troposphere in the 10X case. In addition to this, the strength of the mean circulation and the eddies decrease in the 10X case. The strength of the Hadley cell is reduced by a factor of two, and the maximum eddy kinetic energy in midlatitudes decreases by over a factor of two. These two factors combine to explain the moderate increase in moisture fluxes. Within the Hadley cell, there is an additional factor which contributes to the very modest increase of the moisture fluxes there of only 30%. This additional effect is the moisture content at the outflow level: while negligible for the control case, the specific humidity outflow for the 10X case is half as much as the lower layer humidities. This results from the strongly decreased lapse rates in the 10X case.

Figure 4.2 gives the decomposition of the total flux into mean and eddy components for the T170 simulations. The midlatitude transport is primarily due to eddy fluxes in all cases. There is a Ferrel cell present in the midlatitudes in each simulation, seen in the equatorward MSE transport by the mean flow. The MSE transport by the mean Hadley cell varies greatly with water vapor concentration. The Hadley cell actually transports energy equatorward in parts of the deep tropics in each of these simulations, with more equatorward transport over a wider area as moisture concentrations increase. The deep tropical region of equatorward transport extends to 2.2 degrees in the dry limit, 4.2 degrees in the control case, and 8.7 degrees in the 10X case (although this case actually changes sign twice in the deep tropics). This equatorward flux is balanced by strong eddy moisture fluxes in each of the moist runs,

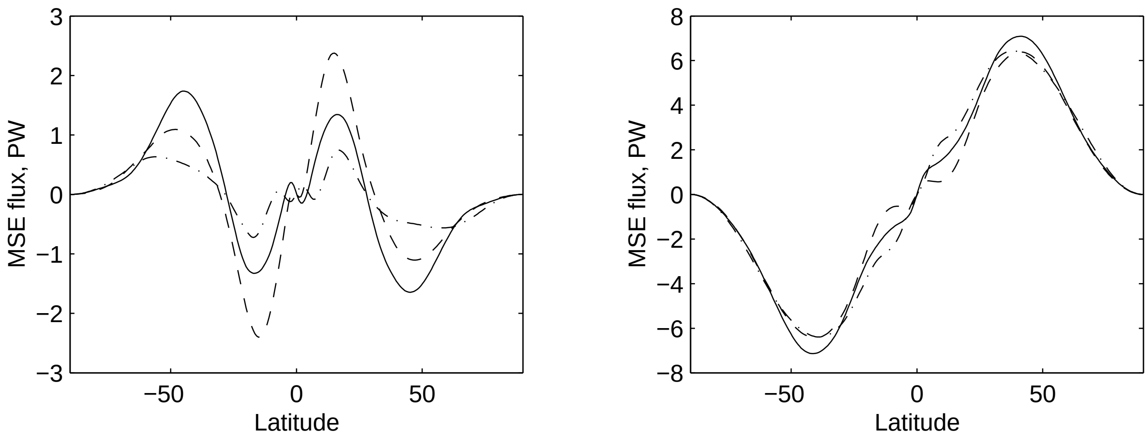

Figure 4.2: Vertically integrated moist static energy transport for the control case (solid), dry limit (dashed), and 10 times moisture case (dash-dot) (a) by the mean flow and (b) by eddies. Units are PW for all simulations, note the different scales for each plot.

and small eddy fluxes of dry static energy in the dry case so that the total energy transport is poleward always.

A useful diagnostic when studying of the energy transports by the Hadley cell is the gross moist stability (Neelin and Held, 1987), which is the amount of energy transported per unit mass transport by the circulation, i.e.,

$$\Delta m = \frac{\int_0^{p_s} \bar{v}\bar{m}dp}{\int_{p_m}^{p_s} \bar{v}dp} \tag{4.1}$$

where Δm is the gross moist stability, m is the moist static energy, p_s is the surface pressure, and p_m is some midtropospheric level (defined so that the equatorward mass flux occurs mostly below this level, and the poleward mass flux occurs above). Since we are considering the zonally and time averaged flow, unlike Neelin and Held, we can use the meridional velocity as the weights in this calculation. Using the divergence as a weight gives similar results. We plot the gross moist stabilities for each of these simulations in Figure 4.3. For the dry limit, the gross moist stability is almost exactly zero at the equator (less than .1 K), and increases slowly away from this, reaching

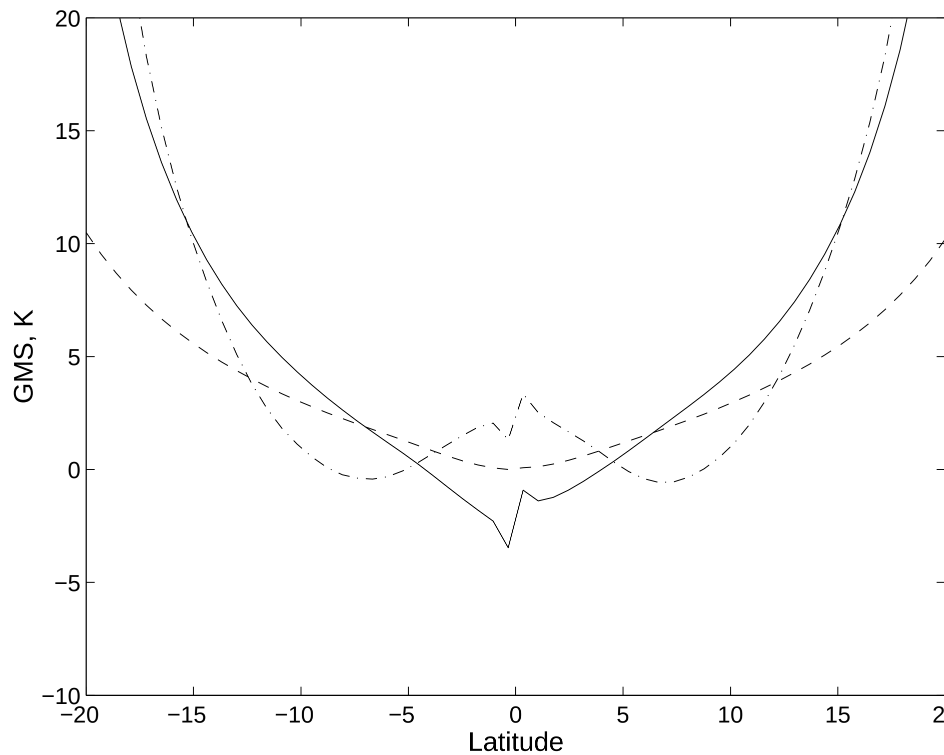

Figure 4.3: Gross moist stability for the three simulations (units of temperature in K).

5.6 K at 15 degrees. The control case is more strongly negative at the equator (-2.2 K), and becomes positive more quickly away from the equator. The 10X case begins slightly stable at the equator, then becomes negative out to 8.7 degrees (the asymmetry between hemispheres in these two cases is due to the mass transport in the denominator of this expression approaching zero at the equator). A consistent picture of this behavior and the area of equatorward transport is that our large scale condensation scheme creates a highly unstable tropics which transports energy towards the source of the convection, as in CISK theories (Charney and Eliassen, 1964). Even a strong Hadley circulation then cannot flatten temperature gradients, and eddies flux significant amounts of latent heat poleward. In the dry limit, in contrast, the temperatures are essentially on the same dry adiabat in the tropics, implying zero static stability at the equator, and small eddy fluxes.

4.3 Theories for the Compensation and Energy Balance Models

4.3.1 Extreme Cases

We have demonstrated in Section 4.2 that there is remarkable compensation of the change in latent energy fluxes as we vary moisture by changes in sensible heat fluxes. We would like first to put into context how large this compensation is by considering some extreme cases. Given the net shortwave radiation at the top of the atmosphere and the OLR, the moist static energy flux is:

$$F(\phi) = 2\pi R^2 \int_0^{\phi} (Q_{SW} - I) cos\phi^* d\phi^* \tag{4.2}$$

where F is the flux, ϕ is latitude, R is the radius of the Earth, Q_{SW} is the shortwave heating, and I is the outgoing longwave radiation (OLR). The lower limit for energy fluxes is obviously zero in radiative-convective equilibrium when $Q_{SW} = I$, although we never expect this limit to be approachable unless latitudinal gradients of solar radiation are made very weak, since the radiative-convective equilibrium temperature profile is otherwise unstable. Another interesting limit is fixed OLR with latitude, i.e., that the energy fluxes have flattened the temperatures at the radiative emission level. This is actually not a strict upper limit in our model; some extreme cases with optical depths strongly a function of latitude have reversed temperature gradients at the emission level (but not at the surface). However this limit is still interesting to consider. Substituting in the shortwave radiation profile used in our model, and the proper uniform OLR to ensure global energy balance (234.6 Wm^{-2}), one obtains 7.82 PW for the maximum flux. One might wonder if the fluxes vary little because they are all close to this limit; this is a primary argument in Stone (1978b) to explain the invariance of fluxes in GCM simulations. For this model, the fluxes are sufficiently far from this limit, and remain unchanged to a much higher degree for this to be the only factor contributing to the compensation.

4.3.2 Energy Balance Model

Therefore to interpret this compensation of energy fluxes with a simpler model, we introduce a one-dimensional energy balance model (EBM) in which all of the energy transport is diffusive (Budyko (1969); Sellers (1969)). The assumption of diffusive energy transport, that the flux is everywhere proportional to the local gradient, is evaluated for the dry case in Pavan and Held (1996). The form of the energy balance model is:

$$\begin{aligned} \frac{\partial m}{\partial t} &= Q_{SW} - Q_{LW} + D\nabla^2 m \\ &= Q_{SW} - Q_{LW} + \frac{D}{a^2 cos(\theta)} \frac{\partial}{\partial \theta}\left(cos(\theta) \frac{\partial m}{\partial \theta} \right) \end{aligned} \tag{4.3}$$

where m is some appropriate moist static energy to be diffused, Q_{SW} and Q_{LW} are the shortwave radiative heating and outgoing longwave radiation, respectively, a is the Earth radius, θ is the latitude, and D is some appropriate diffusion coefficient. Lapeyre and Held (2003) discuss results for why lower layer values of moist static energy are most appropriate for diffusive models of energy fluxes; therefore we take m to be the moist static energy just above the surface.

$$\begin{aligned} m &= c_p T_s + L_V q_s \\ &= c_p T_s + RH_s L_V q_s^* \\ &= c_p T_s + RH_s L_V \xi \frac{R_d e_{s0}}{R_V p_s} exp\left(-\frac{L_V}{R_V} \left(\frac{1}{T_s} - \frac{1}{T_0}\right) \right) \end{aligned} \tag{4.4}$$

where the subscripts s represent surface values, q_s^* is the saturation specific humidity at the surface, and RH_s is the surface relative humidity.

4.3.3 Energy Balance Model with Exact Compensation

Interestingly, the simplest energy balance model we present has the property of exact compensation: energy fluxes do not change as we vary moisture content through the parameter ξ. This model uses the following assumptions in addition to the above: first, that the diffusivity D does not change as we vary moisture content. Second, the effective level of emission (the level where the temperature $= (\frac{Q_{LW}}{\sigma})^{\frac{1}{4}}$, where σ is the Stefan-Boltzmann constant) does not change as we vary ξ. This is an excellent approximation for our GCM since the optical depths in our gray radiation scheme are the same for all of our simulations. Third, we assume that all water vapor has condensed out at the emission level. This assumption is reasonable since the emission level in our GCM is observed to be well above the e-folding depth for water vapor (our emission level is around 500 mbar, similar to the real atmosphere). Finally, we assume that the parcel has the same moist static energy at the emission level as it does at the surface. This is a reasonable starting point, since the moist isentropes in our model are close to vertical from the midlatitudes poleward, the key result in Chapter 3. While none of these four assumptions are satisfied exactly in the GCM, we find this a useful starting point, since the energy flux in this model is independent of ξ.

Proof: The EBM can be written as:

$$\frac{\partial m}{\partial t} = Q_{SW} - \sigma T_E^4 + D\nabla^2 m \tag{4.5}$$

where T_E is the emission temperature. Under the assumption of moist adiabatic ascent above, $c_p T_E = c_p T_s - g z_E + L(q_s - q_s(z_E))$. Further, with the assumption that all the water vapor has condensed out by the emission level, $q_s(z_E) = 0$, and the above can be rewritten as:

$$c_p T_E = m - g z_E \tag{4.6}$$

Substituting into the EBM, we have:

$$\frac{\partial m}{\partial t} = Q_{SW} - \sigma(m - gz_E)^4 + D\nabla^2 m \quad (4.7)$$

Nothing in this equation is a function of ξ; therefore there is a unique steady solution for m, the flux of m, the OLR, etc. Changing ξ only changes the partition of the fluxes into latent and sensible.

4.3.4 Refinements to the Energy Balance Model

Unfortunately, none of the assumptions in this simple EBM are exactly true in the GCM. Further, our model does not exhibit exact compensation. We therefore modify our theory to understand our GCM further. We first relax the assumption that all moisture has condensed out by the emission level, and calculate actual moist adiabats to get the emission temperature. To start, we specify the emission height to be $5km$ at all latitudes. We additionally assume that the diffusion coefficient is independent of latitude, and tune its value to match the maximum flux in the control case to that of the GCM. This value is $D = 6.1 \times 10^6 \frac{m^2}{s}$. The fluxes are well-predicted globally in the control case when the maximum flux is matched (accurate to within 3% outside of the deep tropics). However, the surface moist static energy gradient in the EBM is much weaker than in the GCM.

To correct the surface moist static energy structure, we next run the EBM with the emission heights from the control run of the model inputted. The emission level peaks at the equator with a value of approximately 6 km, and has a minimum at the poles of 1.5 km. The emission levels in our model change little from simulation to simulation, since the optical depths for radiation do not change. Therefore we use this emission level for all cases.

For the control case, putting this function into the EBM implies that a much smaller value must be used for the diffusion coefficient in order to produce the same energy fluxes, $D = 1.84 \times 10^6 \frac{m^2}{s}$ in this case. Less diffusion is needed since surface moist static energy gradients are amplified given the emission level temperature when there are lowered emission levels near the pole. The fluxes are again well-matched for all latitudes for this case, and the surface moist static energy gradients are now close to the GCM value as well. The primary deficiency here is that the ratio of moisture flux to dry static energy flux is larger than the GCM value. This can be attributed to the neglect of the moist stability, which causes the EBM surface temperatures (and hence the moisture content and moisture gradients) to be slightly too large. However, due to the large increase in complexity that would be needed to model the static stability and its spatial structure, we find this model of the control case adequate. We emphasize that adding a latitudinally constant moist stability to this model keeps the moist static energy flux the same, but does affect the partition into dry and moist. We therefore focus on the moist static energy fluxes as much as possible.

We therefore proceed by using the same diffusion coefficient and emission level profile in the dry limit and the 10X case. The fluxes for these cases are plotted in Figure 4.4. Clearly there is much less compensation present in this version of the EBM. The maximum fluxes now range from 5.26 PW for the dry limit to 7.22 PW for the 10X case, and the compensation is down to 67.4% going from the dry limit to the 10X case. The relevant values of the fluxes and compensations for this case are listed in Table 4.3. We point out that despite the changes in the maximum value, the fluxes again have a very similar structure. This reaffirms the result of Stone (1978b) that the fluxes are insensitive to the structure of the diffusivity.

Anticipating that the next most important effect is changes in the diffusivity, we now examine the effective diffusivities found in the GCM, both to refine the energy balance model further and to test these values with theories for the diffusivity such

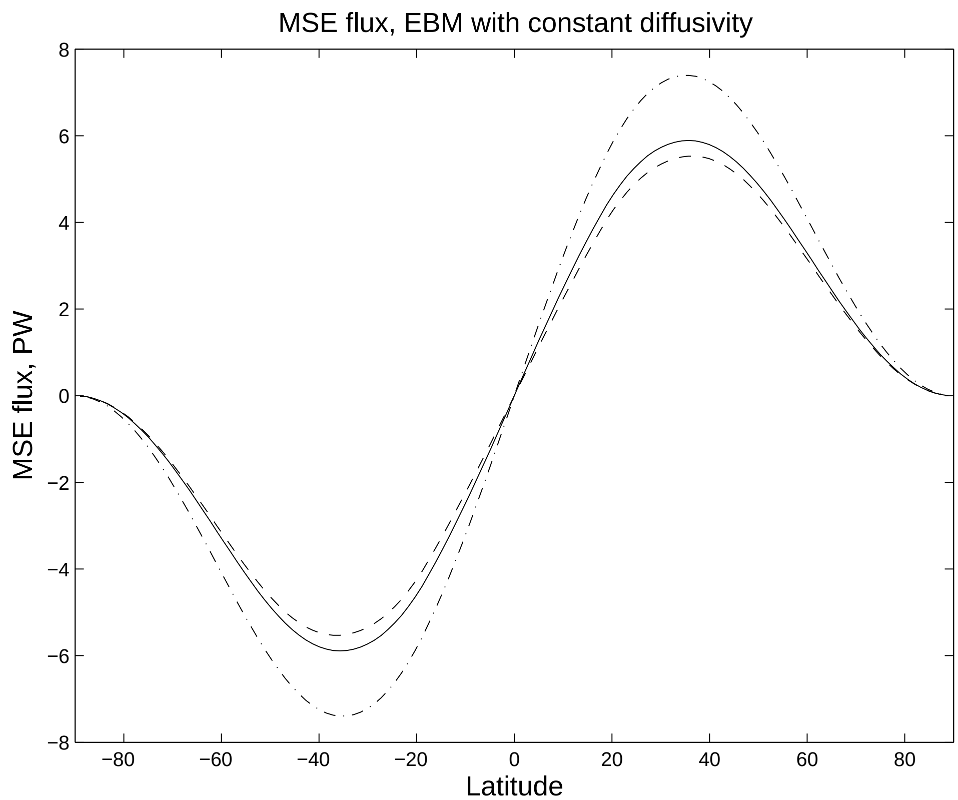

Figure 4.4: MSE fluxes from energy balance model with uniform diffusivity and emission heights from the control run of the GCM (solid=control, dashed=dry limit, dash-dot=10 times moisture).

EBM	MSE flux	DSE flux	Moisture flux	Compensation
DRY	5.26	5.26	0	
CTRL	5.63	2.61	3.02	87.7%
10X	7.22	1.22	5.99	67.4%

Table 4.3: Maximum moist static energy fluxes of the EBM with constant diffusivity of $1.84 \times 10^6 \frac{m^2}{s}$, and partition into sensible and latent components at the latitude of maximum flux (this occurs at 37.1 degrees for the dry limit, 35.7 degrees for the control case, and 35.7 degrees for the 10 times moisture case). Units are $PW = 10^{15}\ W$ for all simulations.

as Held and Larichev (1996) and Barry et al. (2002). We define the diffusivity as the vertically averaged flux of moist static energy divided by the gradient of moist static energy at the surface, i.e.,

$$D_{GCM} = \frac{\frac{1}{\Delta p}\int_{p_s}^{0} \overline{vm} dp}{\frac{1}{a}\frac{\partial m}{\partial \theta}|_{p_s}} \tag{4.8}$$

where Δp is an appropriate pressure depth of the troposphere (taken to be $800hPa$ here). These effective diffusivities are plotted in Figure 4.5. There is a clear decrease in the effective diffusivity as moisture is added into the atmosphere. When area-averaged away from the tropics (poleward of 25 degrees), the mean value of the diffusivity are $1.87 \times 10^6, 2.09 \times 10^6$, and $1.26 \times 10^6 m^2 s^{-1}$ for the control case, the dry limit, and the 10X case, respectively. We note that the value for the control case is very similar to the value which worked best in the EBM, $1.86 \times 10^6 m^2 s^{-1}$. These GCM values are somewhat sensitive to the latitudinal domain used for averaging, due to the fact that the spatial structure of these diffusivities are complex. The global minima occur in the tropics for all cases, with abrupt increases in diffusivity within the tropics in the dry limit and control case. Diffusivities become negative in the deep tropics for the 10X case due to a very slight surface moist static energy gradient reversal. We do not expect the diffusion hypothesis to be relevant in these areas, where Hadley cell dynamics dominate the energy transports. Both the control case and 10X

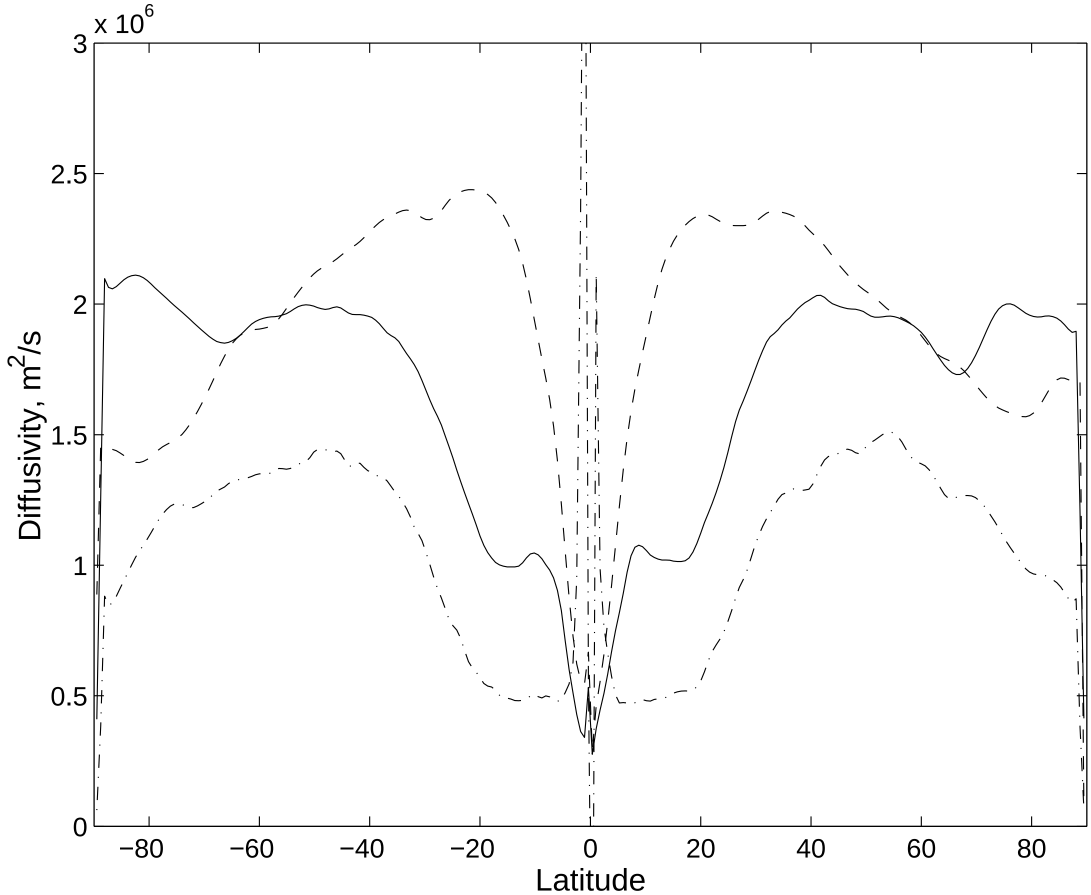

Figure 4.5: Effective diffusivities from the GCM (solid=control, dashed=dry limit, dash-dot=10 times moisture, units are m^2/s).

case plateau over the subtropics, and increase to broad maxima of diffusivity between 40 and 60 degrees. This behavior is not observed for the dry limit; here the global maximum occurs in the subtropics at 20 degrees and there is a secondary maximum at 33 degrees. The control case actually surpasses the dry limit diffusivity near the poles. For the T85 cases, the average diffusivities are 2.09, 2.03, 1.92, 1.74, 1.51, and 1.27 $\times 10^6 m^2/s$ for ξ = 0, 0.5, 1, 2, 4, and 10, respectively. This demonstrates the relative robustness of this statistic as resolution is increased, as well as the gradual decrease of diffusivity as moisture is increased.

We next investigate the sensitivity of the EBM to the diffusivity, first by calculating what value of the diffusivity is required in each case to reproduce the maximum flux of the GCM. Varying the diffusivity to reproduce the GCM fluxes, we find that the values required by the EBM in the 10X case and the dry limit are remarkably close to the actual GCM values. When the control emission height is used for all cases, the required diffusivities are $2.05 \times 10^6 m^2 s^{-1}$ for the dry limit, and $1.10 \times 10^6 m^2 s^{-1}$ for the 10X case. This agreement suggests that a theory for the change in diffusivity is the only remaining component to explain the compensation seen in our GCM. Changes in static stability, emission level, and the structure of the diffusivity are secondary to changes in the mean diffusivity in explaining the behavior of the GCM, because the structure of the fluxes is quite insensitive (Stone, 1978b).

To get an idea of the sensitivity of the fluxes to the diffusivity within the EBM, we run this model over a wide range of diffusivities. The maximum moist static energy flux as a function of diffusivity is plotted in Figure 4.6. Each point on this plot represents one steady state of the EBM. When the diffusivity is small, the fluxes go to zero and the model is in radiative equilibrium. In the other extreme limit, the surface temperature and moist static energy have become homogenized. This corresponds to a reversed OLR gradient due to the emission height structure with latitude. The flux asymptotes to a smaller value for the 10X case due to the reduced temperature lapse rate up to the emission level, creating a smaller OLR reversal, and a smaller fluxes. Provided the diffusivity is not very small, the latitudinal structure of the fluxes is very similar over this wide range of diffusivities. The maximum flux always occurs within 2 degrees of 36 degrees provided the diffusivities are greater than $9 \times 10^5 m^2 s^{-1}$.

It is clear from Figure 4.6 that the maximum fluxes are quite sensitive to changes in diffusivity at their current state: in fact, each are at approximately their most sensitive point in the domain of diffusivities. The 10X case is most sensitive to diffusivity for small values of diffusivity, due to the strong positive feedback of moisture on surface moist static energy gradients as surface temperature gradients increase. Our

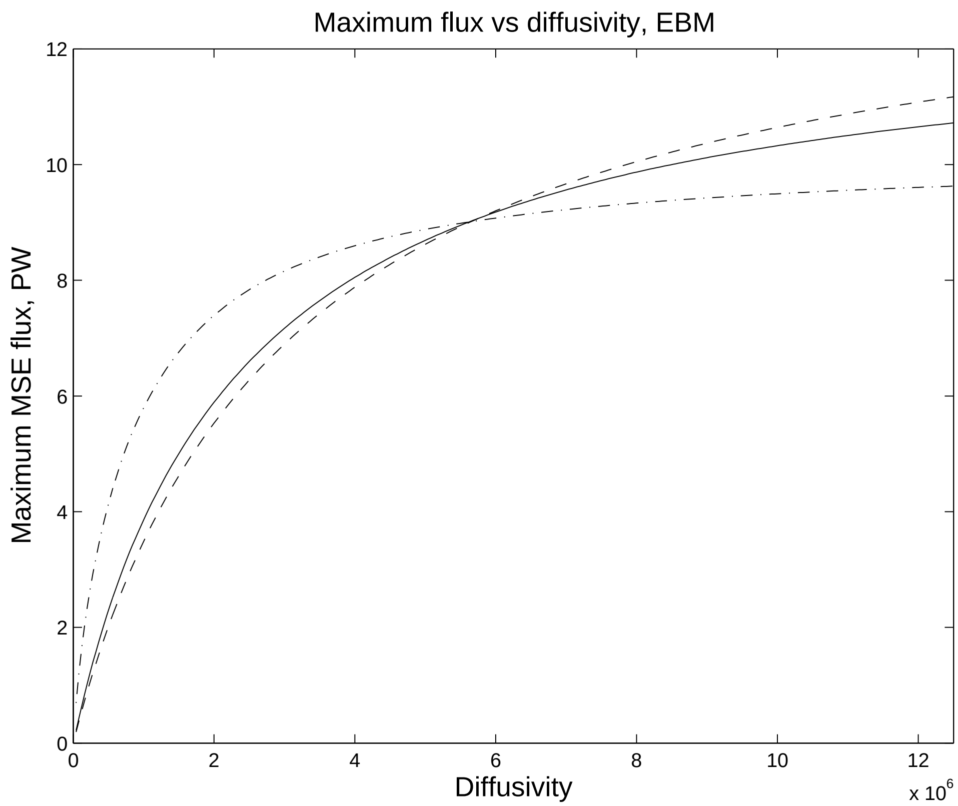

Figure 4.6: Maximum flux (in PW) with diffusivity (in m^2/s) from the EBM.

conclusion from this plot is that the change in diffusivity from case to case is clearly important for the observed invariance of fluxes. We therefore proceed with a theory for the diffusivity.

4.4 Theory for Diffusivity

Eddy diffusivity theories are based on the principle that perturbations in the quantity being mixed can be written as a mixing length times the mean gradient of the quantity, in this case, that

$$|m'| = -L_{mix}\frac{1}{a}\frac{\partial \bar{m}}{\partial \theta} \tag{4.9}$$

Then the eddy diffusivity is calculated as the following:

$$D = kL_{mix}|v'| \tag{4.10}$$

where k is a correlation coefficient between v and m, and $|v'|$ is the typical fluctuation of the meridional velocity. In the past, theories have been developed using length scales including the Rhines scale (Held and Larichev (1996), Barry et al. (2002)), the Rossby radius (Stone (1972)), the scale with maximum growth in the Charney problem (Branscome (1983), Stone and Yao (1990)), and the width of the baroclinic zone (Green (1970), Haine and Marshall (1998)). These studies have used scales for the meridional velocity fluctuation including the mean zonal wind (Stone (1972), Haine and Marshall (1998)), scales based on equipartition of kinetic energy (Green (1970)), or scales based entropy production and the kinetic energy cycle (Barry et al. (2002)).

In Chapter 3 we have found that the length scales of the GCM, measured by the spectrum of the vertically averaged variance of the meridional velocity, are remarkably constant, both with latitude, and with changes in moisture. We interpret this with the Rhines scale at the latitude of maximum eddy kinetic energy. We first investigate whether this length scale times the pressure averaged RMS meridional velocity at this maximum latitude gives an adequate description of the changes in diffusivity, i.e., whether the correlation coefficient is relatively constant from case to case. The pressure-averaged RMS meridional velocity at latitude of maximum eddy kinetic energy (EKE) are the following: 11.44 m/s for the dry limit, 11.36 m/s for the control case, and 7.75 m/s in the 10X case. The latitude of maximum eddy activity shifts poleward as moisture is added: from 46 degrees in the dry limit, to 47 degrees in the control case, to 63 degrees in the 10X case. Multiplying the velocities by the average length scales quoted in the Chapter 3 (4000, 3960, and 3910 km in the dry limit, control, and 10X case) gives a diffusivity in the dry limit that is 1.02 times the control case, and the diffusivity in the 10X case that is .67 times the control case. We compare this with the ratios of 1.12 and .67 for the GCM diffusivities. Due to the arbitrariness of selection of the area for averaging for the diffusivities and length scales (poleward of 25 degrees), we are satisfied with these values as approximations to the diffusivity. It should be mentioned that simply multiplying the length and velocity scales together gives a value approximately 25 times the actual diffusivity. This is partially due to the correlation coefficient between v and m, but is primarily because the surface mixing length is significantly smaller than the length scale for v. Discussion of the smaller scales for surface mixing lengths can be found in Swanson and Pierrehumbert (1997).

If we consider the length scale to be the Rhines scale at the latitude of maximum EKE, then all we need for a complete theory of the diffusivity (and hence the temperature profile and fluxes from the EBM) is a theory for the latitude of maximum EKE, and the RMS velocity there. In Chapter 3 we have shown that the static stability is near neutral in terms of moist stability from the midlatitudes equatorward. However, there is some moist stability in the midlatitudes that increases as moisture is added.

Further, the atmosphere is very stable in the polar regions. Lacking a simple unified theory for this behavior, we investigate whether a simple theory for the diffusivity can be obtained without considering the determination of the moist stability. This is consistent with the level of complexity of the EBM as presented so far, which assumes moist neutrality everywhere.

The theory for the latitude is based on midtropospheric values of the shear minus the critical shear for baroclinic instability from the two-layer model, $(\frac{\partial U}{\partial z})_{crit} = \frac{\beta N^2 H}{f^2}$. These quantities at 560 mbar are plotted in Figure 4.7. The maximum difference of the shear and the critical shear captures the movement of the latitude of maximum EKE quite well, with the predicted latitudes occurring at 41 degrees, 47 degrees, and 70 degrees for the dry limit, control case, and 10X case respectively. There is slightly more movement of the jet latitude than observed in the GCM. The usage of the two-layer model critical shear in this expression may seem somewhat arbitrary. However, in Figure 4.7 the primary factor in this movement is the change in shears, not the critical shears. The usage of the critical shear simply eliminates the subtropical jet at the edge of the Hadley cell from being falsely selected. Further, the large changes in dry static stability among these three cases affect this latitude only minimally. Rather the stabilizing effect of $\frac{1}{f^2}$ in the subtropics is the primary effect of this term.

We base our theories for $|v'|$ on the thermal wind relation in the zonal direction:

$$f \frac{\partial v}{\partial z} = \frac{g}{T_0} \frac{\partial T}{\partial x} \tag{4.11}$$

This can be scaled in terms of the meridional temperature gradient as follows:

$$v \sim \frac{gH}{fT_0} \frac{L_y}{L_x} \frac{\partial T}{\partial y} \tag{4.12}$$

where L_y and L_x are appropriate length scales in the meridional and zonal directions, respectively. One can either assume that the length scales do not change much from

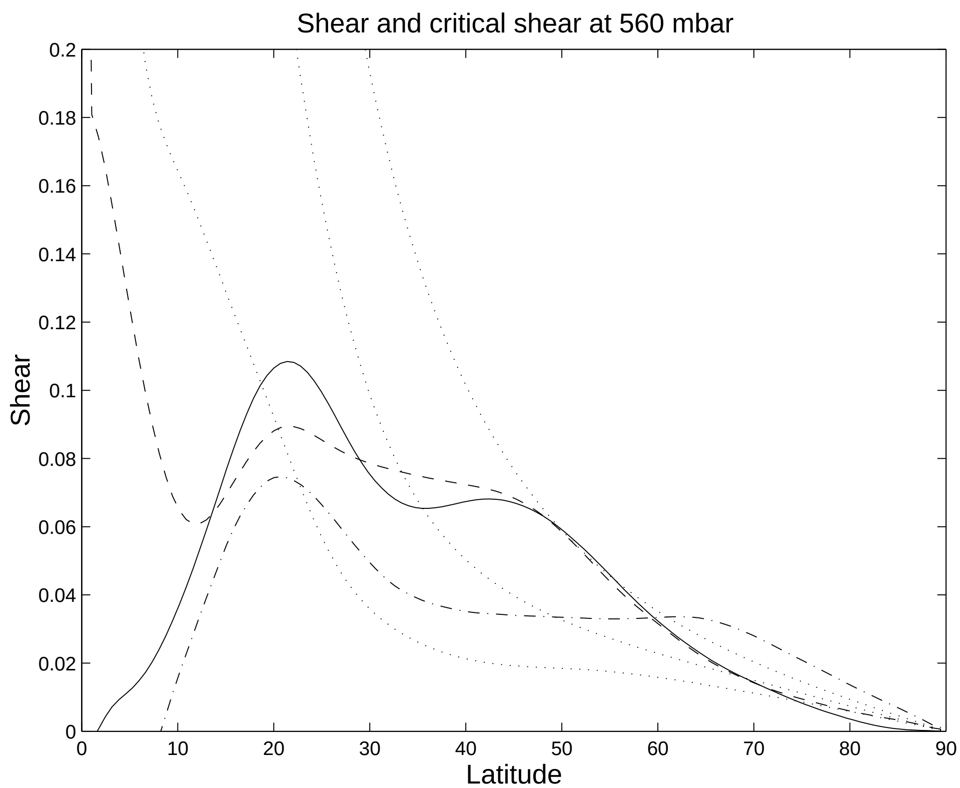

Figure 4.7: Shear and critical shear (dotted) for the two layer model at 560 mbar. The critical shears increase with moisture, i.e., the top dotted curve is the critical shear for the 10 times moisture case.

case to case, or that $L_y = L_x$ to justify our scaling for v:

$$v \sim \frac{1}{f}\frac{\partial T}{\partial y} \tag{4.13}$$

This theory is equivalent to assuming equipartition of mean dry available potential energy and eddy kinetic energy. Using this scale at the latitudes predicted above give ratios to the control case of 1.11 for the dry limit and .43 for the 10X case; using this scale at the latitudes of maximum EKE in the GCM gives ratios of 1.04 for the dry limit and .52 for the 10X case.

We next run the EBM predicting everything based on these theories: the latitude of maximum EKE, the RMS meridional velocity, the length scale, and the diffusivity. These are predicted at each time step, and run until converged. The diffusivity is tuned in the control case, and this value is then used in the dry limit and the 10X case. It is necessary to assume a small background dry stability so the dry limit is not singular; we choose a dry stability of 1.5 K/km for this purpose. The cases with moisture are insensitive to this value, and the dry limit is only somewhat sensitive to it, mostly in the calculation of the latitude. This full EBM converges for all these cases, and the results for the fluxes are the following: dry limit flux = 5.6 PW, 10 times flux = 6.5 PW. The compensation is less for the 10X case, but is quite reasonable for the dry limit. Further, the movement of the latitudes of maximum EKE are well-predicted by this model: they are found to be 35.7 degrees, 45.5 degrees, and 65.1 degrees for the dry limit, control case, and 10X case, respectively.

4.5 Conclusions

In this chapter we have studied the meridional fluxes of moist static energy as moisture content is increased. The moisture fluxes increase with moisture as expected; however there is an accompanying decrease in dry static energy fluxes, leaving the total moist static energy flux remarkably unchanged, both in terms of structure and magnitude of fluxes. The compensation is approximately 99% from the dry limit to the control case, while the total fluxes in the 10X case increase slightly (giving 93% compensation from the dry limit). The compensation is remarkable given the large changes in many aspects of the climate among these simulations: as moisture content is increased, the dry stability increases, the jet shifts poleward, the eddy kinetic energy is reduced, and the Hadley circulation weakens.

We investigate several reasons for this compensation. Firstly, as shown in Stone (1978b), the structure of the fluxes is not expected to vary much. The essential structure of the moist static energy fluxes is given by the flux implied by flat OLR with latitude: this gives nearly the exact structure of the fluxes in observations as well as in this model. Stone (1978b) additionally shows that structure in the OLR function projects only weakly onto the structure on the fluxes; changes in OLR project essentially only onto the magnitude of the fluxes with the same structure as for flat OLR.

The fact that the structure of the fluxes cannot vary much is a key simplification for idealized models of the moist static energy fluxes. This allows one to describe the entire latitudinal profile of the fluxes with only one value, for instance, the maximum flux. We use one-dimensional diffusive energy balance models as a basis for theories of the energy fluxes; the approximation of fixed structure allows us to use a globally averaged diffusivity to capture the behavior of the fluxes.

An energy balance model with four assumptions, all of which are approximately satisfied within the full model, has the property of exact compensation as moisture content is changed. This model consists of fixed diffusivity, fixed emission level, neutral moist stability to the emission level (as shown in Chapter 3), and all moisture condensed out by the emission level. We provide a mathematical proof for the invariance of fluxes in this case. These assumptions essentially provide the explanation for the invariance of fluxes as moisture content is decreased from the control value.

In order to explain the near-equality of fluxes in the 10X case, one must consider the change in diffusivity with moisture content. The diffusivity is found to decrease by approximately one-third from the control case to the 10X case, and using this value within the EBM gives the proper degree of compensation. We find that changes in moist stability and emission level are secondary to the change in diffusivity in explaining the compensation. As in standard mixing length theories, we write our theory for the diffusivity as the product of a length scale times a velocity scale. The length scale is taken to be the Rhines scale at latitude of maximum EKE, as in Chapter 3. The latitude of maximum EKE is chosen to be the latitude with maximum shear minus critical shear for the two-layer model. The theory for the velocity scale is based on the thermal wind relation in the zonal direction: while this underestimates the velocity in the high moisture cases, there is approximate agreement. We believe the underestimate is due to the neglect of moisture as an available potential energy source. This may be remedied in the future by consideration of some appropriate moist APE. An EBM that includes all of these effects is able to qualitatively reproduce the poleward shift of the jet, the reduction in EKE, the reduction in diffusivity, and near-equality of fluxes with moisture content.

In the next chapter we shift our focus to tropical dynamics, where latent heating and moisture plays an even more fundamental role. We begin by constructing a simple model of large-scale precipitation and moisture dynamics in the tropics. The derivation of this model begins from the Boussinesq equations, and is given from an applied mathematics perspective. The key assumption of the model is truncated vertical resolution into two modes, using the Galerkin method. Moisture dynamics are truncated into one equation for the vertically integrated water vapor content, and condensation heats the first baroclinic mode. After the derivation is presented, we additionally consider energy conservation laws for the simple system, and use these to make statements about what kind of discontinuities can develop within the system.

Chapter 5

A Simple Mathematical Model of Large-Scale Tropical Moisture Dynamics

5.1 Introduction

One of the striking observational discoveries over the last few decades is the profound impact of the interaction of water vapor and planetary scale dynamics in the tropics on monthly, seasonal, and even decadal prediction of weather and climate in the mid-latitudes (Madden and Julian (1994); Waliser et al. (2003)). Full GCM's have been somewhat unsuccessful at simulating these interactions on time scales appropriate for seasonal prediction as well as climate change projections (Slingo and coauthors, 1996). Given the complexity of full GCM's, one important theoretical thrust in the atmospheric science community is the development of simplified models for the parameterization of the interaction of moisture and large scale dynamics which retain fidelity with crucial features of the observational record (Emanuel (1987); Neelin and Held (1987); Neelin et al. (1987); Yano and Emanuel (1991); Emanuel et al. (1994);

Yano et al. (1995); Majda and Shefter (2001b); Majda and Shefter (2001a); Majda et al. (2004)). These simple theories fit into the hierarchy of models described in Chapter 1 near the lowest levels of of complexity.

The main thrust of this chapter is to develop a simple mathematical model for the study of precipitation regions in the tropics, from a large scale dynamical perspective motivated by the work mentioned above. In Section 5.2, we present a detailed derivation, starting from the Boussinesq equations and the equations for bulk cloud microphysics, of a family of simplified prototype tropical climate models for the interaction of moisture with large scale dynamics. In spirit these models have similar features to the QTCM of Neelin and Zeng (2000) but a detailed systematic self-contained derivation is merited as an introduction to these topics for the applied mathematics community. The simplified equations have the form of a shallow water equation and a scalar equation for moisture coupled through a strongly nonlinear source term. This term, the precipitation, is of relaxation type in one region of state space for the temperature and moisture while the nonlinearities vanish identically elsewhere in the state space. In addition, these equations are coupled nonlinearly to the equations for barotropic incompressible flow in two horizontal space dimensions. In Section 5.3, several mathematical features of this system are developed including energy principles for solutions and their first derivatives independent of relaxation time. We then use this model in Chapter 6 to study the dynamics of precipitation fronts in the tropical atmosphere.

5.2 Model Equations and Physical Parameterizations

5.2.1 The Hydrostatic Boussinesq Equations on the Equatorial β-plane

We begin with the constant buoyancy frequency version of the hydrostatic Boussinesq equations on the equatorial β-plane as the dynamical core for simplicity. The Boussinesq equations are obtained by expanding the Navier-Stokes equations in a power series about a background state which is a function of height. This filters the fast and meteorologically insignificant sound waves from the system. The hydrostatic approximation of the vertical momentum equation, which is justified by the small aspect ratio of the flow, is additionally employed. The equatorial β-plane approximation is a linearization of the Coriolis parameter about the equator (where it is zero). See texts such as Gill (1982), Pedlosky (1987), and Majda (2003) for derivations and further discussion of these models.

The hydrostatic Boussinesq equations on a β-plane are as follows:

$$\begin{aligned} \frac{D\mathbf{U}}{Dt} &= -\beta y \mathbf{U}^{\perp} - \nabla p + S_{\mathbf{U}} && (5.1) \\ \nabla \cdot \mathbf{U} + \frac{\partial w}{\partial z} &= 0 && (5.2) \\ \frac{DT}{Dt} &= -\frac{T_0 N^2}{g} w + S_T && (5.3) \\ \frac{\partial p}{\partial z} &= \frac{gT}{T_0} && (5.4) \end{aligned}$$

where

$$\frac{D}{Dt} = \frac{\partial}{\partial t} + \mathbf{U} \cdot \nabla + w \frac{\partial}{\partial z} \quad (5.5)$$

is the advective derivative, and (x, y, z) are the eastward, northward, and upward (above sea level) distances, t is time, $U = (u, v)$ is the zonal (eastward) and meridional (northward) velocities, w is the vertical velocity, and T is the perturbation temperature. The full temperature in this system (including the background state) is $T_0 + \frac{\partial \bar{T}}{\partial z} z + T$. The vertical gradient of the temperature determines its dry stability to vertical perturbations, and its buoyancy frequency. The buoyancy frequency of the background state is $N = \left(\frac{g}{T_0} (\frac{\partial \bar{T}}{\partial z} + \frac{g}{c_p}) \right)^{\frac{1}{2}}$, assumed here to be constant, as is the mean basic state temperature, T_0.

The pressure, p, is always a reduced pressure divided by a constant density factor which is omitted; thus the units for this reduced pressure are given by

$$[p] = \frac{L^2}{T^2} \tag{5.6}$$

where $[f]$ = units of f. We utilize the following standard values for parameters: $T_0 = 300\ K$, the mean atmospheric temperature in Kelvin; $N = 10^{-2}\ s^{-1}$, the buoyancy frequency; $g = 9.8\ m/s^2$, gravitational acceleration; $c = 50\ m/s$, the wave speed; $H_T = 15.75\ km$, the tropopause height, obtained from the relation $H_T = \frac{c\pi}{N}$; and $\beta = 2.28 \times 10^{-11}\ m^{-1}s^{-1}$.

We now nondimensionalize these equations, using the following units: $L_E = \sqrt{\frac{c}{\beta}} \approx 1500\ km$, the typical equatorial length scale; $T_E = \frac{L_E}{c} \approx 8.3\ hrs$, the equatorial timescale; $\bar{\alpha} = \frac{H_T N^2 T_0}{\pi g} \approx 15\ K$, the typical temperature scale; and $P = c^2$, the pressure scale. Further derived units include the vertical velocity scale $W = \frac{H_T}{\pi T_E} \approx .18\ m/s$.

Using the above units and parameters, we have the nondimensional hydrostatic

Boussinesq equations on a β-plane:

$$\frac{D\hat{\mathbf{U}}}{D\hat{t}} = -\hat{y}\hat{\mathbf{U}}^{\perp} - \hat{\nabla}\hat{p} + \hat{S}_{\mathbf{U}} \tag{5.7}$$

$$\hat{\nabla}\cdot\hat{\mathbf{U}} + \frac{\partial\hat{w}}{\partial\hat{z}} = 0 \tag{5.8}$$

$$\frac{D\hat{T}}{D\hat{t}} = -\hat{w} + \hat{S}_T \tag{5.9}$$

$$\frac{\partial\hat{p}}{\partial\hat{z}} = \hat{T} \tag{5.10}$$

where the hats represent nondimensional variables scaled by the units described above. From this point on, we drop the hats and consider all variables to be nondimensional quantities. The boundary conditions assumed here are no normal flow at the top and bottom of the troposphere, i.e., $w = 0$ at $z = 0, \pi$.

5.2.2 Vertical Decomposition and Galerkin Expansion

The flow in the tropics is primarily in the first baroclinic mode, that is, with winds in the lower troposphere of opposite sign and equal magnitude to those in the upper troposphere. First baroclinic mode models have been used in many studies of tropical atmospheric dynamics dating back to Matsuno (1966) and Gill (1980). In these models, there is one temperature, representing a typical midtropospheric temperature, and the first baroclinic mode velocity. We derive this model more rigorously from the hydrostatic Boussinesq equations by performing a Galerkin truncation, keeping two velocity modes. We retain the barotropic mode as well as the baroclinic mode, unlike the above studies. Keeping the barotropic mode is necessary for the study of tropical-extratropical interactions, where transport of momentum from the barotropic and baroclinic mode is an important effect (Majda and Biello, 2003).

We begin by performing a vertical decomposition of the variables as such:

$$\mathbf{U} = \bar{\mathbf{U}} + \mathbf{U}' \tag{5.11}$$

$$p = \bar{p} + p' \tag{5.12}$$

and so on, where $\bar{\mathbf{U}} = \langle \mathbf{U}, 1 \rangle$, $\bar{p} = \langle p, 1 \rangle$ are the depth-independent barotropic modes (i.e., the orthogonal projection on 1), and $\langle f, g \rangle = \frac{1}{\pi}\int_0^\pi fgdz$. The quantities $\mathbf{U}', p'$ are baroclinic modes, with $\langle \mathbf{U}', 1 \rangle = \langle p', 1 \rangle = 0$.

The complete Galerkin expansion of baroclinic modes in nondimensional form is

$$p' = \Sigma_{j=1}^{\infty} p_j e_j(z) \tag{5.13}$$

$$\mathbf{U}' = \Sigma_{j=1}^{\infty} \mathbf{U}_j e_j(z) \tag{5.14}$$

$$e_j(z) = \sqrt{2}cos(zj), 0 < z < \pi, j = 1, 2, ... \tag{5.15}$$

(see Chapter 9 of Majda (2003)).

The projected free tropospheric nonlinear dynamics, obtained by substituting (5.11) and (5.12) into equations (5.7)-(5.10), are as follows: first, the barotropic mode dynamics,

$$\frac{\bar{D}\bar{\mathbf{U}}}{Dt} + \langle \mathbf{U}' \cdot \nabla \mathbf{U}', 1 \rangle + \langle w' \frac{\partial \mathbf{U}'}{\partial z}, 1 \rangle + y\bar{\mathbf{U}}^{\perp} = -\nabla \bar{p} + \bar{S}_{\mathbf{U}} \tag{5.16}$$

$$\nabla \cdot \bar{\mathbf{U}} = 0 \tag{5.17}$$

where

$$\frac{\bar{D}}{Dt} = \frac{\partial}{\partial t} + \bar{\mathbf{U}} \cdot \nabla. \tag{5.18}$$

The vertical mean vertical velocity satisfies $\bar{w} = 0$. The baroclinic dynamics satisfy

$$\begin{aligned} \frac{\bar{D}\mathbf{U}'}{Dt} + \mathbf{U}' \cdot \nabla \bar{\mathbf{U}} + \mathbf{U}' \cdot \nabla \mathbf{U}' - \langle \mathbf{U}' \cdot \nabla \mathbf{U}', 1 \rangle & \\ + w' \frac{\partial \mathbf{U}'}{\partial z} - \langle w' \frac{\partial \mathbf{U}'}{\partial z}, 1 \rangle + y \mathbf{U}'^{\perp} &= -\nabla p' + S'_{\mathbf{U}} \qquad (5.19) \\ \frac{\bar{D}}{Dt}\left(\frac{\partial p'}{\partial z}\right) + \mathbf{U}' \cdot \nabla \left(\frac{\partial p'}{\partial z}\right) + w' \frac{\partial}{\partial z}\left(\frac{\partial p'}{\partial z}\right) &= -w' + S_T. \qquad (5.20) \end{aligned}$$

In equation (5.20), we have used the relation $T = \frac{\partial p'}{\partial z}$ obtained from the hydrostatic equation; therefore equation (5.20) is the full buoyancy equation, not the barotropic or baroclinic parts as the velocity equations (5.16) and (5.19).

We create a simplified model for the dynamics of the free troposphere via Galerkin truncation of the baroclinic mode equations to the first baroclinic mode, as motivated above. It is important to point out that the first baroclinic approximation is strongly justified in areas of deep convection, where latent heating in the midtroposphere creates the baroclinic structure. However, in dry regions, this approximation begins to break down, due to vertical propagation of gravity waves which upset the vertical structure. Therefore some degree of care must be taken when interpreting results which rely strongly on behavior in dry regions.

Our assumptions about the baroclinic modes are as follows (all valid for $0 \leq z \leq \pi$):

$$\begin{aligned} p' &= p_1 \sqrt{2} cos(z) && (5.21) \\ \mathbf{U}' &= \mathbf{U}_1 \sqrt{2} cos(z) && (5.22) \\ T &= p'_z = -p_1 \sqrt{2} sin(z) && (5.23) \\ w' &= -\nabla \cdot \mathbf{U_1} \sqrt{2} sin(z). && (5.24) \end{aligned}$$

First, this implies that the baroclinic interaction terms in the barotropic velocity equation (5.16) project directly; i.e., this equation becomes

$$\frac{\bar{D}\bar{\mathbf{U}}}{Dt} + \mathbf{U_1} \cdot \nabla \mathbf{U_1} + (\nabla \cdot \mathbf{U_1})\mathbf{U_1} + y\bar{\mathbf{U}}^{\perp} = -\nabla \bar{p} + \bar{S}_{\mathbf{U}}. \tag{5.25}$$

To derive the reduced dynamics for the baroclinic velocity field $\mathbf{U_1}$, we take the inner product of equation (5.19) above with $\sqrt{2}cos(z)$ under the ansatz above, giving the Galerkin projected baroclinic momentum equation

$$\frac{\bar{D}\mathbf{U_1}}{Dt} + \mathbf{U_1} \cdot \nabla \bar{\mathbf{U}} + y\mathbf{U_1}^{\perp} = -\nabla p_1 + S'_{\mathbf{U}}. \tag{5.26}$$

To derive the projected baroclinic buoyancy equation, we take the inner product of equation (5.20) above with $\sqrt{2}sin(z)$ and this yields the Galerkin truncated buoyancy equation,

$$\frac{\bar{D}p_1}{Dt} + \nabla \cdot \mathbf{U_1} = -S_T. \tag{5.27}$$

Through a mild abuse of notation, we still denote $S_T = \langle S_T, sin(z) \rangle$. This equation is often written in terms of T, with the identification from (5.23),

$$T = -p_1. \tag{5.28}$$

(Since this is the only temperature in the system, we denote the above by T rather than T_1 to be consistent with standard notation.) Maxima of T imply minima in pressure in the lower troposphere and maxima in the upper troposphere.

5.2.3 Physical Parameterizations

We now must consider the source terms $S_{\mathbf{U}}$ and S_T. The effects we want to capture are momentum damping by frictional drag, and three temperature source terms: the radiative cooling $S_{T,R}$, the sensible heat flux $S_{T,SH}$, and the precipitation $S_{T,P}$.

Momentum Damping, Radiative Cooling, and Sensible Heat Flux

We parameterize frictional dissipation in the atmosphere by relaxation of velocities to zero:

$$S_{\mathbf{U}} = -\bar{d}\mathbf{U}. \tag{5.29}$$

For surface velocities, one would expect relatively strong damping (for instance on the order of 5 day damping time), but for the upper troposphere, there is very little momentum drag. The momentum drag parameter $\bar{d}$ is therefore somewhat arbitrary for first baroclinic mode models. Studies such as Gill (1980) and Held and Kang (1987) have used values around $\bar{d} = (3.8 - 10\ days)^{-1}$. With this model we utilize values similar to these, or consider the inviscid problem with $\bar{d} = 0$.

The standard parameterization for radiation in models of this complexity is Newtonian cooling, i.e., relaxation to a specified radiative equilibrium profile over a certain damping time. That is,

$$S_{T,R} = -d_T(T - T_{eq}) \tag{5.30}$$

where $d_T \approx (20\ days)^{-1}$. Since radiation acts as a net cooling within the atmosphere, we specify $T_{eq} < 0$.

We parameterize the sensible heat flux in a manner similar to the momentum damping, using a drag law formulation that relaxes temperatures to the surface value:

$$S_{T,SH} = d_{SH}(T_s - T) \tag{5.31}$$

where T_s is the sea surface temperature. The drag coefficient is typically selected to be $d_{SH} \approx (10\ days)^{-1}$.

Sensible heat fluxes in the tropical atmosphere are small compared to evaporative fluxes, radiative cooling, and precipitation. The ratio of evaporation to sensible heating is given by the Bowen ratio, which is typically on the order of .2 in the tropics

(Hartmann, 1994). We therefore often neglect sensible heating for simplicity in this model.

Precipitation

The final diabatic term needed in the buoyancy equation is the precipitation, $S_{T,P}$. The parameterization of precipitation has been somewhat difficult historically in models of this complexity. Many studies (e.g., Gill (1982), Philander et al. (1984)) have simply specified precipitation distributions, or constructed simple parameterizations based on sea surface temperature distributions, and then calculated the atmospheric response to this heating. However as described in Chapter 1, moisture not only drives the large scale flow, it is advected by the large scale flow as well. Therefore, for our parameterization of precipitation, we employ an active moisture equation so we can allow the flow to affect the precipitation distribution, and vice-versa. Other studies which use active moisture budgets to determine the precipitation within first baroclinic mode models include Neelin and Held (1987), Neelin et al. (1987), Neelin and Zeng (2000), and Bretherton and Sobel (2002).

In the tropics, most of the moisture is concentrated in the lower troposphere. For our simplified dynamics, we will derive an equation for q_v, the mixing ratio of water vapor in the atmosphere, which is vertically averaged as in Neelin and Zeng (2000). The motivation for the closure approach is best understood by looking at the equations for bulk cloud microphysics which illustrate the full moisture dynamics. Ultimately we will get a simplified equation for $q(x, y, t) = \langle q_v, 1\rangle$.

Bulk Cloud Microphysics

To examine the conservation laws present in the microphysical system, we consider the set of equations without radiative effects or sensible heat fluxes. We derive conservation laws for the moist static energy, an energy which accounts for the moisture content of the air (which releases latent heat when it condenses), and the total moisture content of the air. The fully dimensional bulk microphysical equations are the following:

$$
\begin{aligned}
c_p \frac{DT}{Dt} &= -\frac{c_p T_0 N^2}{g} w + L(C_d - E_r) && (5.32)\\
\frac{Dq_v}{Dt} &= -C_d + E_r && (5.33)\\
\frac{Dq_c}{Dt} &= C_d - A_r - C_r && (5.34)\\
\frac{Dq_r}{Dt} &= \frac{\partial(v_t q_r)}{\partial z} + A_r + C_r - E_r && (5.35)
\end{aligned}
$$

where q_v is the mixing ratio (mass of constituent divided by mass of dry air) of water vapor, q_c is the mixing ratio of cloud water, and q_r is the mixing ratio of rain. Of the various conversion terms, C_d is the condensation of water vapor, E_r is the reevaporation of rain into unsaturated air, A_r is the autoconversion of cloud water into rain, and C_r is the rain collection (falling rain gathering cloud water into rain). v_t is the terminal (downward) velocity of rain droplets. Cloud resolving numerical models and some general circulation models have parameterizations of each of these processes, and often utilize distributions of droplet size, of which the conversion processes and fall speed are a function. See Emanuel (1994) for further discussion of these parameterizations.

An important relation for the parameterization of the condensation and evaporation is the Clausius-Clapeyron equation, a first order differential equation for the saturation vapor pressure e_s as a function of temperature. The Clausius-Clapeyron equation is:

$$\frac{de_s}{dT} = \frac{Le_s}{R_v T^2} \tag{5.36}$$

and the saturation specific humidity satisfies $q_{v,s} = \frac{R_d e_s}{R_v p}$, where R_d and R_v are the gas constants for dry air and water vapor, respectively, and p is the pressure. Condensation occurs when the specific humidity exceeds its saturation value, i.e., when

$q_v > q_{v,s}$. Specifically,

$$q_v < q_{v,s}, q_c = 0, C_d = 0 \tag{5.37}$$

$$q_v > q_{v,s}, q_c \geq 0, C_d = \infty. \tag{5.38}$$

The latter implies that $q_c \geq 0 \Leftrightarrow q_v = q_{v,s}$. Majda and Souganidis (2000) discuss various subtle issues for these parameterizations in the context of turbulent mixing problems.

Conservation Principles for Bulk Cloud Microphysics

There are two key quantities in this microphysics model with conservation laws. Firstly, the moist static energy, $m = c_p T + \frac{c_p T_0 N^2}{g} z + L q_v$ is conserved, as can be seen from adding (5.32) and (5.33) and using $w = \frac{Dz}{Dt}$:

$$\frac{Dm}{Dt} = 0. \tag{5.39}$$

The moist static energy, which can be rewritten in the familiar form $m = c_p(T + \frac{\partial \bar{T}}{\partial z} z) + gz + Lq_v$, includes the thermal energy, the gravitational energy, and a moisture component reflecting the thermal energy increase that would occur if condensation occurs.

Further, by adding equations (5.33), (5.34), (5.35), we see that the total moisture $Q = q_v + q_c + q_r$ is conserved except for precipitation:

$$\frac{DQ}{Dt} = \frac{\partial (v_t q_r)}{\partial z} \tag{5.40}$$

where the right hand side is the divergence of the rain water flux, falling at its terminal velocity. The precipitation is defined as the flux of this term evaluated at the ground, i.e., $P = v_t q_r|_{z=0}$. Clearly P satisfies the constraint $P \geq 0$. The equations in (5.34) and (5.35) imply that the total liquid water $q_l = q_c + q_r$ satisfies

$$\frac{Dq_l}{Dt} = C_d - E_R + \frac{\partial v_t q_r}{\partial z}. \tag{5.41}$$

Keeping these conservation laws for the full system in mind, we now proceed with vertical averaging of the equations, and make several approximations appropriate to the level of complexity of the model. Our goal will be one equation for the vertically integrated water vapor, and parameterizations for the latent heating and evaporation.

Vertical Averaging of the Moisture Equation

After vertical averaging of the equations in (5.39) and (5.40) (i.e., taking the inner product of these quantities with 1), we have the following conservation equations, for liquid water

$$\langle \frac{Dq_l}{Dt}, 1 \rangle = \langle C_d - E_r, 1 \rangle - P \tag{5.42}$$

and moist static energy

$$\langle \frac{Dm}{Dt}, 1 \rangle = 0 \tag{5.43}$$

while the conservation of vertically integrated water vapor (equation (5.33)) becomes

$$\langle \frac{Dq_v}{Dt}, 1 \rangle = -\langle C_d - E_r, 1 \rangle. \tag{5.44}$$

We now discuss additional approximations to these vertically averaged moisture equations.

Moisture Equation Approximation 1

We first assume a quasi-steady state from faster dynamics for vertically integrated liquid water q_l, i.e., That is,

$$\langle \frac{Dq_l}{Dt}, 1 \rangle = 0. \tag{5.45}$$

This is justified by the faster microphysical timescales which determine the rate of change of liquid water, and amounts to the same simplification used in our GCM of Chapter 2, that condensate is ignored.

Using approximation (5.45) in equation (5.42), we have

$$P = \langle C_d - E_r, 1 \rangle. \tag{5.46}$$

Substituting the above into equation (5.44) then implies that

$$\langle \frac{Dq_v}{Dt}, 1 \rangle = -P. \tag{5.47}$$

This approximation has allowed us to eliminate the liquid water variables as prognostic variables, and consider the water vapor variable alone.

Next, we make approximations regarding the vertical structure of water vapor to simplify our budgets further. We first separate the water vapor into vertical average and mean zero components as above:

$$q_v = \bar{q}_v + q_v'. \tag{5.48}$$

Rearranging the terms in the advective derivative, the equation for the mean tendency of water vapor is therefore:

$$\begin{aligned} \langle \frac{Dq_v}{Dt}, 1 \rangle = \frac{\bar{D}\bar{q}_v}{Dt} \quad &+ \quad \langle \mathbf{U}' \cdot \nabla q_v', 1 \rangle \\ &+ \quad \langle w' \frac{\partial q_v'}{\partial z}, 1 \rangle - (w' q_v')|_{z=0} = -P. \end{aligned} \tag{5.49}$$

The surface turbulent flux term $(w'q_v')|_{z=0}$ is the evaporation flux E, i.e.,

$$(w'q_v')|_{z=0} = E. \tag{5.50}$$

Moisture Equation Approximation 2

We assume that there is a background mean moisture gradient (as for the temperature in the Boussinesq equations) that is obtained from a mean sounding. We assume that this background moisture gradient is the dominant contribution to the vertical motion. That is,

$$\langle w' \frac{\partial q_v'}{\partial z}, 1 \rangle = \bar{Q} \nabla \cdot \mathbf{U_1}. \tag{5.51}$$

The key approximation is that the "gross moisture stratification" $\bar{Q}$ is independent of the integrated moisture content.

Note that $\bar{Q}$ satisfies $\bar{Q} > 0$ since typical moisture soundings fall off approximately exponentially with scale heights of a few kilometers. The parameter $\bar{Q}$ is quite important for the dynamics; it reduces the stability in moist regions, as described in the introduction. We will return to this parameter later in this chapter.

Moisture Equation Approximation 3

For simplicity, we ignore turbulent fluctuations and assume

$$\langle \mathbf{U}' \cdot \nabla q_v', 1 \rangle = 0. \tag{5.52}$$

that is, perturbation moisture is only advected by the mean flow. This approximation could be refined if needed for other modeling studies.

Simplified Dynamics for Moisture Equation

Using equations (5.50), (5.51), and (5.52) in equation (5.49), we have, with $q \equiv \langle q_v, 1 \rangle$, the simplified dynamics for moisture:

$$\frac{\bar{D}q}{Dt} + \bar{Q} \nabla \cdot \mathbf{U_1} = E - P \tag{5.53}$$

where $\bar{Q}$ is the prescribed gross moisture stratification. We now discuss the evaporation and precipitation parameterizations.

Evaporation Parameterization

The evaporation is parameterized by a drag law formulation, that is,

$$E = d_q(q_s(T_s) - q). \tag{5.54}$$

A typical value of the inverse evaporative timescale is $d_q \approx (10days)^{-1}$. The temperature T_s used to calculate the saturation mixing ratio at the surface is the sea surface temperature, which we specify as a function of x and y in this model.

Precipitation Parameterization

Our spatial units for the dynamics is 1500 km, so the tacit assumption operating is that we are considering effects of moisture on large spatial scales. On such large scales, it is natural to model the precipitation based on the formulation of Betts and Miller (Betts (1986); Betts and Miller (1986)) who relax temperature and humidity back to a reference profile when some convective criterion is met. To implement a Betts-Miller scheme within a full GCM is complicated, and requires a correction to satisfy enthalpy conservation, and a treatment of shallow convection (we discuss this in detail in Chapter 7). Within the simple model, there is a simple form of the Betts-Miller scheme: when there is enough moisture for convection, we relax the humidity back to a significant fraction of the saturation value, $\tilde{q}$. More precisely,

$$P = \frac{1}{\tau_c}(q - \tilde{q}(T))^+ \tag{5.55}$$

where $\tilde{q}$ is a prescribed function of the atmospheric temperature (possibly a nonlinear function), and τ_c is a convective adjustment time. Neelin and Zeng (2000) and Betts and Miller (1986) use relaxation times of the order $\tau_c \approx 2hrs$, whereas Bretherton et al. (2004) estimate $\tau_c \approx 12hrs$ from current observations.

Two types of functions are typically used for the moisture saturation parameterization. The first of these is a precipitation threshold, independent of T, i.e.,

$$\tilde{q}(T) = \hat{q}. \tag{5.56}$$

This parameterization is the simplest mathematically, and is physically justified since atmospheric temperatures are approximately uniform across the tropics. There is also observational data which correlates the precipitation in the tropics with the humidity content (Sobel et al., 2004).

A second parameterization, utilized by Neelin and Zeng (2000), is proportional to temperature:

$$\tilde{q}(T) = T. \tag{5.57}$$

We call this the CAPE parameterization, since it is based on the quasi-equilibrium of convectively available potential energy (CAPE), which is the integrated buoyancy a surface parcel of air can obtain (Emanuel, 1994). CAPE increases with the surface humidity since more latent heat is released for parcels that are more humid, which are therefore more buoyant relative to the environment. CAPE also decreases with the temperature of the environment, since it is easier to be buoyant in colder air. The proper expression for CAPE in the nondimensional units explained above for our system is $q - T$, so CAPE is kept in quasi-equilibrium by using the saturation criterion (5.57). Full general circulation model convection schemes such as Arakawa-Schubert (Arakawa and Schubert, 1974) and Betts and Miller (1986) would reduce to this in the first baroclinic mode system. Thus, the parameterizations in (5.56) or (5.57) together with (5.55) are simple prototype models for the behavior of GCM's.

In this chapter, we build a class of convective parameterizations which contain both of these options by performing our analysis on the parameterization

$$\tilde{q}(T) = \hat{q} + \alpha T \tag{5.58}$$

with $0 \leq \alpha \leq 1$ and $\hat{q} > 0$. Actually, all the analysis developed below only requires $-\bar{Q} < \alpha < +\infty$. The use of various parameterizations for precipitation permits us to study the variability of dynamics with different convective parameterizations, an important practical topic.

For the arguments in Section 5.3 where we differentiate the equations, it is convenient to keep in mind a smooth regularized version of (5.55), where

$$P = \frac{1}{\tau_c}\phi(q - \tilde{q}(T)) \tag{5.59}$$

with $\phi(s)$ a monotone smooth approximation to $(s)^+$ and satisfying

$$\begin{aligned} \phi(s) &\geq 0 \\ \phi(s) &\equiv 1 \text{ for } s > 0 \\ \phi(s) &\equiv 0 \text{ for } s < 0 \\ \phi'(s) &\geq 0. \end{aligned} \tag{5.60}$$

Since $\hat{q} \geq 0$, with (5.60) we also automatically have

$$(s + \hat{q})\phi(s) \geq 0. \tag{5.61}$$

which is obviously satisfied for (5.55). In the zero relaxation limit, one can recover (5.55) through letting $\phi(s)$ depend on τ_c and converge to $(s)^+$ as $\tau_c \to 0$ in standard fashion. Without further comment, we assume that P is smooth with the above structure when we differentiate the equations in Section 5.3 below.

Nondimensional Moisture Equation

We nondimensionalize moisture by the scale of temperature variations divided by the latent heat coefficient L: $Q = \frac{\bar{\alpha}}{L}$, where $\bar{\alpha} = \frac{H_T N^2 T_0}{\pi g}$ is the temperature scale from Section 5.2.1.

Our final nondimensional moisture equation is then the following:

$$\frac{\bar{D}q}{Dt} + \bar{Q}\nabla \cdot \mathbf{U_1} = d_q(q_s(T_s) - q) - P. \tag{5.62}$$

All of the parameters, $\bar{Q}$, $\hat{q}$, etc. have now taken nondimensional values.

This equation and the precipitation parameterization are used in the temperature equation with the following approximation:

Vertical Heating: Approximation 4

Consistent with the above approximations we assume that all vertical heating (convective, radiative, and sensible) goes into the first baroclinic mode, so that the fully dimensional temperature equation becomes:

$$\begin{aligned} \frac{DT}{Dt} + w = LP\sqrt{2}sin(\frac{z}{H}) \quad &- \quad d_T(T - T_{eq})\sqrt{2}sin(\frac{z}{H}) \\ &+ \quad d_{SH}(T_s - T)\sqrt{2}sin(\frac{z}{H}). \end{aligned} \tag{5.63}$$

Note that equations (5.23), (5.24), (5.27), and (5.28) together with (5.63) yields the equation for the temperature T listed in (5.67) below with (5.62) yielding the moisture equation. The momentum equations for $\bar{\mathbf{U}}$ and $\mathbf{U_1}$ have been derived in (5.25) and (5.26) with the parameterizations discussed above. This completes the dynamics in the simplified model.

5.3 Conservation Laws and Dry and Moist Phase Speeds

We begin by summarizing the final simplified equations that we have derived in the last section:

$$\begin{aligned}
\frac{\bar{D}\bar{\mathbf{U}}}{Dt} + \nabla \cdot (\mathbf{U_1} \otimes \mathbf{U_1}) + y\bar{\mathbf{U}}^{\perp} &= -\nabla \bar{p} - \bar{d}\bar{\mathbf{U}} && (5.64)\\
\nabla \cdot \bar{\mathbf{U}} &= 0 && (5.65)\\
\frac{\bar{D}\mathbf{U_1}}{Dt} + \mathbf{U_1} \cdot \nabla \bar{\mathbf{U}} + y\mathbf{U_1}^{\perp} &= \nabla T - \bar{d}\mathbf{U_1} && (5.66)\\
\frac{\bar{D}T}{Dt} - \nabla \cdot \mathbf{U_1} &= -d_T(T - T_{eq}) + d_{SH}(T_s - T) + P && (5.67)\\
\frac{\bar{D}q}{Dt} + \bar{Q}\nabla \cdot \mathbf{U_1} &= d_q(q_s(T_s) - q) - P. && (5.68)
\end{aligned}$$

The form of the precipitation parameterization, P, is discussed in (5.55)-(5.61) above.

We now present several basic conservation principles for the simplified dynamics equations. For simplicity, set $\bar{d} = d_T = d_q = d_{SH} = 0$. Generalizing to the cases with the source terms is trivial, and simply adds source terms to the conservation laws. First, there is a principle of conservation of moist static energy $m = q + T$. This is given by

$$\frac{\bar{D}m}{Dt} - (1 - \bar{Q})\nabla \cdot \mathbf{U_1} = 0. \tag{5.69}$$

There is a physical justification for this equation which involves the assumed vertical gradients of humidity and buoyancy. In the nondimensional Boussinesq equations, we have assumed a mean vertical gradient for T of slope 1. Further, there is a mean gradient of q of slope $-\bar{Q}$, as explained in Section 5.2.3 above. The vertical motion is $w = -\nabla \cdot \mathbf{U_1}$ in our single mode approximation. The second term in (5.69) can therefore be understood as the vertical advection of the mean moist static energy gradient.

Another conservation principle can be obtained by eliminating the divergence terms between (5.67) and (5.68). This can be obtained by considering the quantity $q + \bar{Q}T$ which satisfies

$$\frac{\bar{D}(q + \bar{Q}T)}{Dt} = -(1 - \bar{Q})P. \tag{5.70}$$

Since the precipitation P is non-negative, we have

$$\frac{\bar{D}(q + \bar{Q}T)}{Dt} \leq 0 \tag{5.71}$$

provided $0 < \bar{Q} < 1$. We will confirm later that $\bar{Q}$ must indeed be within these bounds for well-posedness.

5.3.1 Dissipation of Total Energy

We now form an energy principle using this system of equations and show that this quadratic quantity is dissipated.

The total dry energy density is given by the following:

$$\epsilon_d = \frac{1}{2}(|\bar{\mathbf{U}}|^2 + |\mathbf{U_1}|^2 + T^2) \tag{5.72}$$

with the energy principle

$$\frac{\bar{D}\epsilon_d}{Dt} = -\nabla \cdot (\bar{\mathbf{U}} \cdot (\mathbf{U_1} \otimes \mathbf{U_1})) - \nabla \cdot \bar{\mathbf{U}}\bar{p} + \nabla \cdot \mathbf{U_1}\mathbf{T} + TP. \tag{5.73}$$

In this form, precipitation does work on or against the fluid depending on the sign of the temperature. We anticipate that precipitation will be a dissipative mechanism on the overall energy budget including moisture. We observe from equation (5.70) above that

$$\frac{\bar{D}}{Dt}\left(\frac{1}{2}\frac{(q + \bar{Q}T)^2}{(1 - \bar{Q})(\alpha + \bar{Q})}\right) = -(\frac{\bar{Q}T + q}{\alpha + \bar{Q}})P. \tag{5.74}$$

Thus, we introduce a moist energy density contribution:

$$\epsilon_m = \frac{1}{2}\frac{(q+\bar{Q}T)^2}{(1-\bar{Q})(\alpha+\bar{Q})}. \tag{5.75}$$

Note that $\epsilon_m \geq 0$ provided $0 < \bar{Q} < 1$. Further, the addition of equation (5.73) to (5.74) will cancel the indefinite flux term and replace it by the term $-\frac{q-\alpha T}{\alpha+\bar{Q}}P$. According to the structure of the precipitation assumed in (5.55)-(5.61), $(q-\alpha T)P \geq 0$ so that this additional source term is always negative.

Thus consider the total energy density $\epsilon = \epsilon_d + \epsilon_m$. We have the local energy principle

$$\frac{\bar{D}\epsilon}{Dt} = -\nabla\cdot(\bar{\mathbf{U}}\cdot(\mathbf{U_1}\otimes\mathbf{U_1})) - \nabla\cdot(\bar{\mathbf{U}}\bar{p}) + \nabla\cdot(\mathbf{U_1}T) - \frac{q-\alpha T}{\alpha+\bar{Q}}P \tag{5.76}$$

and by integrating, we obtain the Energy Dissipation Identity

$$\int \epsilon(t)dxdy = \int \epsilon(0)dxdy - \int_0^t \int \frac{q-\alpha T}{\alpha+\bar{Q}}Pdxdydt. \tag{5.77}$$

In particular, there is decay of the total energy in the absence of forcing due to the weak dissipative effects of moisture at large scales independent of the relaxation time τ_c:

$$\int \epsilon(t)dxdy \leq \int \epsilon(0)dxdy. \tag{5.78}$$

5.3.2 Derivative Formulation

We can derive additional important results by considering the system formed by taking the gradient of the equations (5.64)-(5.68) above, without the barotropic mode. As mentioned earlier in Section 5.2.3, the approximation without the barotropic mode is often used in the simplest tropical climate model and is trivially always satisfied in one horizontal space dimension. We call this the derivative formulation, and we will derive a conservation law for this, and use it to demonstrate mean square boundedness of the first derivative within this system. One must neglect the barotropic mode ($\bar{\mathbf{U}}$) in order to derive this since the barotropic-baroclinic nonlinear transfer term makes the derivation below invalid.

Setting the barotropic velocity equal to zero in equations (5.64)-(5.68) without the forcing gives

$$\frac{\partial u_1}{\partial t} = yv_1 + \frac{\partial T}{\partial x} \tag{5.79}$$
$$\frac{\partial v_1}{\partial t} = -yu_1 + \frac{\partial T}{\partial y} \tag{5.80}$$
$$\frac{\partial T}{\partial t} = (\nabla \cdot \mathbf{U_1}) + P \tag{5.81}$$
$$\frac{\partial q}{\partial t} = -\bar{Q}(\nabla \cdot \mathbf{U_1}) - P. \tag{5.82}$$

The gradient system is then the following:

$$\frac{\partial \nabla u_1}{\partial t} = y\nabla v_1 + v_1\hat{\mathbf{e}}_\mathbf{2} + \frac{\partial \nabla T}{\partial x} \tag{5.83}$$
$$\frac{\partial \nabla v_1}{\partial t} = -y\nabla u_1 - u_1\hat{\mathbf{e}}_\mathbf{2} + \frac{\partial \nabla T}{\partial y} \tag{5.84}$$
$$\frac{\partial \nabla T}{\partial t} = \nabla(\nabla \cdot \mathbf{U_1}) + \nabla P \tag{5.85}$$
$$\frac{\partial \nabla q}{\partial t} = -\bar{Q}\nabla(\nabla \cdot \mathbf{U_1}) - \nabla P. \tag{5.86}$$

The dry energy flux equation for this system, analogous to equation (5.73), is given by

$$\frac{\partial \epsilon_{x,d}}{\partial t} = \frac{\partial}{\partial x}(\nabla u_1 \cdot \nabla T) + \frac{\partial}{\partial y}(\nabla v_1 \cdot \nabla T) + v_1\frac{\partial u_1}{\partial y} - u_1\frac{\partial v_1}{\partial y} + \nabla P \cdot \nabla T \tag{5.87}$$

where

$$\epsilon_{grad,d} = \frac{1}{2}(|\nabla \mathbf{U_1}|^2 + |\nabla T|^2). \tag{5.88}$$

We have a similar moist energy contribution as in the previous system (see equation (5.75)):

$$\epsilon_{grad,m} = \frac{1}{2}\frac{(\nabla q + \bar{Q}\nabla T)^2}{(1-\bar{Q})(\alpha+\bar{Q})} \tag{5.89}$$

such that setting the total energy to

$$\epsilon_{grad} = \epsilon_{grad,d} + \epsilon_{grad,m} = \frac{1}{2}\left(|\nabla \mathbf{U_1}|^2 + |\nabla T|^2 + \frac{(\nabla q + \bar{Q}\nabla T)^2}{(1-\bar{Q})(\alpha+\bar{Q})}\right) \tag{5.90}$$

gives the energy principle:

$$\begin{aligned}\frac{\partial \epsilon_{grad}}{\partial t} = \frac{\partial}{\partial x}(\nabla u_1 \cdot \nabla T) \quad &+ \quad \frac{\partial}{\partial y}(\nabla v_1 \cdot \nabla T) \\ &+ \quad v_1\frac{\partial u_1}{\partial y} - u_1\frac{\partial v_1}{\partial y} - \nabla P \cdot (\nabla(q-\alpha T)).\end{aligned} \tag{5.91}$$

Using the chain rule, the last term can be rewritten as

$$-\nabla P \cdot (\nabla(q-\alpha T)) = -P'|\nabla(q-\alpha T)|^2. \tag{5.92}$$

Now, it follows from (5.55) in the weak sense, or equivalently, (5.59), that P' satisfies $P' \geq 0$ so this term is negative semi-definite pointwise.

We can integrate this equation in (5.92) to obtain the energy principle

$$\begin{aligned}\int \epsilon_{grad}(t)dxdy \quad &= \quad \int \epsilon_{grad}(0)dxdy + \int_0^t \int (v_1\frac{\partial u_1}{\partial y} - u_1\frac{\partial v_1}{\partial y})dxdydt \\ &- \quad \int_0^t \int \frac{|\nabla(q-\alpha T)|^2}{\alpha+\bar{Q}}P'dxdydt \\ &\leq \quad \int \epsilon_{grad}(0)dxdy + \int_0^t \int (v_1\frac{\partial u_1}{\partial y} - u_1\frac{\partial v_1}{\partial y})dxdydt.\end{aligned} \tag{5.93}$$

The so-called "β-effect" terms $v_1\frac{\partial u_1}{\partial y} - u_1\frac{\partial v_1}{\partial y}$ can cause exponential growth. However, there is always dissipation of energy in this derivative system by precipitation, independent of the convective relaxation time τ_c, and independent of convective parameterization.

The estimate in (5.93) guarantees that for any finite time interval, the quantities $\nabla\mathbf{U_1}$, ∇T, and ∇q are bounded in L^2 for bounded initial conditions independent of relaxation time. By Sobolev's Lemma, this means that smooth initial conditions cannot develop discontinuities in $\mathbf{U_1}, T, q$ in a single space dimension.

Remark: Since the second derivative of precipitation with respect to the saturation deficit P'' is no longer sign definite, there are no higher order energy principles. Therefore, it is natural to expect that discontinuities in the gradients of velocity, temperature, and humidity, and discontinuities in precipitation, can develop in time from appropriate smooth initial conditions in the limit of $\tau_c \to 0$.

5.4 Conclusions

We have derived a simplified set of equations that are suitable for study of the location and strength of precipitation regions in the tropical atmosphere and the effect of moisture on large-scale tropical dynamics in general. We give a full derivation of the equations starting from the hydrostatic Boussinesq equations on an equatorial $\beta-$plane. We present this derivation for completeness and for readers who come from an applied mathematics background, but the derivation is additionally useful for several reasons. First the derivation shows the assumptions of the model clearly, and is useful for connecting to models with full vertical structure (for instance, by suggesting appropriate diagnostics to understand tropical circulations within the moist GCM of Chapter 2). The Galerkin truncation additionally gives a systematic procedure for expansion into a system with a higher number of modes. Finally our treatment of moisture ensures that conservation laws from models that treat water in a more complete manner are retained.

It is important to point out that the dry equations we derive mathematically above have a physical analog as well: a two-layer system, with two uniform fluid layers of different densities stably stratified. We thus can expect that the dry system will have standard conservation laws that are expected in physical systems: conservation of energy, etc. The moisture contribution adds a significant amount of complexity. In Section 5.3 we derive an energy conservation law for the system. We additionally derive a law for the derivative system, and then use this to show that the velocity, temperature, and humidity cannot develop discontinuities in finite time. However, due to the parameterization of moisture, it is impossible to derive higher order conservation laws. Therefore it is possible for discontinuities in the vertical velocity, precipitation, temperature derivative, and humidity derivative develop in finite time. We study these discontinuities in more detail in the next chapter.

Chapter 6

The Dynamics of Precipitation Fronts in the Tropical Atmosphere

6.1 Introduction

In Chapter 5, we have derived a simple model to study the large-scale dynamics of moisture and precipitation in the tropical atmosphere. This model is significantly less complex than the GCM of Chapters 2-4, consisting only of two vertical modes coupled to an equation for the vertically integrated moisture content. However this system is a useful starting point for study of the dynamics of precipitation regions in the tropics.

In Section 5.3 of the last chapter, we derived energy conservation laws for the system independent of relaxation time. These estimates allow us to discuss the formal infinitely fast relaxation limit in Section 6.2, which is a novel hyperbolic free boundary problem for the motion of precipitation fronts from a large scale dynamical perspective. Such precipitation fronts are in the Sobolev space H^1, but have jumps in their first derivatives. Elementary exact solutions of the limiting dynamics involving precipitation fronts are developed in detail in Section 6.2 and include three families of waves with discontinuities in the first derivatives: fast drying fronts as well as slow and fast moistening fronts. The last two families of moistening waves violate Lax's shock inequalities for moving discontinuities in hyperbolic systems (Majda, 1984). Nevertheless, Section 6.3 contains detailed numerical experiments which confirm the robust realizability of all three families of precipitation fronts with realistic finite relaxation times.

From the viewpoint of applied mathematics, this chapter studies a new class of strongly nonlinear relaxation systems which has completely novel phenomena as well as features in common with the established applied mathematical theories of relaxation limits for conservation laws (Chen et al. (1994); Jin and Xin (1995); Katsoulakis and Tzavaras (1997)) and waves in reacting gas flows (Majda (1981); Colella et al. (1986); Bourlioux and Majda (1995)). Some of the similarities and differences with the phenomena for reacting gas flow are discussed briefly at the end of Section 6.3 while the general energy decay principle established in Section 5.3 is a common feature with relaxation limits (Chen et al., 1994). Section 6.4 establishes briefly that similar effects also occur in elementary steady state models of the tropical circulation with both forcing and damping.

6.2 The Free Boundary Problem in the Formal Limit of Vanishing Relaxation Time

In the last chapter, we used the formulation of Betts and Miller (Betts (1986); Betts and Miller (1986)) to parameterize precipitation as a function of humidity content, specifically,

$$P = \frac{1}{\tau_c}(q - \tilde{q}(T))^+ \tag{6.1}$$

for some saturation value $\tilde{q}$. In Section 5.3, we have developed conservation laws independent of convective relaxation time. We now consider the formal limit $\tau_c \to 0$, that is, instantaneous convective adjustment. This is known as the "strict quasi-equilibrium limit" (Emanuel et al., 1994) since convection is assumed to keep the moisture or CAPE in a state of quasi-equilibrium (depending on our convective parameterization). Since the estimates that we derived in Sections 5.3.1 and 5.3.2 above are independent of τ_c, we are assured that, at least formally, even in this limit the equations will be well-posed.

Let $\tau_c = \delta$. The moisture equation (5.68) then becomes

$$\frac{\bar{D}q}{Dt} + \bar{Q}\nabla \cdot \mathbf{U_1} = d_q(q_s - q) - \delta^{-1}(q - \tilde{q}(T))^+. \tag{6.2}$$

The term of order δ^{-1} tells us that to leading order,

$$(q - \tilde{q}(T))^+ = 0. \tag{6.3}$$

Therefore the dry region Ω_d, defined as the region where there is no precipitation so $P = 0$, is given by either:

$$q < \tilde{q}(T) \tag{6.4}$$

or

$$q = \tilde{q}(T), \frac{\partial q}{\partial t} \leq 0. \tag{6.5}$$

The formal limit of (6.2) in the moist region, Ω_m, where precipitation occurs and $P > 0$, is given by the constraint

$$q = \tilde{q}(T), \frac{\partial q}{\partial t} > 0. \tag{6.6}$$

With (6.3), the latter constraint, which assures that the precipitation is positive, is equivalent to

$$\frac{\partial q}{\partial t} = -\bar{\mathbf{U}} \cdot \nabla q - \bar{Q}\nabla \cdot \mathbf{U_1} + d_q(q_s - q) > 0. \tag{6.7}$$

Clearly the boundaries between Ω_d and Ω_m can change in time; they are free boundaries. Some physical mechanisms to change these boundaries include the following:

- A moist region develops places with $\nabla \cdot \mathbf{U_1} > 0$, i.e., strong enough low-level divergence to overcome evaporation and become unsaturated.
- A dry region develops a region of strong convergence with $\nabla \cdot \mathbf{U_1} < 0$, creating moisture there.
- Barotropic advection of drier air, i.e., $\bar{\mathbf{U}} \cdot \nabla q$, with $q < \tilde{q}(T)$.
- Rossby waves or Kelvin waves entrain or detrain a moist region and influence it (see Majda (2003)).

Some elementary numerical solutions demonstrating all of these physical effects are reported in Khouider and Majda (2004).

6.2.1 Dry and Moist Waves and Free Boundaries

The behavior of linear disturbances in our system is vastly different for saturated and unsaturated perturbations. To illustrate this in a simple context, we examine the unforced equations without the barotropic mode, equations (5.79) to (5.82). For dry (subsaturated) waves, $P = 0$ so we obtain, from equations (5.79) to (5.81)

$$\begin{aligned} \frac{\partial \mathbf{U_1}}{\partial t} + y\mathbf{U_1}^{\perp} - \nabla T &= 0 && (6.8)\\ \frac{\partial T}{\partial t} - (\nabla \cdot \mathbf{U_1}) &= 0. && (6.9) \end{aligned}$$

These are the well-studied linear two-layer equatorial β-plane equations (see Gill (1982) or Majda (2003) for complete description of this set of equations and the waves therein). These equations support many interesting types of waves including equatorial Kelvin waves, Rossby waves, and mixed Rossby-gravity waves. The Kelvin wave, for instance, is symmetric about the equator, has $T = -u_1$, and propagates with speed $c_d = 1$ (in our nondimensional units).

However, for moist (saturated) disturbances, the precipitation is an important term, and we need to form the moist static energy equation to evaluate the role of disturbances. This is obtained by adding equations (5.81) and (5.82) to obtain

$$\frac{\partial(q+T)}{\partial t} - (1-\bar{Q})\nabla \cdot \mathbf{U_1} = 0. \tag{6.10}$$

Since $q = \hat{q} + \alpha T$ for saturated disturbances, this can be written as

$$\frac{\partial T}{\partial t} - \frac{(1-\bar{Q})}{(1+\alpha)}\nabla \cdot \mathbf{U_1} = 0. \tag{6.11}$$

When this equation is combined with the baroclinic momentum equation (6.8) it is clear that the result is a wave equation with reduced propagation speeds. For instance, the Kelvin wave now propagates with speed $c_m = \sqrt{\frac{1-\bar{Q}}{1+\alpha}}$.

Theoretical studies that have used similar models (e.g., Neelin and Held (1987)) typically take values of $\bar{Q} \approx .8 - .9$, meaning $c_m \approx (.2 - .4)c_d$. This fits with observations as well; the data presented in the observational study of Mapes and Houze (1995) shows clear spectral peak of dry disturbances at $\approx 50 m/s$, and a moist disturbance spectral peak at $\approx 15 m/s$ (see their Figure 15).

It is important to point out that the moist wave speeds are different for different convective parameterization criteria. Moist wave speeds are significantly faster for the fixed saturation ($\alpha = 0$) case than for the CAPE ($\alpha = 1$) case. Since $\bar{Q}$ is often chosen to produce moist wave speeds in accordance with observations, care must be taken when choosing this constant for different convective criteria.

We have shown that there is a significant gap between the propagation speeds of dry and moist disturbances. It is this fact that motivates our work below, where we study the implication of the two different wave speeds. The problem is made more complex by the fact that the free boundary between dry and moist regions evolves in time.

6.2.2 Precipitation Front Propagation

For conceptual simplicity, we now consider the one-dimensional version of this system, which represents flow in the zonal direction around the equator. This simplification is meaningful as a first approximation because much of the important dynamics in the tropics occurs in the zonal direction, including the Walker circulation, propagation of superclusters, and the Madden-Julian Oscillation. However, the dynamics we study here can easily be extended to the 2-dimensional equatorial longwave approximation, or to the full 2-dimensional system (see Majda (2003) Chap. 9).

With this approximation, we need not consider the Coriolis force, which is dominant in midlatitudes but disappears on the equator. Further, the only appropriate value for the barotropic velocity $\bar{\mathbf{U}}$ is a constant over the domain, which we denote by $\bar{u}$. The nondimensional equations for this system are therefore

$$\begin{aligned}
\frac{\partial u}{\partial t} + \bar{u}\frac{\partial u}{\partial x} &= \frac{\partial T}{\partial x} - \bar{d}u && (6.12)\\
\frac{\partial T}{\partial t} + \bar{u}\frac{\partial T}{\partial x} &= \frac{\partial u}{\partial x} - d_T(T - T_{eq}) + d_{SH}(T_s - T) + \frac{(q - \tilde{q}(T))^+}{\tau_c} && (6.13)\\
\frac{\partial q}{\partial t} + \bar{u}\frac{\partial q}{\partial x} &= -\bar{Q}\frac{\partial u}{\partial x} + d_q(q_s - q) - \frac{(q - \tilde{q}(T))^+}{\tau_c} && (6.14)
\end{aligned}$$

where u is now the zonal (eastward in the lower layer) first baroclinic mode velocity (we have dropped the subscript “1” now since this is the only dynamic velocity now) and all other variables are the same. Another important relation is the vertical velocity equation from (5.24) above which becomes:

$$w = -u_x. \tag{6.15}$$

We have shown in Section 5.3.2 that while discontinuities in q, T, and u cannot form from smooth initial conditions, it is possible that discontinuities in the derivatives of these quantities (and hence vertical velocity and precipitation) can occur out of smooth initial conditions. With this fact in mind, we now investigate the dynamics of solutions with a discontinuity in these quantities under the formal limit of $\tau_c \to 0$. We call these "precipitation fronts" since there is a discontinuity in precipitation. The fields u, T, and q only have a kink in them; there is a discontinuity in u_x, T_x, and q_x.

We consider the free wave problem with no barotropic wind, that is, $\bar{u} = \bar{d} = d_q = d_T = d_{SH} = 0$:

$$\frac{\partial u}{\partial t} = \frac{\partial T}{\partial x} \tag{6.16}$$

$$\frac{\partial T}{\partial t} = \frac{\partial u}{\partial x} + P \tag{6.17}$$

$$\frac{\partial q}{\partial t} = -\bar{Q}\frac{\partial u}{\partial x} - P. \tag{6.18}$$

The derivative form of equations (6.16) to (6.18) in this limit, obtained by taking the x-derivative and substituting the vertical velocity from equation (6.15) is:

$$\frac{\partial w}{\partial t} = -\frac{\partial T_x}{\partial x} \tag{6.19}$$

$$\frac{\partial T_x}{\partial t} = -\frac{\partial w}{\partial x} + P_x \tag{6.20}$$

$$\frac{\partial q_x}{\partial t} = +\bar{Q}\frac{\partial w}{\partial x} - P_x \tag{6.21}$$

The jump conditions for equations (6.19) to (6.21) are as follows:

$$
\begin{aligned}
-s[w] &= -[T_x] && (6.22)\\
-s[T_x] &= -[w] + [P] && (6.23)\\
-s[q_x] &= +\bar{Q}[w] - [P] && (6.24)
\end{aligned}
$$

where s is the front propagation speed and $[f] = f_+ - f_-$.

First, there exist solutions which occur entirely within the dry and moist region. For solutions within the dry region, $[P] = 0$, and therefore we can solve equations (6.22) and (6.23) to obtain $s = \pm 1$, the dry wave speed. For fronts entirely within the moist region, we can add equations (6.23) and (6.24) and solve to obtain $s = \pm\frac{(1-\bar{Q})}{1+\alpha}$, the moist wave speed. These solutions are not surprising, as the character of the propagation is the same as for continuous disturbances. The more interesting fronts occur at the interface between dry and moist regions, where the discontinuity in precipitation causes different propagation speeds.

To allow further study of the case with fronts at the interface between dry and moist regions, we assume, without loss of generality, that the moist region is on the positive side of the $x-$axis, and the dry region is on the negative side. We can derive conditions for the movement of the interface between dry and moist regions using the moisture constraints imposed formally by (6.3)-(6.7) in a single space dimension. First, since we are saturated in the moist region, we use the convective criterion (equation (5.58)) and the continuity of q to obtain

$$q(0) = \hat{q} + \alpha T(0) \tag{6.25}$$

at the interface. Further, to stay saturated in the moist region, we need to have

$$q_{x+} = \alpha T_{x+}. \tag{6.26}$$

Then, to assure that there is no precipitation in the dry region, we require

$$q_{x-} \geq \alpha T_{x-}. \tag{6.27}$$

Now, (6.26) and (6.27) imply

$$[q_x] \leq \alpha [T_x]. \tag{6.28}$$

Finally, we can calculate the precipitation in the moist region by adding equation (6.18) to $-\alpha$ times equation (6.17) and solving to yield

$$P_+ = \frac{(\alpha + \bar{Q})}{(1+\alpha)} w_+. \tag{6.29}$$

Since this quantity must be positive, we also have

$$w_+ > 0. \tag{6.30}$$

Of course, this just means that we have rising air in the saturated region which is physically consistent. Using these constraints, we can calculate the solutions for the precipitation fronts.

Proposition: With the saturated region initially at $x > 0$ in accordance with equations (6.25)-(6.27), there are 3 branches of solutions of equations (6.22)-(6.24) for precipitation fronts depending on the values of the jumps in the derivatives:

- A branch of *drying fronts* with wave speeds in between the dry and moist wave speeds moving into the moist region ($1 > s > (\frac{1-\bar{Q}}{1+\alpha})^{\frac{1}{2}}$)
- A branch of *slow moistening fronts*, with speeds in between the moist speed and zero propagating into the dry region ($0 > s > -(\frac{1-\bar{Q}}{1+\alpha})^{\frac{1}{2}}$)
- A branch of *fast moistening fronts* moving into the dry region with speed above the dry wave speed ($s < -1$).

Proof: Solving the equations (6.22) to (6.24) with the constraints (6.26) to (6.29) gives the following relations:

$$s = \pm(1 - \frac{\frac{(\alpha+\bar{Q})}{(1+\alpha)}w_+}{[w]})^{\frac{1}{2}} \tag{6.31}$$

$$[T_x] = s[w] \tag{6.32}$$

$$[q_x] = (\frac{1-\bar{Q}}{s} - s)[w]. \tag{6.33}$$

This set of equations provides a method of constructing exact solutions from arbitrary initial jumps. For instance, given a vertical velocity $[w]$, one can calculate the necessary $[T_x]$ and $[q_x]$ to produce a balanced propagating front.

We now investigate the allowed phase speeds for these waves. For real phase speeds, we must have either

$$w_- \leq (1 - \frac{\alpha+\bar{Q}}{1+\alpha})w_+ \tag{6.34}$$

or

$$w_- \geq w_+. \tag{6.35}$$

Using the constraint (6.28), the bounds on the speed of the front are then

$$1 > s > (\frac{1-\bar{Q}}{1+\alpha})^{\frac{1}{2}} \text{ for } w_- < 0 \tag{6.36}$$

or

$$0 > s > -(\frac{1-\bar{Q}}{1+\alpha})^{\frac{1}{2}} \text{ for } 0 < w_- < (1 - \frac{\alpha+\bar{Q}}{1+\alpha})w_+ \tag{6.37}$$

or

$$s < -1 \text{ for } w_- > w_+. \tag{6.38}$$

The dry wave speed is $c_d = 1$, and the moist wave speed is $c_m = \sqrt{\frac{1-\bar{Q}}{1+\alpha}}$, so the above constraints can be rewritten as:

$$c_d > s > c_m \tag{6.39}$$

or

$$0 > s > -c_m \tag{6.40}$$

or

$$s < -c_d. \tag{6.41}$$

The first branch of front speeds (equation (6.36)) we call the drying front, since it propagates from the dry region into the moist region. Note that w_- is negative for these drying waves so the state adjacent to the moist region has downdrafts and divergence at the bottom of the troposphere consistent with drying. This family of fronts exactly spans the region between dry and moist wave speeds, which is the exact range given for stability of fronts by Lax's Stability Criterion (Majda, 1984).

The second branch (equation (6.37)) we call the slow moistening fronts. This branch is particularly interesting because it produces movement of the interface between dry and moist at a speed that is below the moist wave speed. Note that according to (6.37), w_- is positive with low level convergence in the flow field but bounded from above by a multiple less than one of w_+; furthermore, slower waves have larger w_- in the unsaturated state.

The final branch (equation (6.38)) we call the fast moistening front. This consists of moistening propagating at speeds faster than the dry wave speed. According to (6.38) and (6.15), the fast moistening occurs from large convergence in the dry region, which brings the dry region to saturation rapidly.

Note the important asymmetry between "drying waves" (with $s > 0$, that is, the precipitation front propagating into the moist region) and "moistening waves" (with $s < 0$). The moistening waves both violate Lax's stability criterion so it becomes interesting to understand their potential dynamical significance; this is a main topic in Section 6.3.

Since the front speeds are bounded by the dry and moist wave speeds, there is no difference in allowed propagation speeds between systems with different convective criteria (i.e., different α). However, systems with the same initial discontinuities do not behave the same as α is varied, since α appears in equation (6.31). Next, we investigate the effect of finite relaxation time, as well as the effective differences among systems with different convective criteria in a numerical model.

6.3 Numerical Simulation of Fronts

We now present numerical results of simulations of these fronts over a range of convective relaxation times, demonstrating that the theoretical predictions made in Section 6.2.2 in the limit of $\tau_c \to 0$ are surprisingly accurate up to large values of the relaxation time. Even the two moistening fronts which violate Lax's Stability Criterion are readily realizable in the numerics presented below. We additionally investigate sensitivity to the convective criterion, and to the numerical mesh.

6.3.1 Description of Numerical Model

We numerically simulate the one-dimensional forced-dissipative system with arbitrary relaxation time, i.e., equations (6.12) to (6.14). Since we are considering a somewhat stiff problem (with small convective relaxation times), care must be taken when designing the numerical method. First of all, by considering the quantity $Z_0 = q + \bar{Q}T$, introduced earlier in (5.70), one of the equations becomes an ODE in the absence of mean wind. Secondly, we can isolate the westward and eastward moving waves by using the characteristics $Z_E = u - T$ and $Z_W = u + T$ as variables (the subscripts represent eastward and westward propagation, respectively).

Therefore the equations we integrate are:

$$
\begin{aligned}
\frac{\partial Z_E}{\partial t} + \bar{u}\frac{\partial Z_E}{\partial x} + \frac{\partial Z_E}{\partial x} &= -S_{T,R} - S_{T,SH} + S_u - P && (6.42)\\
\frac{\partial Z_W}{\partial t} + \bar{u}\frac{\partial Z_W}{\partial x} - \frac{\partial Z_W}{\partial x} &= S_{T,R} + S_{T,SH} + S_u + P && (6.43)\\
\frac{\partial Z_0}{\partial t} + \bar{u}\frac{\partial Z_0}{\partial x} &= \bar{Q}S_{T,R} + E - (1-\bar{Q})P && (6.44)
\end{aligned}
$$

where $S_{T,R} = -d_T(\frac{Z_E+Z_W}{2} - T_{eq})$, $S_{T,SH} = d_{SH}(T_s - \frac{Z_E+Z_W}{2})$, $S_u = \bar{d}(\frac{Z_E-Z_W}{2})$, $E = d_q(q_s - Z_0 + \frac{\bar{Q}}{2}(Z_E+Z_W))$, and $P = \frac{(Z_0 - \frac{\bar{Q}}{2}(Z_E+Z_W) - \tilde{q}(T))^+}{\tau_c}$.

For numerical integration of the scalar wave equations, we use the 3rd order ENO scheme (Harten et al., 1987) for spatial differencing. This provides a high order of accuracy, while preserving very sharp resolution near fronts with minimal numerical dissipation.

An added difficulty is that the precipitation term is stiff for small values of τ_c; essentially this term can cause unphysical oscillations, and even reduction of q below its saturation value for $\tau_c \sim \Delta t$. Therefore for time integration, we use Strang time splitting on this term, which gives 2nd order in time accuracy, and facilitates simulation of the precipitation term to small values of τ_c. The typical mesh spacing used is .0267 (40 km), so we expect the shocks to be well resolved within 100 km. We use a small time step of .0033 (100 seconds) to resolve the short-time relaxation effects.

6.3.2 Simulations

The basic parameters we use in the simulations below are the following:

$$\bar{Q} = .9, \alpha = 0, \hat{q} = .9. \qquad (6.45)$$

The Drying Front

We first simulate a drying front. The initial conditions for this simulation are

$$
\begin{aligned}
w_+ &= .01 && (6.46)\\
T_{x+} &= 0 && (6.47)\\
q_{x+} &= 0 && (6.48)\\
w_- &= -.01 && (6.49)\\
T_{x-} &= -.02\sqrt{.55} = -.0148 && (6.50)\\
q_{x-} &= \frac{.009}{\sqrt{.55}} = .0121 && (6.51)
\end{aligned}
$$

which yield a balanced front with speed $s = \sqrt{.55} = .742$ in the formal limit of vanishing relaxation time. We simulate using a range of convective relaxation times: $\tau_c = .0625, .25$, and 1.5 in nondimensional units (30 min, 2 hrs, and 12 hrs, respectively). The 12 hour relaxation time is that found in Bretherton et al. (2004), 2 hours is typically used with the Betts-Miller convection scheme in general circulation models, and the 30 minute relaxation time simulations are performed to get an idea of how close we are to the $\tau_c \rightarrow 0$ limit.

Figure 6.1 shows space-time plots of the precipitation for this drying front at the three relaxation times, along with the predicted front speed (the black dotted line in each plot). The time of simulation is $t = 13.33$, or 4.44 days in dimensional units. All simulations agree with the predicted front speed quite well, if one considers the center of the front region. The $\tau_c = .0625$ simulation is virtually identical to predictions for all time, and the front remains very abrupt. Only small deviations from the prediction can be seen for the .25 relaxation time simulation. In the simulation with $\tau_c = 1.5$, however, the front has been smoothed out quite a bit. The center of the front region still agrees with the predicted speed quite well though.

We next demonstrate that the smoothing of the front primarily occurs during the "spin-up" of the fronts, i.e., the adjustment time it takes for the precipitation to

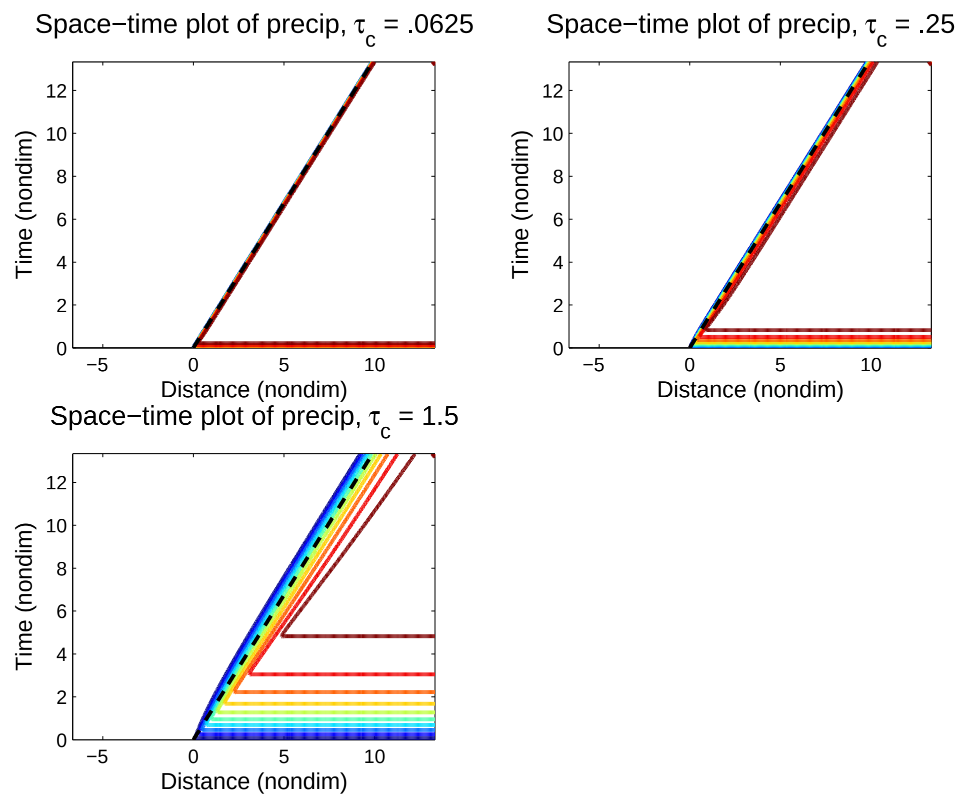

Figure 6.1: Space-time diagrams of precipitation for the drying front simulations.

reach its proper value, and that the fronts propagate steadily after a certain time. The steady state of the precipitation in the unperturbed moist region for these cases is $P_+ = \bar{Q}w_+ = .009$, implying a steady state humidity of $q_+ = \tilde{q} + \tau_c P_+ = .9 + .009\tau_c$. Since the initial condition for the humidity begins exactly at the saturation value (.9), it takes on the order of the convective relaxation time for adjustment to this steady state to occur. As can be seen from Figure 6.1, this amount of time is approximately $2\tau_c$ for each of the simulations.

The steady shapes of the precipitation profiles can be seen in Figure 6.2, which contains plots at different time slices for the three drying fronts, shifted by the predicted speed. That is, we plot $P(x - st, t)$ for $t = 1.2, t = 2.4$, and $t = 12$ where $s = \sqrt{.55}$, the predicted speed. There is a significant difference in distance scale for the three plots. The two smaller relaxation cases both converge to the steady profile quickly. The spinup of precipitation can be seen more clearly in the $\tau_c = 1.5$ simulation, as the $t = 1.2$ and $t = 2.4$ slices are both in the process of adjusting. Even the $t = 12$ slice is not completely at steady state for this case, so we additionally plot a time slice at $t = 36$ to indicate the steady state. The simulations do not drift from these steady states once reached.

Plotting the vertical velocity (Figure 6.3), one can see that there are dry waves propagating into the dry region created in the adjustment process. The fetch of these waves is proportional to the adjustment time, with the front expelling waves until approximately $t = 2\tau_c$.

From these simulations we can conclude that our theory regarding the limit as $\tau_c \to 0$ can be applied to the realistic adjustment cases. The structure of the fronts are steady in the moving frame provided $t \gg \tau_c$, where t is the time over which the integration is performed.

The Slow Moistening Front

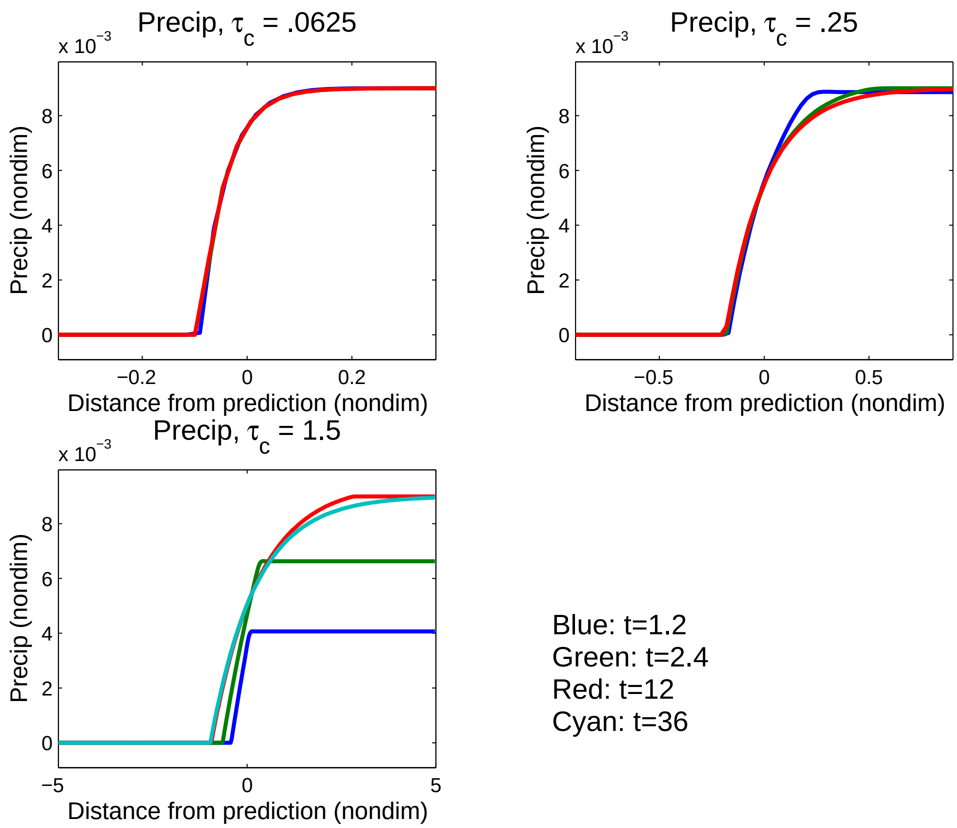

Figure 6.2: Precipitation for the drying fronts at t=1.2, t=2.4, and t=12 vs. distance recentered by the theoretical prediction for shock position. t=36 is additionally plotted for the $\tau_c = 1.5$ case. Note the different distance scales for each simulation.

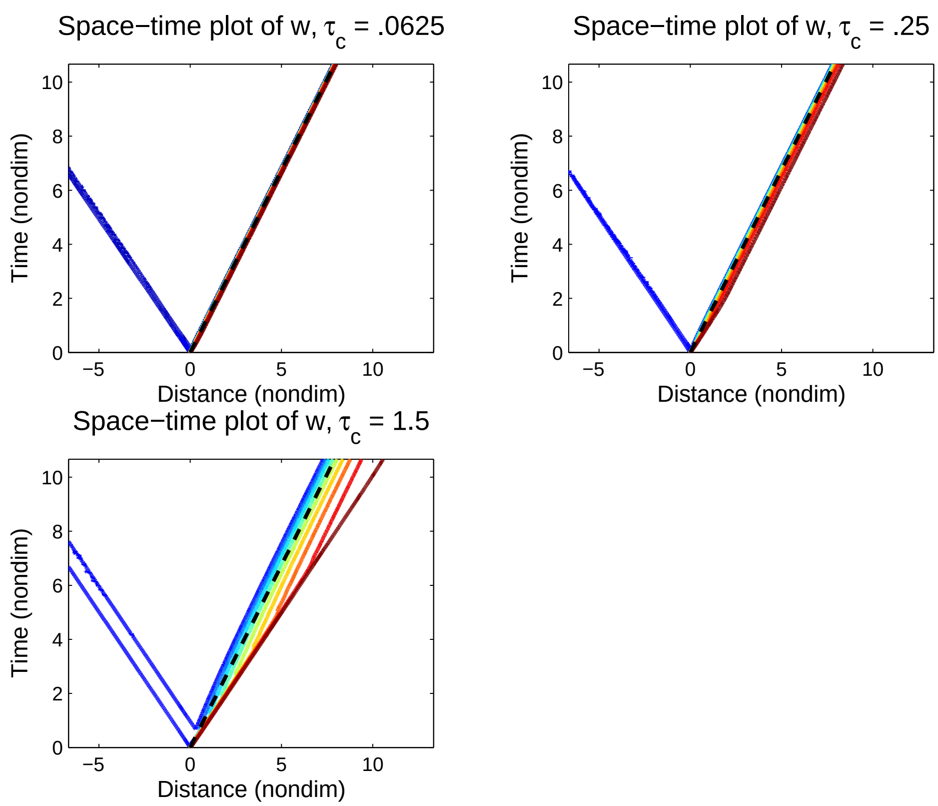

Figure 6.3: Space-time diagrams of vertical velocity for the drying front simulations.

We next simulate the slow moistening front, with initial conditions as follows:

$$w_+ = .01 \tag{6.52}$$

$$T_{x+} = 0 \tag{6.53}$$

$$q_{x+} = 0 \tag{6.54}$$

$$w_- = \frac{1}{1300} = .000769 \tag{6.55}$$

$$T_{x-} = \frac{3\sqrt{.1}}{650} = .00146 \tag{6.56}$$

$$q_{x-} = \frac{9\sqrt{.1}}{650} = .00438 \tag{6.57}$$

which creates a balanced front with speed $s = -\frac{\sqrt{.1}}{2} = -.158$ in the formal limit of vanishing relaxation time. The plots for this wave (Figure 6.4) are given for the same time period, $t = 13.33$, and are displayed on a slightly smaller spatial domain. Again the speeds are well-predicted by our $\tau_c \to 0$ theory, when the center of the front region is considered. However more spreading of the fronts is observed here, which again primarily occurs during the precipitation adjustment period. This is clear in the $\tau_c = .25$ simulation as well as the $\tau_c = 1.5$. For instance, the $\tau_c = 1.5$ front is approximately 75% wider than the corresponding drying front in the previous case.

Examining the vertical velocities (Figure 6.5), one can see that there are now both dry waves (propagating into the dry region) and moist waves (propagating into the moist region) being emitted from the front during the adjustment phase. The influence of the moist waves can be seen in the precipitation fields in Figure 6.4. The character of the dry waves is similar to the dry waves being emitted from the drying front, i.e., propagation at the dry phase speed with width proportional to the adjustment time. The behavior of the moist waves is more complex. After an adjustment period (here approximately $t = 4\tau_c$), the moist wave simply propagates into the moist region at the moist speed. However, prior to this, the wave expands,

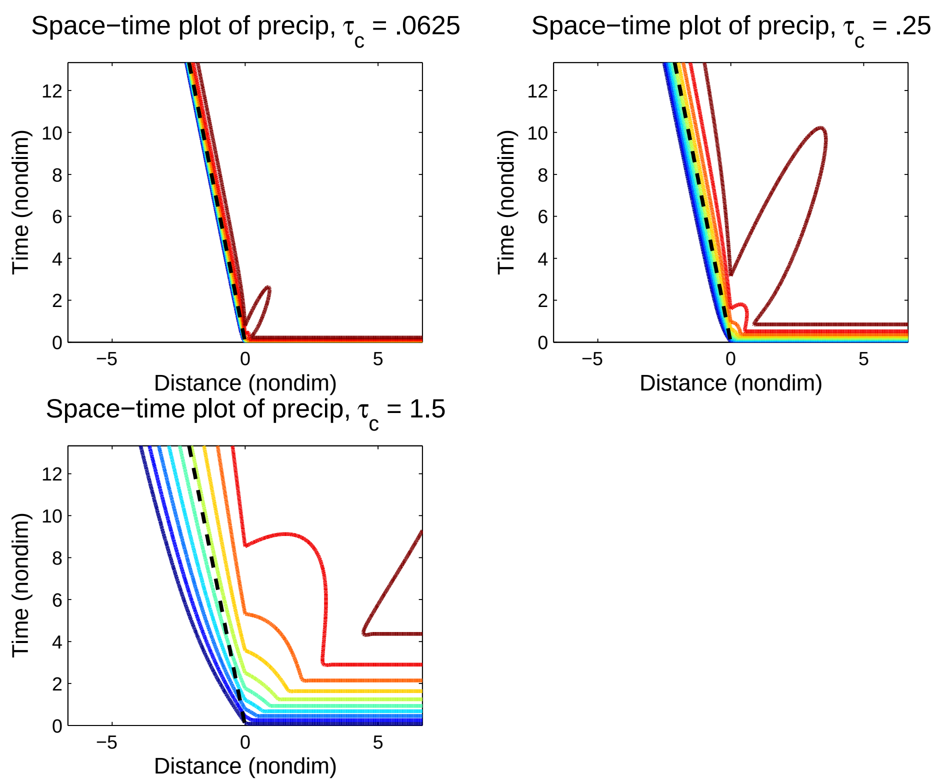

Figure 6.4: Space-time diagrams of precipitation for the slow moistening front simulations.

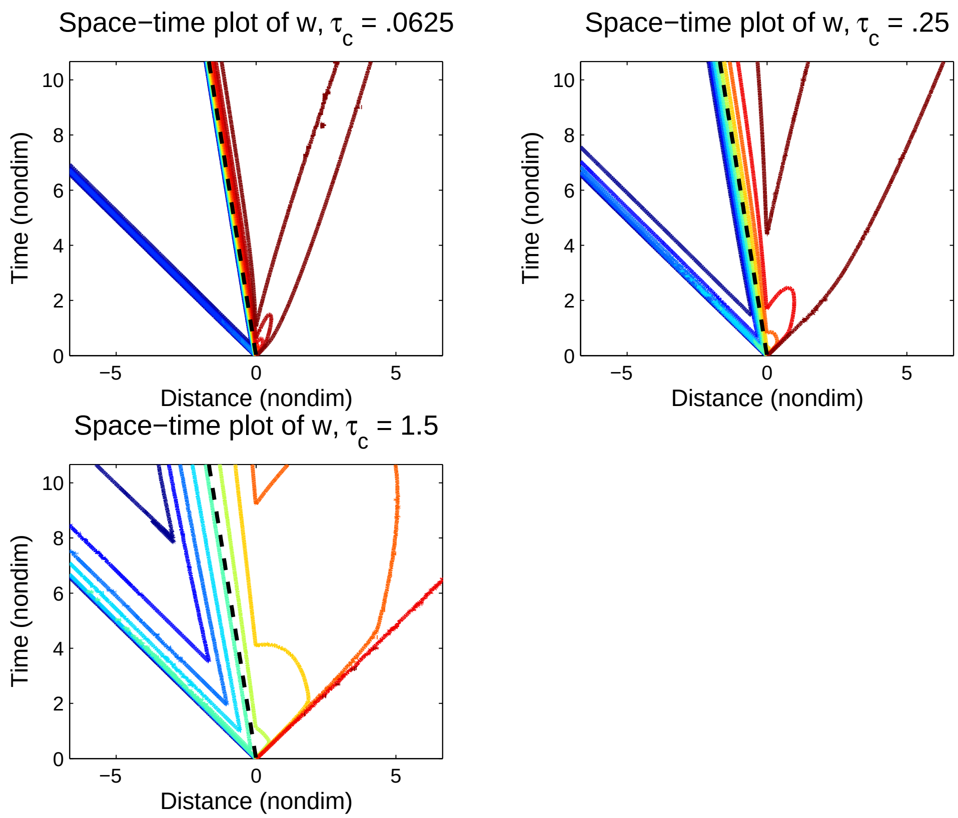

Figure 6.5: Space-time diagrams of vertical velocity for the moistening front simulations.

with the boundary on the positive side moving at the dry wave speed. Propagation at speeds above the moist wave speed in precipitating regions can occur in the system where $\tau_c > 0$, since changes in divergence do not immediately affect the precipitation. Specifically, the assumption that $q = \hat{q} + \alpha T$, which we used between equations (6.10) and (6.11) in deriving the properties of moist disturbances in Section 6.2.1 breaks down. When the precipitation is adjusting to its steady value given a certain velocity divergence, small wave perturbations to this do not affect the evolution of the precipitation much, and hence the waves propagate more like dry disturbances.

In Figure 6.6 we plot the vertical velocities at different times, recentered by the predicted front speed. In these plots one can see the structure of the dry waves propagating away from the interface, as well as some of the moist wave propagation.

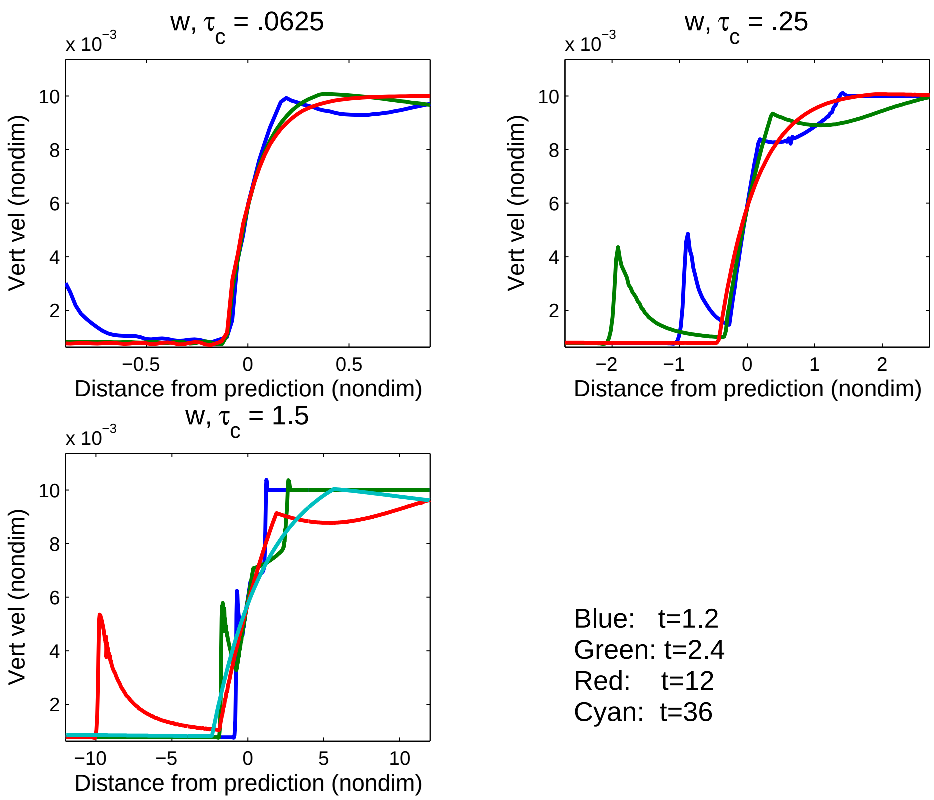

Figure 6.6: Vertical velocity for the slow moistening fronts at t=1.2, t=2.4, and t=12 vs. distance recentered by the theoretical prediction for shock position. t=36 is additionally plotted for the $\tau_c = 1.5$ case.

Again all of these waves eventually propagate with a steady shape after a certain length of time, approximately given by the $t = 36$ plot for the $\tau_c = 1.5$ case, and the $t = 12$ plots in the shorter relaxation time cases. Keeping in mind the different spatial scales in the plots, the emerging steady states clearly retain the same smoothed shape for the two smaller relaxation times; also see figures 6.7 and 6.8 below which confirms this.

Since we believe this wave is the most interesting to the atmospheric science community (due to its reduced phase speeds), we now examine the sensitivity of these simulations to both resolution (by considering 2x and .5x resolutions) and convective parameterization (by constructing a wave with a similar propagation speed in the CAPE parameterization). First, plots similar to Figure 6.6 for double and half reso-

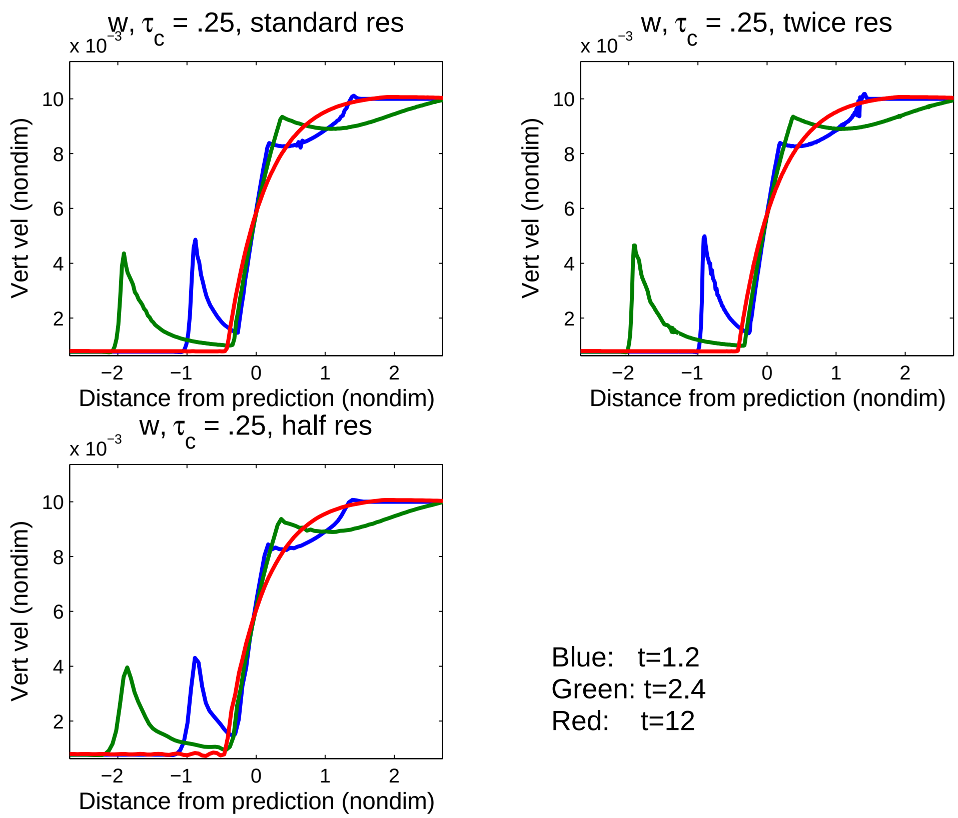

Figure 6.7: Testing resolution with the $\tau_c = .25$ simulation: vertical velocity with rescaled distance at t=1.2, t=2.4, and t=12.

lution are given in Figure 6.7 and 6.8. These plots give time slices of vertical velocity (which exhibits the largest change with resolution) for the $\tau_c = .25$ case (Fig. 6.7) and the $\tau_c = .0625$ case (Fig. 6.8). The primary difference evident in these plots is not in the fronts, which are all nearly identical, but rather with the dry waves propagating away, which are slightly better defined for the cases with higher resolution. This gives us faith in the numerical simulation of the precipitation fronts however.

We next consider a slow moistening front with the same speed under the CAPE

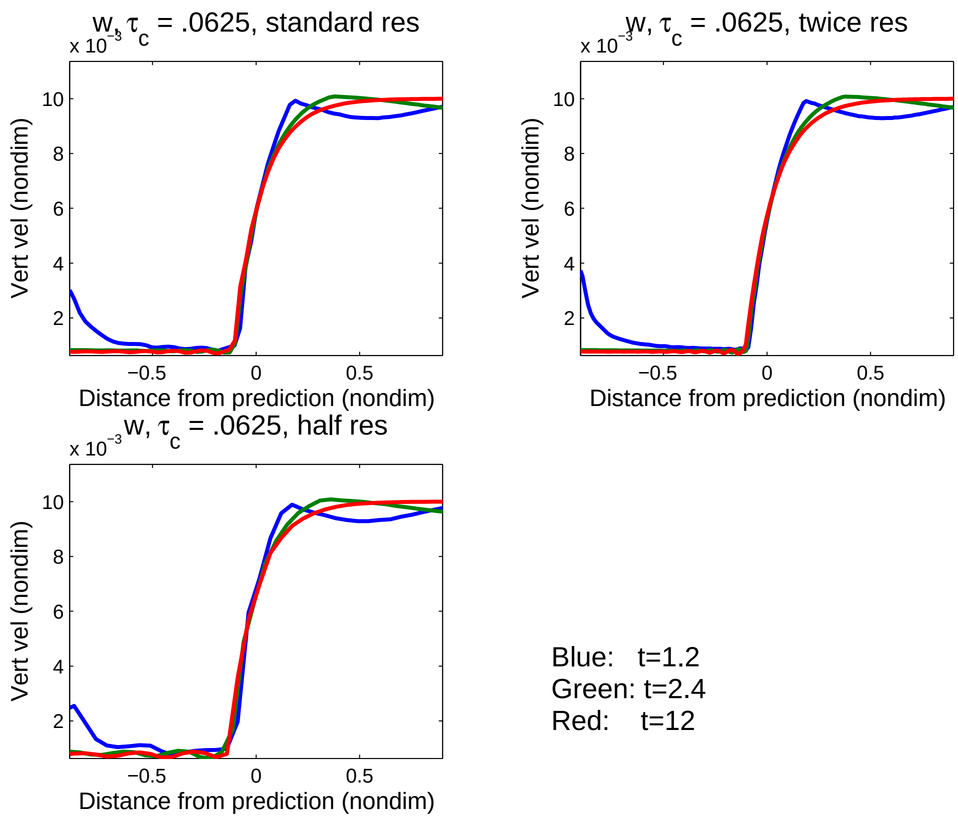

Figure 6.8: Testing resolution with the $\tau_c = .0625$ simulation: vertical velocity with rescaled distance at t=1.2, t=2.4, and t=12.

parameterization ($\alpha = 1$) which is constructed by using the following values:

$$w_+ = .01 \tag{6.58}$$

$$T_{x+} = 0 \tag{6.59}$$

$$q_{x+} = 0 \tag{6.60}$$

$$w_- = \frac{1}{3900} = .000256 \tag{6.61}$$

$$T_{x-} = \frac{19\sqrt{.1}}{3900} = .00154 \tag{6.62}$$

$$q_{x-} = \frac{19\sqrt{.1}}{1300} = .00462 \tag{6.63}$$

which again gives a theoretical propagation speed of $s = -\frac{\sqrt{.1}}{2}$. Again, the theoretical prediction for the is strikingly accurate (Figure 6.9). There is a small amount more smoothing of the front here as compared with the fixed saturation case; these fronts also take slightly longer to reach steady state (despite the fact that the precipitation adjusts faster in the $\tau_c = 1.5$ case). Other than these observations, the shape of the fronts, the character of the propagation, and the agreement with theoretical predictions are similar to the cases with $\alpha = 0$.

The Fast Moistening Front

Finally we simulate the fast moistening front, with the following initial conditions:

$$w_+ = .01 \tag{6.64}$$

$$T_{x+} = 0 \tag{6.65}$$

$$q_{x+} = 0 \tag{6.66}$$

$$w_- = .013 \tag{6.67}$$

$$T_{x-} = -.006 \tag{6.68}$$

$$q_{x-} = .00585 \tag{6.69}$$

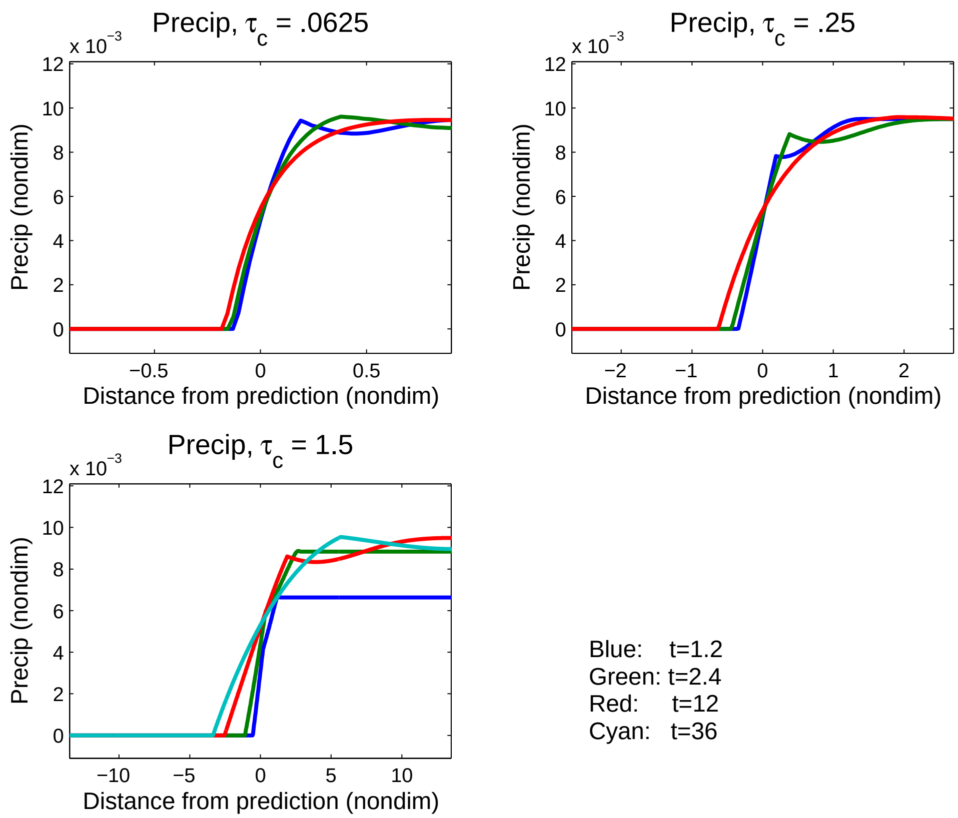

Figure 6.9: Precipitation for the slow moistening fronts with the CAPE parameterization at t=1.2, t=2.4, and t=12 vs. distance recentered by the theoretical prediction for shock position. t=36 is additionally plotted for the $\tau_c = 1.5$ case.

which gives a speed of $s = -2$ in the formal limit of vanishing relaxation time. In Figure 6.10, we plot time slices of the precipitation for the three values of τ_c for this case. Despite its predicted propagation of twice the dry wave speed, this wave is still realizable numerically, and the theoretical predictions are still quite accurate for all three cases. The primary difference from other simulations is that the waves lag behind the theoretical predictions in all three cases due to a phase shift in the adjustment process. This is not surprising since the front propagation speed is faster than any allowed characteristic wave speed; while the precipitation is ramping up to its steady value, the front falls behind the theoretical prediction. The waves still reach a steady state in the moist reference state in this case, though, which is similar to the other cases. The lags, measured by the location of half maximum, are approximately .2, .5, and 2 for $\tau_c = .0625, .25$, and 1.5, respectively. The waves actually reach their steady shape more quickly in this case than for the drying and slow moistening fronts.

Remark: The three branches of precipitation fronts, drying, slow and fast moistening, are reminiscent of the three branches of wave fronts in reacting gas flow, strong detonations, flame fronts, and weak detonations (Williams, 1985) which satisfy the analogous wave speed bounds in (6.39), (6.40), (6.41), respectively. In combustion the strong detonations, which satisfy Lax's shock inequalities as in (6.39) are always realizable (Majda (1981); Bourlioux and Majda (1995)) while flame fronts satisfying (6.40) propagate at speeds that are determined as a nonlinear eigenvalue problem through a subtle balance of reaction and diffusion (Williams, 1985); weak detonations satisfying (6.41) are even more elusive and hard to realize (Majda (1981); Colella et al. (1986)) with special values of diffusion rates needed. The numerical results just presented for precipitation fronts show that for the atmospheric models considered here, all three types of precipitation fronts are realizable as large time limits for any finite relaxation time τ_c with only finite one-sided relaxation as a subtle damping mechanism and with negligible dependence on (numerical) diffusion coefficients. One

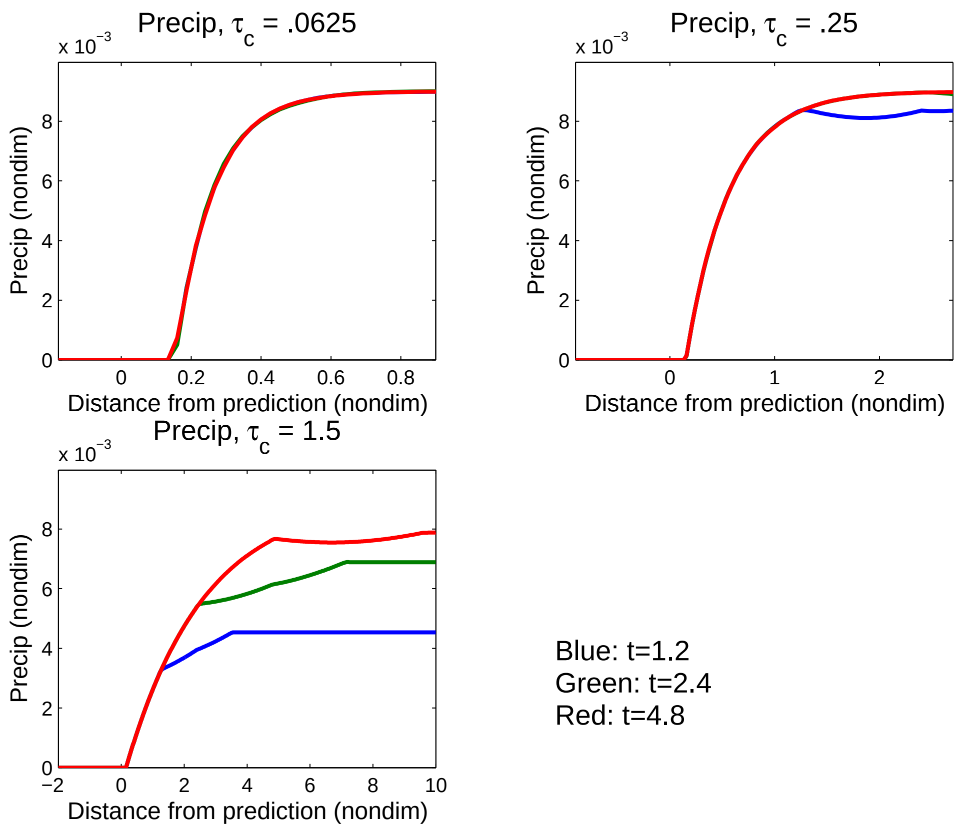

Figure 6.10: Precipitation for the fast moistening fronts at t=1.2, t=2.4, and t=12 vs. distance recentered by the theoretical prediction for shock position.

significant difference in the behavior of the system studied in Section 6.2 is that the basic jump discontinuities occur in the first derivatives of the solution while the nonlinear source terms involve the smoother integrals involving values of the functions themselves; thus, the finite time relaxation effects create a relatively smoother and thus more realizable background environment for the propagation of discontinuities in first derivatives. This is not the case in reacting gas flow where both the nonlinear source terms and the discontinuities occur at the level of primitive variables such as temperature.

6.4 1-Dimensional Walker Cell Solutions

The Walker Cell

The Walker Cell is the zonal circulation of the atmosphere at the equator. Over the warmest sea surface temperatures in the western Pacific Ocean "warm pool," air rises, and subsides in areas of colder sea surface temperatures; this flow is the Walker Circulation. We model this with the 1-D forced-dissipative system (equations (6.12) to (6.14)) by setting up sample sea surface temperature distributions representing the warm pool (the parameter q_s in the evaporation parameterization), and simulating the precipitation response, integrated to a steady state, over a periodic domain all the way around the equator.

We show in this section that even over smooth sea surface temperature distributions, discontinuities in precipitation can develop in this Walker cell model, which provides further physical justification for our study of precipitation fronts in the previous sections. We begin by analyzing what is required to create a discontinuity in precipitation in this model for steady states in the limit of $\tau_c \to 0$.

Solutions in the Limit of $\tau_c \to 0$

The equations we analyze formally below are the steady state of equations (6.12) to (6.14):

$$\bar{u}\frac{\partial u}{\partial x} = \frac{\partial T}{\partial x} - \bar{d}u \quad (6.70)$$
$$\bar{u}\frac{\partial T}{\partial x} = \frac{\partial u}{\partial x} - d_T(T - T_{eq}) + d_{SH}(T_s - T) + P \quad (6.71)$$
$$\bar{u}\frac{\partial q}{\partial x} = -\bar{Q}\frac{\partial u}{\partial x} + d_q(q_s - q) - P \quad (6.72)$$

where $P = \frac{(q-\tilde{q}(T))^+}{\tau_c}$ in the limit of $\tau_c \to 0$. Our reasoning below is somewhat formal but instructive. From the moisture equation (6.72), we obtain

$$P = d_q(q_s - q) - \bar{Q}\frac{\partial u}{\partial x} - \bar{u}\frac{\partial q}{\partial x}. \quad (6.73)$$

For there to be a discontinuity in P, there must be a corresponding discontinuity in at least one of these three terms. As we showed in Section 5.3.2, discontinuities in q, T, or u cannot occur out of smooth initial conditions and we assume that the steady state in (6.70)-(6.72) arises formally as the large time asymptotic limit from smooth initial data for each τ_c. Therefore the discontinuity must be from either the second or third term in the above, i.e., either $\frac{\partial u}{\partial x}$ or $\frac{\partial q}{\partial x}$ must be discontinuous for P to be discontinuous. This also implies that in the absence of mean wind ($\bar{u} = 0$), P is discontinuous if and only if $\frac{\partial u}{\partial x}$ is also discontinuous.

Now consider the moist static energy equation derived from adding equations (6.71) and (6.72) (this eliminates the precipitation term):

$$\bar{u}\frac{\partial(T+q)}{\partial x} = (1-\bar{Q})\frac{\partial u}{\partial x} + d_q(q_s - q) - d_T(T - T_{eq}) + d_{SH}(T_s - T) + d_q(q_s - q) \quad (6.74)$$

In the case where $\bar{u} = 0$, one can solve for $\frac{\partial u}{\partial x}$ as a function of continuous variables only. Therefore with no mean wind, there can be no discontinuity in precipitation. With mean wind, there is no such guarantee, and discontinuities are possible.

Bretherton and Sobel (2002) discuss the variation of the Walker cell with sea surface temperature gradients in a model to similar to ours (essentially a 1-D version of the QTCM). They observe that in their model, nonlinear advection of moisture is key for the presence of precipitation discontinuities. Since they use no linear advection by mean wind, this is obviously connected to the result above.

6.4.1 Numerical Results

We simulate steady Walker cell solutions using the following parameters:

$$\bar{Q} = .9, \alpha = 0, \hat{q} = .9, d_{SH} = 0, d_q = \frac{1}{24}, d_T = \frac{1}{48}, \bar{d} = 0, T_{eq} = -.6 \tag{6.75}$$

We vary the convective relaxation time τ_c and the mean wind $\bar{u}$ in the following simulations. The distribution of q_s is the following:

$$q_s = \begin{cases} 1.1 & \text{for } 0 < x < \frac{3}{8}R_E \text{ and } \frac{5}{8}R_E < x < R_E \\ 1.1 + .26 sin\left(\frac{4\pi}{R_E}(x - \frac{3}{8}R_E)\right) & \text{for } \frac{3}{8}R_E < x < \frac{5}{8}R_E \end{cases} \tag{6.76}$$

which represents a sea surface temperature perturbation of 3 K over the warm pool (one-fourth of the domain) with $R_E = 26.67$, the Earth's circumference. Figure 6.11 contains simulations with $\tau_c = .0625$ (30 minutes) using this distribution of q_s, varying mean wind from 0 to $-.1$. There is additionally one simulation with $\tau_c = .25$ and $\bar{u} = -.1$. The upper limit mean wind (5 m/s) is still within realistic values of the mean easterly winds at the equator. Clearly, for each of the simulations with small τ_c and mean winds, the precipitation distribution is approximately discontinuous. The simulation with no mean wind is smooth as expected. However, the simulation with larger τ_c is not nearly as abrupt in transition as the simulations with smaller τ_c. These simple simulations demonstrate that the concept of precipitation front developed in Sections 6.2 and 6.3 is useful and realizable even for steady state solutions with

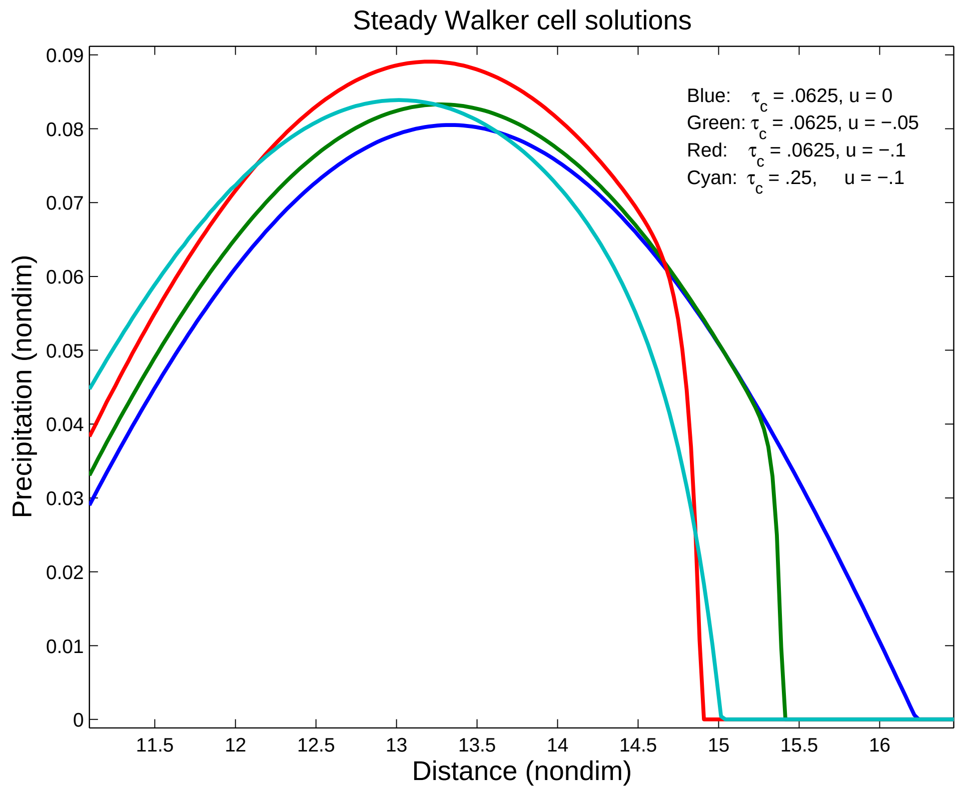

Figure 6.11: Steady Walker cell solutions, $\tau_c = .0625$ and $\bar{u} = 0$ (blue); $\tau_c = .0625$ and $\bar{u} = -.05$ (green); $\tau_c = .0625$ and $\bar{u} = -.1$ (red); $\tau_c = .25$ and $\bar{u} = -.1$ (cyan).

realistic damping.

6.5 Conclusions

In this chapter we have developed a new mathematical theory for the large-scale dynamics of precipitating regions in the tropical atmosphere. The estimates derived in Section 5.3 allow us to consider the limit of vanishing relaxation time (a useful and well-studied simplification) while being assured that the equations will remain well-behaved. We further idealize to the free wave problem (no forcing or dissipation) and study the propagation of "precipitation fronts," which mark the boundary between raining and dry regions in the tropics. These fronts have discontinuities in precipitation, vertical velocity, and derivatives of temperature and humidity. We study exact solutions for these fronts, which fall into three classes based on the speed of propagation: drying fronts, slow moistening fronts, and fast moistening fronts.

Both the slow moistening fronts and the fast moistening fronts violate Lax's stability criterion. However, numerical simulations indicate that all the fronts are realizable both at small relaxation time, and at more realistic finite relaxation times. The fronts converge to a steady state with the proper propagation speed following an adjustment period proportional to the convective relaxation time. We discuss the waves generated during this spin-up period as well. This behavior is robust varying both convective parameterization and grid spacing.

Finally we study steady forced-dissipative Walker cell solutions in Section 6.4. Although we prove in the limit of vanishing relaxation time that discontinuities in precipitation cannot occur in steady state with no barotropic wind, this is not guaranteed for simulations with mean wind. We then demonstrate numerically that precipitation fronts occur in the steady state with mean wind. That discontinuities are present in the steady forced-dissipative system provides further impetus to study these entities. Our theory for precipitation fronts provides the theoretical basis for study of the location and movement of precipitation regions.

Although interesting mathematically and presumably with physical analogs, this study of precipitation fronts remains remote from tropical phenomena of the real atmosphere or in full GCM's. Clearly a significant amount of work remains to connect this to more complex models. Extensions of this work are given in Pauluis et al. (2005), in which we study reflection and propagation of waves from dry regions to moist regions, and vice-versa, using the precipitation front framework.

We are additionally working on extending these concepts to intermediate complexity models. However, the GCM presented in Chapter 2 is not an appropriate context to do this, due to its unrealistic treatment of the tropics. Without a convection scheme, precipitation tends to go to the smallest possible scale, and simulations are somewhat a function of resolution. Therefore to develop the GCM into a model that is useful for study of tropical dynamics, we next develop a convection scheme for the moist GCM of the type used in this chapter.

Chapter 7

A Simplified Convection Scheme for the GCM

7.1 Introduction

The idealized moist GCM in the form presented in Chapter 2 is useful for study of the midlatitudes; however the tropics in the simulations of Chapters 3-4 are somewhat unrealistic. Fields such as the zonal wind, meridional overturning streamfunction, and precipitation are functions of resolution, and require a relatively high resolution to demonstrate any sort of convergence. With large-scale condensation as the only convection scheme, much of the tropical precipitation occurs within storms that are only a few gridpoints in size. These explode throughout the tropics and dominate the dynamics in this region, with strong low-level convergence surrounding precipitation events.

In order to study tropical dynamics in a more realistic setting that retains the simplicity of the idealized moist GCM, we have developed a simplified convection scheme in the style of Betts and Miller. Schemes of this type work on the basic principle that convection acts to relax the temperature and humidity to some post-convective reference profiles. As we demonstrate below, additional complexity is required in order to ensure conservation of enthalpy and to have some treatment of non-precipitating convection. We design our scheme in a mathematically and conceptually simple way in order to ensure reproducibility of results and ease of interpretation, but the methods we use for conservation and shallow convection have physical analogs as well.

We then use this convection scheme to study several prominent aspects of the zonally averaged tropical circulation: the mass and energy transports of the Hadley circulation; the strength and structure of the ITCZ; and zonal wind, temperature, and relative humidity profiles within the tropics and subtropics. We compare with other simplified convection schemes such as large-scale condensation (LSC) only and moist convective adjustment (MCA), and among various formulations and parameter sets within our "simplified Betts-Miller" (SBM) scheme. We attempt to make broad categorizations of the influence of convection and the formulation of convection schemes on large-scale tropical dynamics.

In this chapter we begin with a full description of the simplified Betts-Miller scheme in Section 7.2. We then evaluate the sensitivity to the shallow convection scheme in Section 7.3. We additionally compare with LSC only and MCA simulations within this section, and examine sensitivity to horizontal resolution for these various schemes. We evaluate the sensitivity to the parameters of the SBM scheme in Section 7.4, namely the convective relaxation time and reference profile relative humidity. We conclude in Section 7.5. Parts of this chapter appear in Frierson (2005).

7.2 A Description of the Simplified Betts-Miller Convection Scheme

Betts-Miller convection schemes (Betts (1986), Betts and Miller (1986), Janjic (1994)) take vertical profiles of temperature and humidity and calculate precipitation rates and changes in temperature and humidity by relaxing toward "post-convective equilibrium profiles." This calculation is performed through several steps: calculating reference profiles; determining whether there will be deep, shallow, or no convection; relaxing toward the reference states; correcting to satisfy enthalpy conservation; and performing shallow convection. We describe how our schemes treat these situations. None of the discussion below depends on the choice of reference profiles of temperature and humidity (T_{ref} and q_{ref}, respectively); therefore we describe this aspect of the scheme at the end of the section.

7.2.1 Convective Criteria and First Guess Relaxation

Before determining the convective criteria, we relax the temperature and humidity in the following way:

$$\delta q = -\frac{q - q_{ref}}{\tau_{SBM}} \quad (7.1)$$

$$\delta T = -\frac{T - T_{ref}}{\tau_{SBM}} \quad (7.2)$$

with τ_{SBM} the convective relaxation time, a parameter of the scheme. Then the "precipitation" due to drying and warming respectively are:

$$P_q = -\int_{p_0}^{p_{LZB}} \delta q dp/g \quad (7.3)$$

$$P_T = \int_{p_0}^{p_{LZB}} \frac{c_p}{L} \delta T dp/g \quad (7.4)$$

where the integrals range from the top to the bottom of the adjusted area (p_{LZB} and p_0). The simplest criteria for deep convection is that both P_T and P_q are positive. The former being positive is equivalent to $CAPE + CIN > 0$ if the temperature profile is a moist adiabat. The requirement $P_q > 0$ implies that there is more moisture in the column than in the reference profile. We now summarize different options that can be used under different regimes of P_T and P_q.

7.2.2 Deep convection: $P_T > 0, P_q > 0$

If both of the precipitation quantities P_T and P_q are positive, then we state that there is deep convection. However since these quantities will not be equal in general, we must devise a way to conserve enthalpy. The method utilized by Betts (1986) that we additionally use here is to change the reference profiles in such a manner that $P_T = P_q$. The simplest way to accomplish this is by changing the reference temperature by a uniform amount with height so that the changes in temperature (in enthalpy units) are opposite to the changes in humidity (in enthalpy units). The cooling that takes place in the lower troposphere when $P_q < P_T$ can be interpreted as roughly simulating the effect of downdrafts cooling at lower levels. An implication of the uniform change with height is that the reference profile is no longer an adiabat. This method of conserving enthalpy can be written as the following:

$$\Delta k = \frac{1}{\Delta p} \int_{p_0}^{p_{LZB}} -(c_p T + Lq - c_p T_{ref} - Lq_{ref}) dp \tag{7.5}$$

$$T_{ref2} = T_{ref} - \frac{\Delta k}{c_p} \tag{7.6}$$

where T_{ref2} is the corrected reference profile, which is then used in equation 7.2 to calculate temperature tendencies. When this method is utilized, the precipitation is solely dependent on the humidity relaxation, since the temperature is adjusted to match this. This implies that there is no sensitivity of precipitation to CAPE at all, except that it is used as a threshold for convection.

Clearly these are not the only methods of conserving enthalpy within the Betts-Miller framework. One could imagine instead adjusting the humidity reference profile and setting $P = P_T$. Further, one could construct a family of parameterizations by introducing a "precipitation efficiency" parameter which would specify the fraction of enthalpy deficit to be handled by changing the T_{ref} and the fraction to be handled by changing q_{ref}. However, the extreme case with $P = P_T$ is not useful, and, for simplicity and lacking theoretical or observational basis, we have not considered any cases with a precipitation efficiency as such. Additionally one can change relaxation times rather than reference profiles to conserve; however, all methods that change relaxation time are discontinuous when used with any useful shallow convection scheme.

7.2.3 Shallow Convection: $P_T > 0, P_q < 0$

If the precipitation after the enthalpy conservation correction is negative, we switch to the shallow convection scheme (if the enthalpy conservation scheme given in equations 7.5-7.6 is used, this amounts to $P_T > 0, P_q < 0$). In order to make this continuous in precipitation with the scheme that changes the temperature reference profile to conserve enthalpy, we make the net precipitation zero in this limit. For reference, the original Betts-Miller scheme specifies a shallow cloud top height and then performs a relaxation to mixing-line structures up to that height. Their shallow convection scheme is additionally called if the level of zero buoyancy is below a fixed threshold level. Since we wish to run this scheme over a large range of climates, and do not expect the current climate shallow cloud top height to be a robust value over different climates, we attempt more physically based shallow convection schemes. We have constructed three methods to perform this adjustment, which we describe here and test in the next section.

The simplest option for shallow convection is not to adjust at all under these conditions (i.e., $\delta q = 0, \delta T = 0$). This introduces a certain amount of discontinuity when matched against any of the schemes for enthalpy conservation above, but this is the limit against which we test the other shallow convection schemes.

The first nontrivial shallow scheme that we propose is one that lowers the depth of shallow convection. This scheme finds the deepest height for which there is enough moisture for the precipitation to be identically equal to zero, i.e., the integral in equation 3 above is zero. A height will exist for all cases where the boundary layer has enough moisture. The transition as the precipitation goes to zero will be continuous in all cases where the upper troposphere is being moistened. Then for the temperature equation, we adjust the temperature within the same layer, changing the reference profile by a constant amount with height, Δk as calculated below to ensure enthalpy conservation. In this scheme the parcels do not reach their level of zero buoyancy, so we are implicitly assuming some entrainment. This can be expressed as the following set of equations:

$$
\begin{aligned}
0 &= \int_{p_0}^{p_{shall}} \left(-\frac{q - q_{ref}}{\tau_{SBM}}\right) dp & (7.7)\\
\Delta k &= \frac{1}{\Delta p} \int_{p_0}^{p_{shall}} -(c_p T + Lq - c_p T_{ref} - Lq_{ref}) dp & (7.8)\\
T_{ref2} &= T_{ref} - \frac{\Delta k}{c_p},\ p_{shall} < p < p_0 & (7.9)
\end{aligned}
$$

where p_{shall} is selected to satisfy equation 7.7. Equations 7.1 and 7.2 (with T_{ref2} used in the latter) are then used in the range $p_{shall} < p < p_0$ to calculate humidity and temperature tendencies. We refer to this method as the "shallower" shallow convection scheme.

Another scheme that we propose involves changing the reference profiles for both temperature and humidity so the precipitation is zero. This scheme does not change the depth of shallow convection, and instead simply changes the reference profile of humidity by a uniform fraction with height all the way up to the level of zero buoyancy, to make the precipitation zero. The temperature reference profile is changed in the usual manner, adjusting by a uniform amount with height so that its predicted precipitation is zero. This scheme can be written as:

$$\begin{aligned}
\Delta q &= \int_{p_0}^{p_{LZB}} (q - q_{ref})dp && (7.10)\\
Q_{ref} &= \int_{p_0}^{p_{LZB}} (-q_{ref})dp && (7.11)\\
f_q &= 1 - \frac{\Delta q}{Q_{ref}} && (7.12)\\
q_{ref2} &= f_q q_{ref} && (7.13)\\
\Delta T &= \frac{1}{\Delta p}\int_{p_0}^{p_{LZB}} -(T - T_{ref})dp && (7.14)\\
T_{ref2} &= T_{ref} - \Delta T && (7.15)
\end{aligned}$$

Equations 7.1 and 7.2, using the adjusted reference profiles q_{ref2} and T_{ref2}, then give the tendencies for humidity and temperature. We denote this shallow scheme by "qref," due to the fact that the humidity profile is adjusted.

7.2.4 Reference Profiles

For our temperature reference profile, we use the virtual pseudoadiabat for our temperature profile, meaning water vapor of the parcel and the environment are taken into account in the calculation of buoyancy, but the condensate immediately falls out. For the humidity profile, we specify a fixed relative humidity relative to this calculated temperature structure; this is the method utilized by Neelin and Yu (1994). This introduces the second parameter of the scheme, RH_{SBM}. Adjustment occurs from the surface to the level of zero buoyancy of a parcel lifted from the lowest model level. All of the discussion presented above is valid for any choice of reference profile.

7.3 Sensitivity to Shallow Convection Scheme

7.3.1 Model Setup

Here our model setup is identical to that given in Chapters 3 and 4 with the addition of the convection scheme and one additional change. In order to obtain a more realistic energy balance at the surface and strength of the hydrologic cycle, we specify a solar heating within the atmosphere. This is calculated by specifying optical depths for short wave radiation τ_{SW} within the atmosphere. Then we solve

$$\frac{dD_{SW}}{d\tau_{SW}} = -D_{SW} \tag{7.16}$$

with boundary condition $D(\tau = 0) = Q_{solar}$, and

$$Q_{SW} = \frac{1}{c_p \rho} \frac{\partial D_{SW}}{\partial z} \tag{7.17}$$

The latter is applied as a source term in the temperature equation. Optical depths are specified as

$$\tau_{SW} = \tau_{SW0} (\frac{p}{p_0})^4 \tag{7.18}$$

The parameter τ_{SW0} is set to a value of .2 which implies that 18% of the TOA SW radiation is absorbed within the atmosphere. We then specify an albedo of .38 at the surface for all latitudes, which ensures that 51% of Q_{solar} is absorbed at the surface, and 31% of Q_{solar} is reflected to space. This provides an energy balance and hydrologic cycle strength that is more in accordance with observations.

The simulations below, unless otherwise noted, are run at T42 resolution with 25 vertical levels (spaced the same as in 3 and 4). We integrate for 1800 days, with the last 1440 days used for averaging. Time means are calculated using averages over each model time step, and spectra are calculated using instantaneous values sampled once per day. The control simulation with the SBM scheme uses the "shallower" shallow convection scheme, and has the SBM parameters $\tau_{SBM} = 2h$ and $RH_{SBM} = .7$.

7.3.2 Comparison with Large Scale Condensation Only and Moist Convective Adjustment Simulations, and among Different Shallow Convection Schemes

We begin by examining snapshots of precipitation for a simulation with LSC only, and the SBM scheme with the shallower scheme, the qref scheme, and no shallow convection scheme, shown in Figure 7.1. The LSC only simulations have large amounts of precipitation at small scales, of the order of a few gridpoints. Much of the tropics and subtropics are without precipitation at any given instance, although tropical storm-like disturbances can be seen propagating sparsely throughout the subtropics and into midlatitudes. Simulations with MCA (not shown) are qualitatively indistinguishable from the LSC only snapshot. When the SBM scheme is used but is integrated without a shallow convection scheme, the snapshot resembles the LSC only case to a large extent. In contrast, when either the shallower or the qref shallow convection schemes are used, tropical precipitation ceases to occur at small scales only, and is instead concentrated in more diffuse, zonally oriented bands. A larger fraction of the tropics and subtropics is precipitating at any time in these simulations, but there remain dry regions in much of the subtropics and some of the deep tropics. Tropical storms again propagate in the subtropics, but in a more diffuse manner than the LSC simulations. The shallower and qref simulations are nearly indistinguishable in this field, with tropical precipitation occurring at a slightly smaller scale when the shallower scheme is used.

As a more quantitative examination of typical sizes of convection in the tropics, we plot the spectrum for the vertical velocity ($\omega = \frac{Dp}{Dt}$) at the equator in these simula-

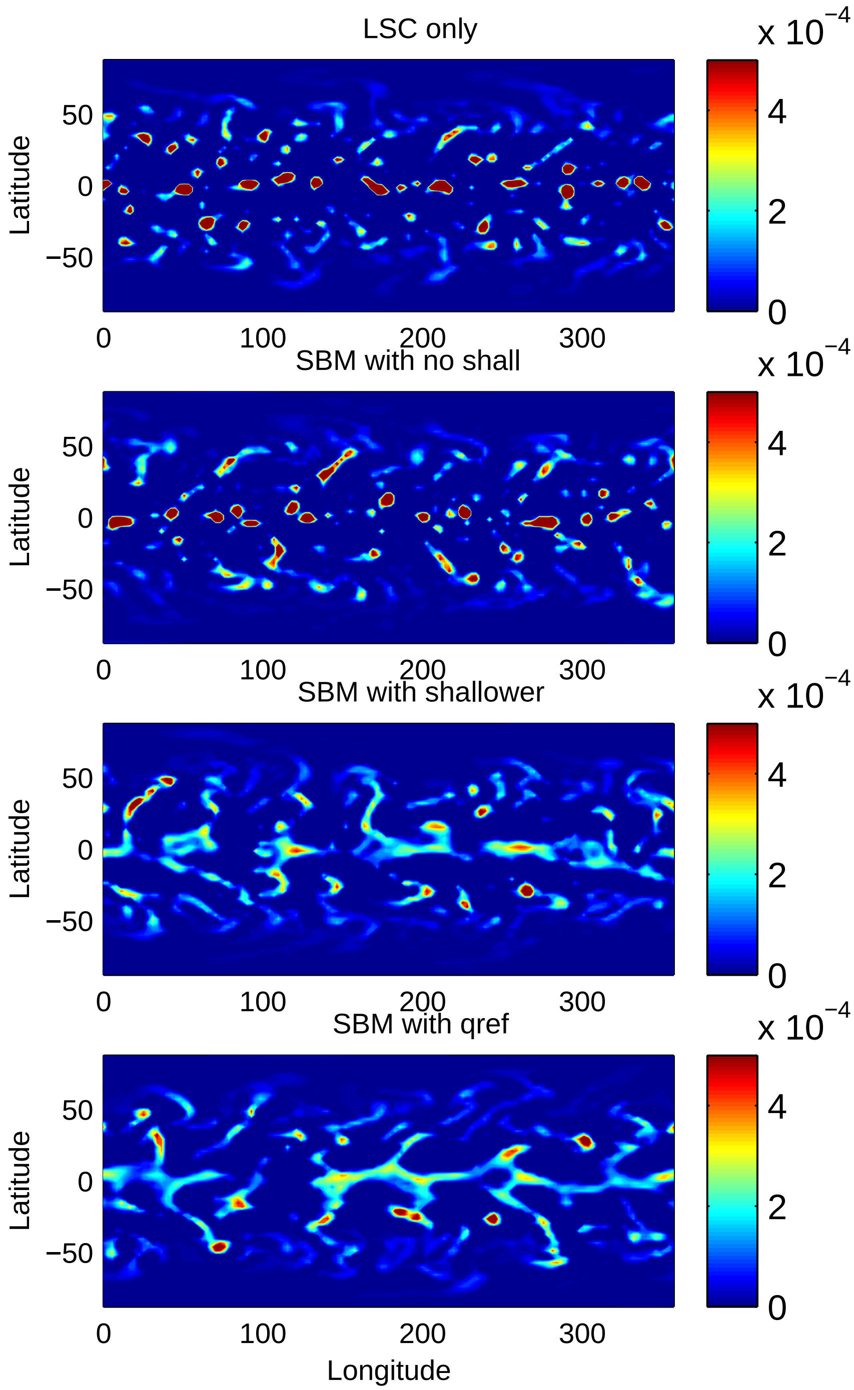

Figure 7.1: Instantaneous precipitation for (top to bottom): LSC only; the SBM scheme with no shallow convection scheme; the SBM scheme with the shallower shallow convection scheme; and the SBM scheme with the qref shallow convection scheme.

tions, presented in Figure 7.2. The MCA and LSC simulations have the most variance of ω, with the SBM with no shallow convection intermediate, and the two simulations with shallow convection last. There is a clear spectral peak at wavenumber 2 for the shallower and qref SBM simulations, implying large-scale organization of convection in these cases. The shallower simulation has slightly more variance at smaller scales as compared with qref. In contrast, for the LSC only, MCA, and SBM with no convection scheme the spectrum is much less peaked, and significant power exists out to small scales. Much of the spectrum occurs near the gridscale for these simulations, suggesting there will be some sensitivity to horizontal resolution (which we analyze in more detail in Section 7.3.4). Evidently without the use of shallow convection, the relaxed adjustment of the SBM scheme is unable to prevent convection occurring at scales near the gridscale.

To evaluate the effect of shallow convection on the Hadley circulation system, we next plot the meridional moist static energy flux by the mean flow for the different shallow schemes in Figure 7.3. Again the two SBM simulations with shallow convection are similar, as are the LSC and MCA simulations, and the SBM with no shallow convection falls somewhat in between these two groups. The LSC only and MCA simulations both have areas of equatorward transport in the deep tropics, and achieve significantly less poleward transport by the mean flow in general. The equatorward transport in the LSC and MCA cases is offset by strong eddy fluxes of moisture in the deep tropics, implying smaller differences in the total flux of moist static energy. Both of the SBM schemes with shallow convection give similar fluxes, with poleward fluxes at all latitudes within the Hadley cell, and achieving maxima of approximately 1.5-1.6 PW at latitudes between 15 and 19 degrees. The SBM scheme with no shallow convection has reduced energy fluxes within the deep tropics, but never becomes equatorward. The profile essentially matches onto the other SBM scheme fluxes poleward of the maximum flux. Equatorial precipitation values (in W/m^2) and maximum

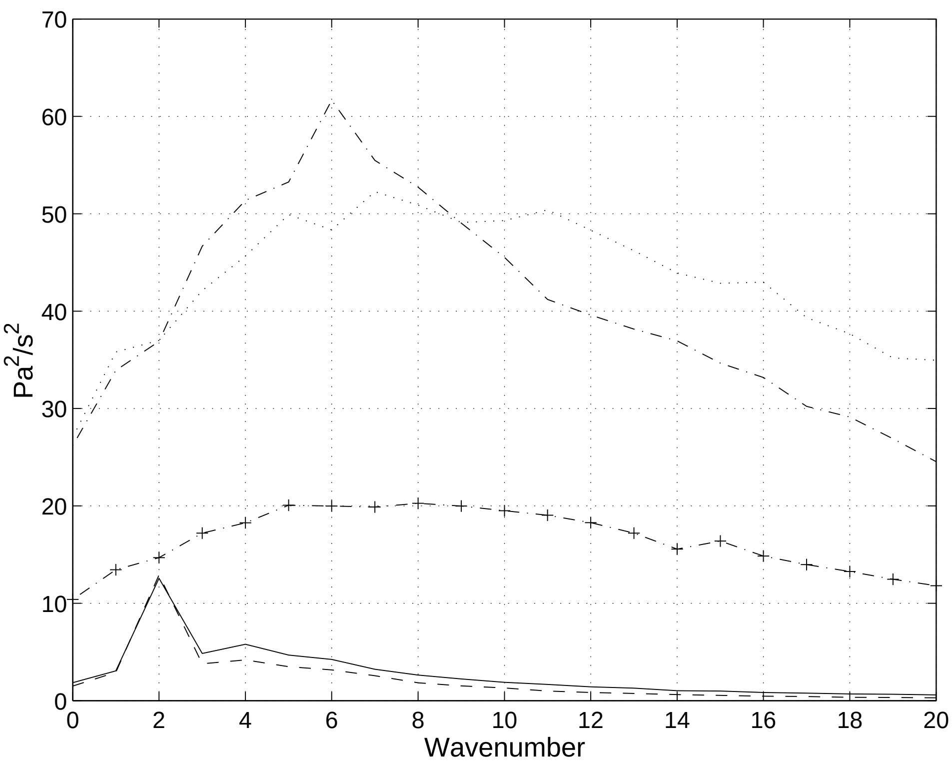

Figure 7.2: Spectrum for vertical velocity (ω) at 560 mbar for the control SBM scheme with the "shallower" shallow convection scheme (solid), the SBM scheme with qref (dashed), the SBM scheme with no shallow convection (dash-dot with +'s), the LSC only simulation (dotted), and MCA (dash-dot).

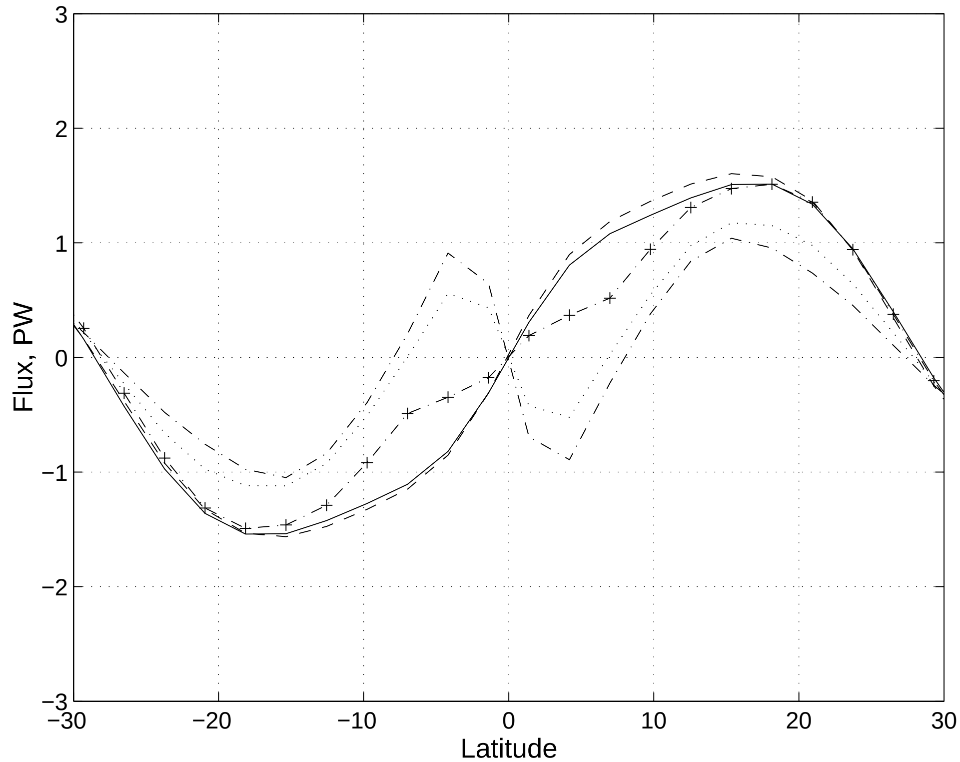

Figure 7.3: Vertically integrated meridional moist static energy flux by the mean flow for the control SBM scheme with the shallower shallow convection scheme (solid), the SBM scheme with qref (dashed), the SBM scheme with no shallow convection (dash-dot with +'s), LSC only (dotted), and MCA (dash-dot).

Hadley circulation mass transport (in $10^9 kg/s$) are given in Table 7.1. The precipitation distribution achieves its global maximum at the equator in all these cases. The agreement between the two SBM schemes with shallow convection is remarkable, suggesting the shallow convection scheme has little effect on the behavior of the Hadley circulation system, as long as some shallow convection is used. The Hadley circulation is stronger than observations in all cases, a fact we understand from the lack of ocean heat transport in the simulations (either explicit, or implied from fixed SST boundary conditions). Again the SBM scheme with no shallow convection is intermediate between the SBM schemes with shallow convection, with weaker Hadley circulation and equatorial precipitation, and the LSC and MCA simulations.

It is somewhat remarkable that despite a 50% stronger Hadley circulation, the

Simulation	P(eq)	max(Had)
SBM w/ shallower	291	184
SBM w/ qref	285	183
SBM w/ no shallow	397	227
LSC	438	277
MCA	470	273

Table 7.1: Precipitation at the equator (W/m^2) and maximum meridional overturning streamfunction ($10^9 kg/s$) for the simulations varying convection scheme and shallow convection scheme.

LSC and MCA simulations still transport significantly less energy poleward. The appropriate quantity to consider here is the "gross moist stability" (Neelin and Held, 1987), which we define here as the amount of energy transported per unit mass transport:

$$\Delta m = \frac{\int_0^{p_s} \bar{v}\bar{m} dp}{\int_{p_m}^{p_s} \bar{v} dp}, \tag{7.19}$$

where Δm is the gross moist stability, m is the moist static energy, p_s is the surface pressure, and p_m is some midtropospheric level (defined so that the equatorward mass flux occurs mostly below this level, and the poleward mass flux occurs above). This quantity is plotted for the SBM case with shallower shallow convection, the SBM case with no shallow convection, and the LSC only case in Figure 7.4. The gross moist stability for all cases increases sharply away from the equator to the edge of the Hadley circulation where this quantity becomes ill-defined. However the values at the equator are significantly different for the three cases: approximately 6 K, 2 K, and -6 K for the SBM with shallower shallow convection, SBM with no shallow convection, and LSC only, respectively. In the shallower simulation, the gross moist stability is large enough at all latitudes that the mean flow can transport enough energy poleward with a modest strength Hadley circulation; the convection scheme has provided a stabilizing influence over the deep tropics. In the LSC only case, on the other hand, the gross moist stability is negative out to approximately 8 degrees, so even an extremely strong Hadley circulation cannot produce energy fluxes to flatten tropical temperatures. In this case, there is strong instability in the time mean, and small scale eddies flux large amounts of latent heat poleward. Despite the increased eddy moisture divergence at the equator in the LSC only case, the precipitation increases by 50% at the equator due to the significantly increased moisture convergence by the stronger Hadley cell. In the theory of Satoh (1994), the gross moist stability cannot exert an influence on the Hadley circulation because the dry subtropics provide an additional constraint on the mass transport. Here, in contrast, mass and energy balance are satisfied with changes in precipitation in the subtropical regions: precipitation is reduced at 15 degrees from 90 W/m^2 in the shallower case and 77 W/m^2 in the SBM with no shallow case, and 57 W/m^2 in the LSC only case, and allow the Hadley circulation to change significantly.

7.3.3 Ability to Build Up Convectively Available Potential Energy

To further explain the differences in these convection schemes, we next examine time series of precipitation and CAPE at a fixed gridpoint on the equator. This is displayed for 50 day time intervals for the LSC only simulation, the MCA simulation, and SBM simulations with no shallow scheme, the shallower scheme, and the qref scheme in Figure 7.5. A first notable point is that the values of CAPE are significantly larger in the LSC and MCA cases, regularly attaining values several times larger than the other cases. The atmosphere is significantly less conditionally unstable for the SBM cases with shallow convection, with typical CAPE values of 500 J/kg. For the qref case in particular, CAPE does not vary in time much either. In the shallower case, CAPE increases relatively rapidly when the column is not precipitating, and this is

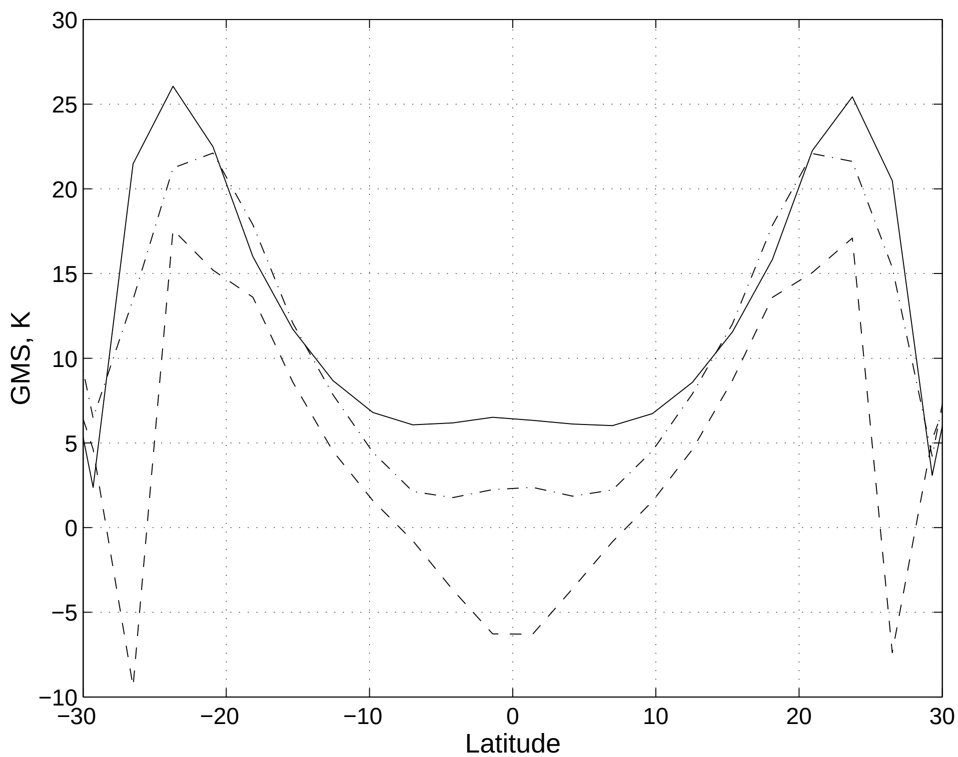

Figure 7.4: "Gross moist stability" (see text for definition) for the control SBM scheme with the shallower shallow convection scheme (solid), the SBM scheme with no shallow convection (dash-dot), and LSC only (dashed).

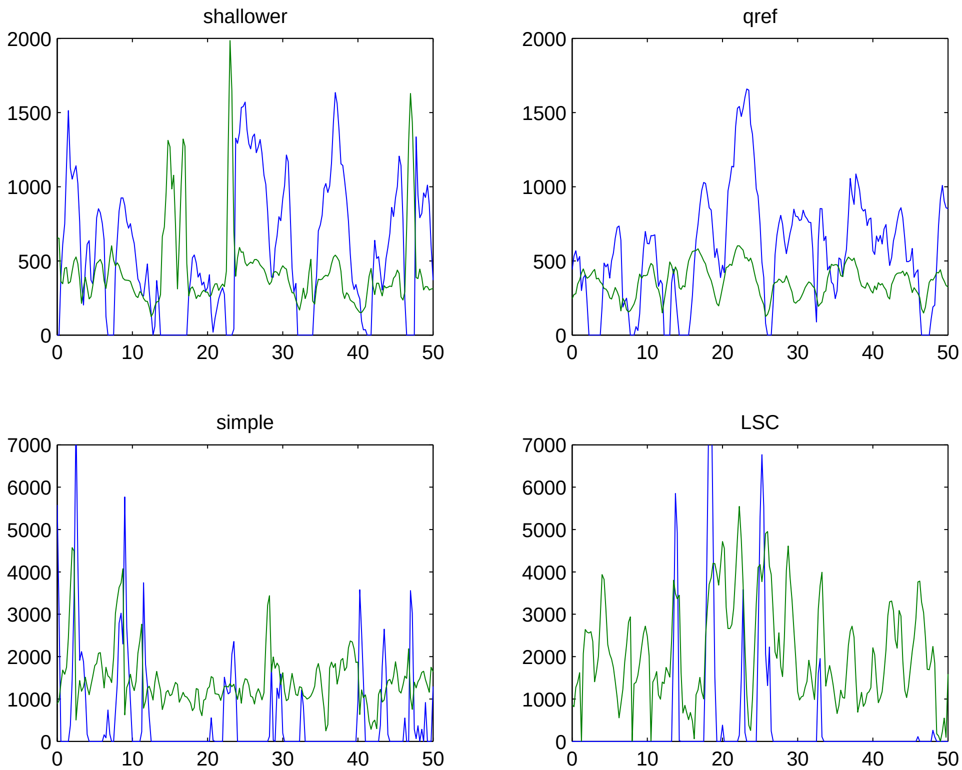

Figure 7.5: Time series of CAPE (green) and precipitation (blue) at a fixed location on the equator for the SBM scheme with "shallower" shallow convection, SBM with "qref" shallow convection, SBM with no shallow convection, and LSC only. Note the different scales in the upper and lower plots. The units for CAPE are J/kg, and the scales refer to this quantity. The precipitation in units of W/m^2 has been multiplied by 2 for plotting purposes.

then dissipated upon onset of deep convection. Evidently with the lower depth of shallow convection in the shallower scheme, conditional instability can be built up more easily when deep convection is not occurring. The variations of CAPE in the shallower case are small compared to those in the SBM simulations with no shallow convection, where typical values of CAPE are over twice as large, and CAPE is often built up to over 4000 J/kg and rapidly released in large precipitation events.

It appears that the ability to build up and rapidly release CAPE is a key classification of convection schemes that greatly affects the tropical general circulation. The LSC only scheme and MCA can both build up significant CAPE because these schemes require complete saturation of the gridbox to trigger convection. The SBM scheme with no shallow convection still has an abrupt trigger, that there is sufficient humidity as compared with the reference profile, so CAPE can still be built up and rapidly released. However since the requirements for convection are less severe than in the LSC or MCA schemes (as only 70% of the saturated humidity of the reference profile is needed to convect), the amount of CAPE that can be built up is less in this case. In the cases with shallow convection, the schemes are more effective at preventing large amounts of CAPE from building up, especially in the case of the qref shallow scheme.

If the ability to build up CAPE is relevant for convection, one would expect the SBM schemes to diverge even more as the criteria for deep convection becomes more difficult to satisfy. We provide a simple test of this by examining simulations with a larger value of RH_{SBM}. In Figure 7.6 we plot the Hadley circulation moist static energy flux for the SBM scheme with no shallow scheme, the shallower scheme, and the qref scheme with $RH_{SBM} = .8$. The simulation with no shallow scheme in this case develops a region of equatorward transport, and has decreased fluxes everywhere, similar to the LSC or MCA simulations. The shallower simulation, which was found to allow larger CAPE buildup, has moist static energy fluxes slightly decreased equatorward of 20 degrees. The qref simulation is only slightly affected. This is in accordance with our expectations from the time series of CAPE in Figure 7.5.

7.3.4 Sensitivity to Horizontal Resolution

We now investigate sensitivity to horizontal resolution in the LSC only case and the control SBM case (with shallower shallow convection) by comparing with simulations at T21 and T85 resolution, all with 25 vertical levels. We first examine the vertically integrated meridional moist static energy transport by the mean flow, plotted in Fig-

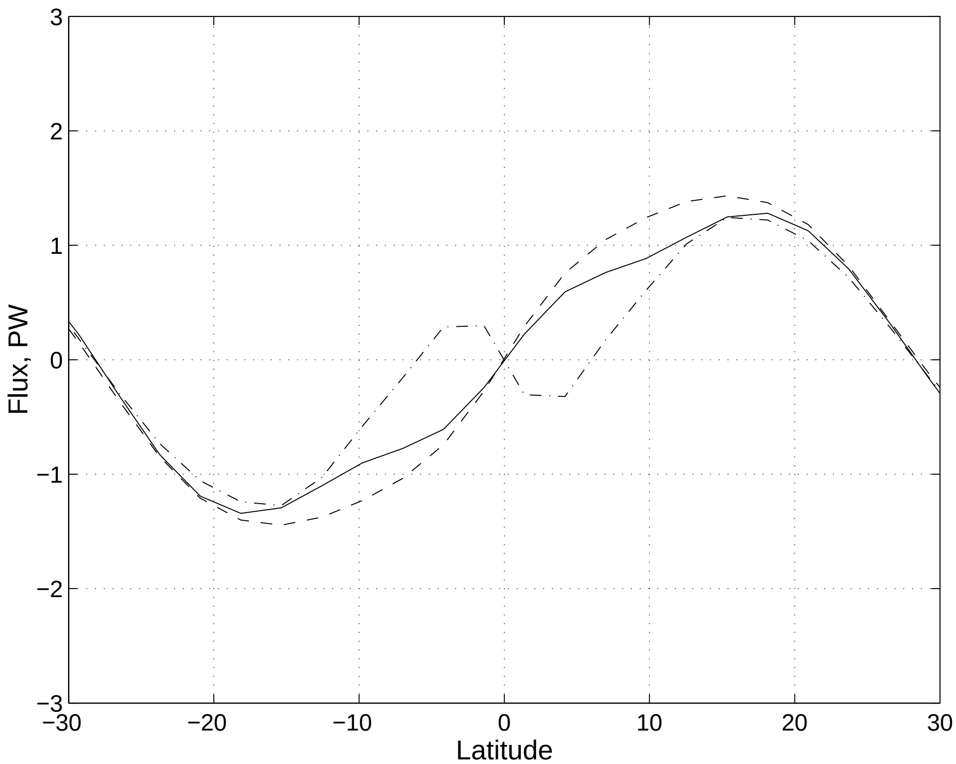

Figure 7.6: Vertically integrated meridional moist static energy flux by the mean flow for the SBM scheme with $RH_{SBM} = .8$ and the shallower scheme (solid), the qref scheme (dashed), and no shallow convection scheme (dotted).

ure 7.7. The LSC only case shows significant change with resolution up to T85 (in the simulations of Frierson et al. (2005a) we found that similar simulations at T85 resolution were essentially converged as compared to T170). The region of equatorward transport by the mean flow in the LSC cases is balanced by strong poleward eddy moisture fluxes, which cause the net MSE transport (mean + eddy) to be similar in all cases. The equatorward transport by the mean flow decreases with resolution, as do the eddy moisture fluxes. In contrast, the SBM scheme exhibits only minor change in resolution from T42 to T85 (although the T21 case is unresolved). The SBM convection scheme with shallow convection provides significantly improved convergence with resolution within the tropics for this field. The equatorial precipitation and maximum Hadley circulation transport are given in Table 7.2. These fields both exhibit some dependence on resolution for the LSC simulations as well as the SBM scheme up to resolutions of T85.

Simulation	P(eq)	max(Had)
SBM, T85	314	197
SBM, T42	291	184
SBM, T21	193	124
LSC, T85	482	268
LSC, T42	438	277
LSC, T21	214	137

Table 7.2: Precipitation at the equator (W/m^2) and maximum meridional overturning streamfunction ($10^9 kg/s$) for the simulations varying resolution.

We now consider the resolution dependence of the zonal wind, plotted in Figure 7.8 for the control SBM simulations and Figure 7.9 for the LSC only simulations. At T21 resolution, both simulations exhibit significant equatorial superrotation. Surface zonal wind profiles are much more diffuse at T21 with both schemes as well,

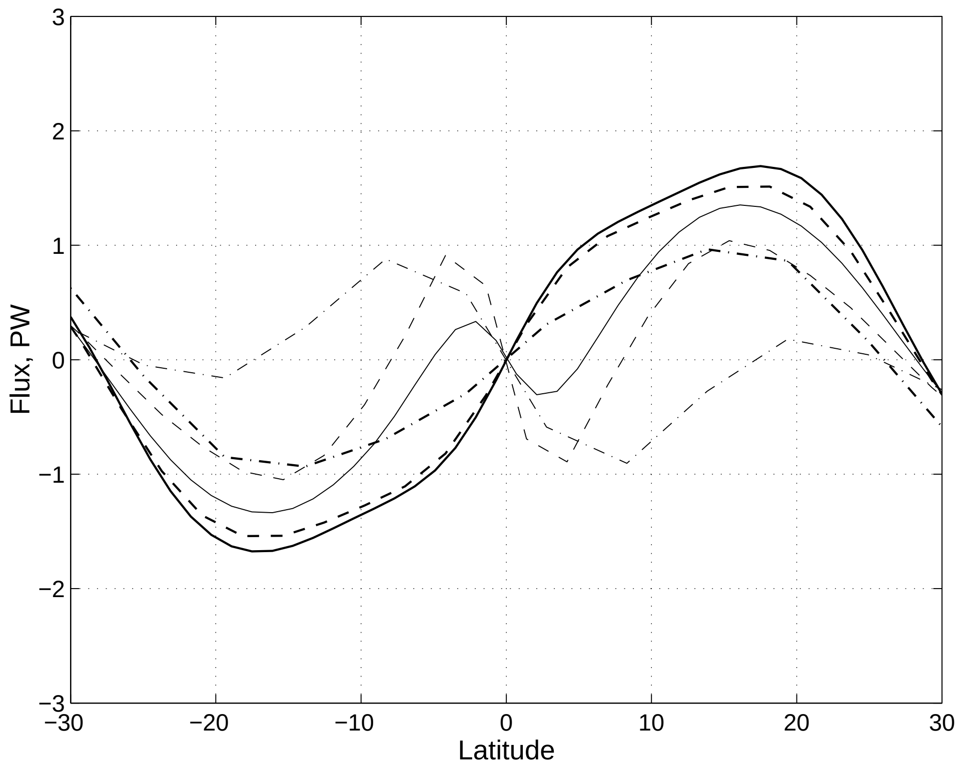

Figure 7.7: Vertically integrated meridional moist static energy flux by the mean flow for the control SBM scheme (dark lines) and the LSC only simulations (light lines) at T85 (solid), T42 (dashed), and T21 (dash-dot).

attaining minima of only -3.1 m/s and -5.7 m/s for the LSC only case and SBM case, respectively, as compared to -8.5 m/s and -9.7 m/s respectively at T85. With the SBM scheme, the superrotation is eliminated at T42 resolution, and the profile at T85 is essentially identical to the T42 simulation. By contrast, with the LSC only simulation superrotation weakens as resolution is increased, but remains even at T85. Similar simulations in Frierson et al. (2005a) have equatorial superrotation eliminated at T170 resolution, but existing at resolutions below this. These results give us confidence that tropical circulations with the SBM can be adequately studied at horizontal resolutions of T42. However, resolutions of T21 appear to be inadequate to reproduce most aspects of tropical climate. Without a convection scheme, a higher resolution (of T85 or higher) is required to obtain convergence of some tropical climatic variables.

7.4 Sensitivity to Simplified Betts-Miller Scheme Parameters

7.4.1 Sensitivity to Convective Relaxation Time

The SBM scheme has only two parameters after the choice of shallow convection scheme: τ_{SBM} and RH_{SBM}. We first examine sensitivity to the relaxation time τ_{SBM} with $RH_{SBM} = .7$ and the shallower shallow convection scheme, as in the control case in the above. The Hadley cell moist static energy fluxes are plotted for $\tau_{SBM} = 1h, 2h, 4h, 8h$ and $16h$ in Figure 7.10. This field changes remarkably little with relaxation time: the cases with $\tau_{SBM} = 4h$ or less are all almost identical, while the $\tau_{SBM} = 8h$ simulation exhibits a small decrease in flux from latitudes of 4 and 12 degrees. The $\tau_{SBM} = 16h$ simulation diverges somewhat from the other four simulations, with flux profiles more similar to the LSC only cases. Equatorial

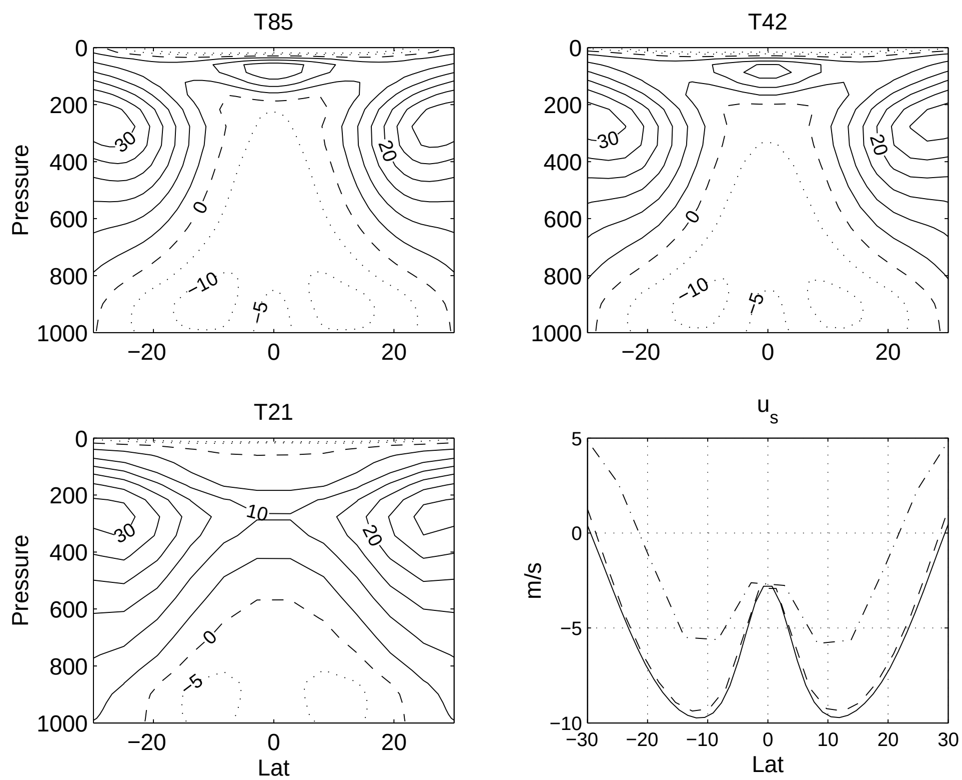

Figure 7.8: Zonal winds for the control SBM scheme at T85 (top left), T42 (top right), and T21 (bottom left); and surface zonal winds (bottom right) at T85 (solid), T42 (dashed) and T21 (dash-dot).

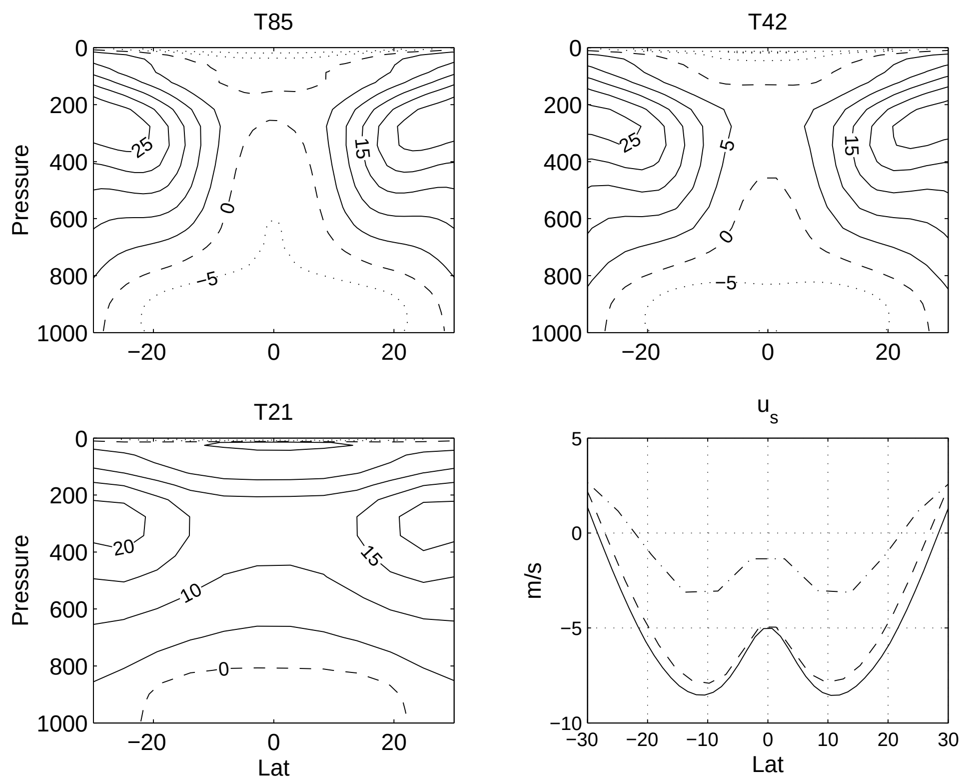

Figure 7.9: Zonal winds for the LSC only simulations at T85 (top left), T42 (top right), and T21 (bottom left); and surface zonal winds (bottom right) at T85 (solid), T42 (dashed) and T21 (dash-dot).

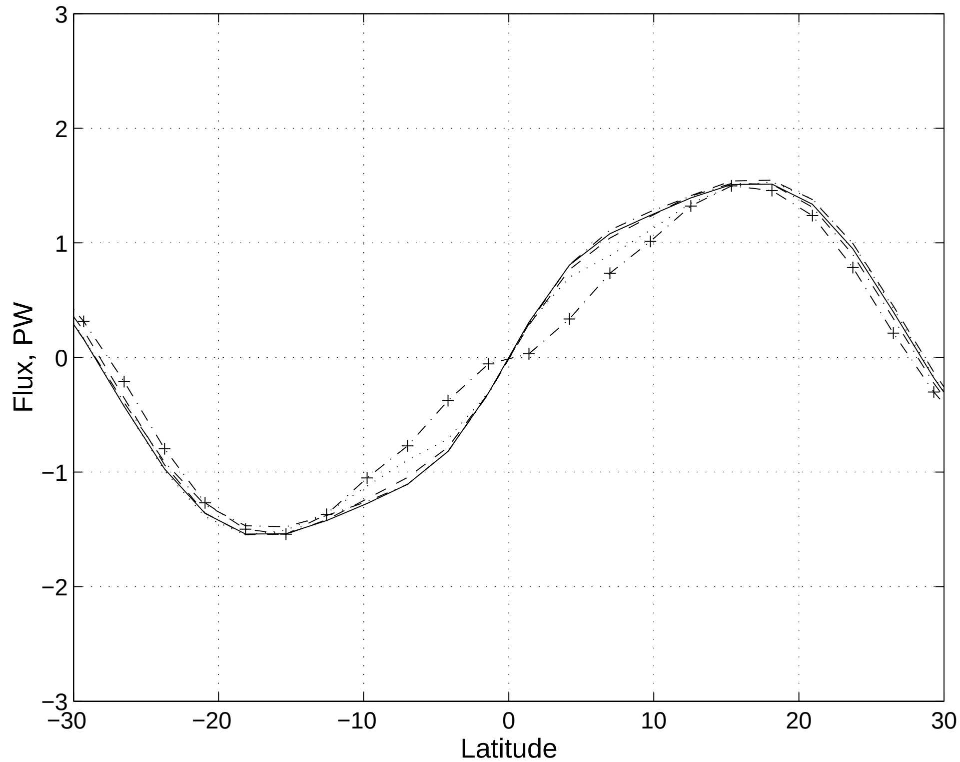

Figure 7.10: Vertically integrated meridional moist static energy flux by the mean flow for the control SBM scheme ($\tau_{SBM} = 2h$, $RH_{SBM} = .7$) (solid), $\tau_{SBM} = 4h$ (dashed), $\tau_{SBM} = 1h$ (dash-dot), $\tau_{SBM} = 8h$ (dotted), and $\tau_{SBM} = 16h$ (dash-dot with +'s).

precipitation distributions and maximum Hadley circulation mass transport are given in Table 7.3; these show a similar insensitivity to relaxation time in all cases except the $\tau_{SBM} = 16h$ simulation, which exhibits a 62% increase in precipitation and a 31% increase in Hadley circulation strength.

We explain the similarities and differences of the simulations varying relaxation time by examining the precipitation term (using equations 7.1 and 7.3):

$$P = \frac{\bar{q} - \bar{q}_{ref}}{\tau_{SBM}} \tag{7.20}$$

where we use the overbar to denote a vertical integral over the adjusted region, i.e., $\bar{\xi} = \int_{p_0}^{p_{LZB}} \xi dp/g$. The expression 7.20 is exact since $P = P_q$ using our energy conservation

Simulation	P(eq)	max(Had)
$\tau_{SBM} = 1h$	285	182
$\tau_{SBM} = 2h$	291	184
$\tau_{SBM} = 4h$	295	186
$\tau_{SBM} = 8h$	283	185
$\tau_{SBM} = 16h$	459	242

Table 7.3: Precipitation at the equator (W/m^2) and maximum meridional overturning streamfunction ($10^9 kg/s$) for the simulations varying convective relaxation time τ_{SBM}.

scheme. There is a similar expression writing the precipitation in terms of $\bar{T}$ and $\bar{T}_{ref}$; however this involves the energy correction and thus the humidity relaxation as well. We focus first on the humidity relaxation. Our results suggest that as τ_{SBM} is varied over a wide range, the precipitation P stays constant, therefore pushing the vertical averaged humidity away from the reference profile according to

$$\bar{q} = \bar{q}_{ref} + \tau_{SBM} P \tag{7.21}$$

A similar adjustment of humidity/temperature rather than precipitation occurs in simple models which use Betts-Miller-type convective parameterizations, e.g., Frierson et al. (2004). We plot the zonal and time mean relative humidity distribution for four of the simulations varying relaxation time in Figure 7.11. This increases significantly as τ_{SBM} is increased, both within the ITCZ and in the subtropics. As long as the precipitation is the same, this change in relative humidity has little effect because the longwave optical depths are fixed. With the short relaxation time of $1h$, the deep tropics are kept very close to 70% relative humidity. With $\tau_{SBM} = 8h$, on the other hand, ITCZ relative humidities exceed 95% in the midtroposphere, and typical subtropical values are around 55%. With $\tau_{SBM} = 16h$ (not shown), the relative

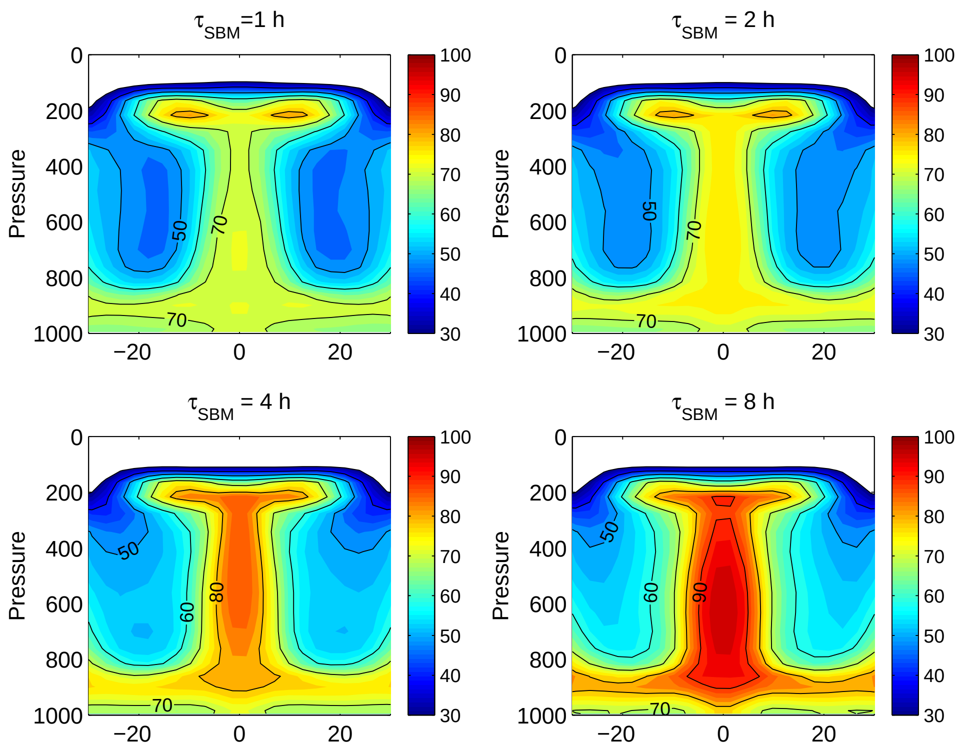

Figure 7.11: Relative humidity distribution for the control SBM scheme (top right), with $\tau_{SBM} = 1h$ (top left), $\tau_{SBM} = 4h$ (bottom left), and $\tau_{SBM} = 8h$ (bottom right).

humidity is similar to $\tau_{SBM} = 8h$. Significant large scale precipitation occurs in the deep tropics in the 16 h simulation: over 67% of the equatorial precipitation in the 16 h case is large scale, as compared to only 7% large scale for the 8 h case and zero in the other cases. It is thus not surprising that the $\tau_{SBM} = 16h$ case takes on many of the properties of the LSC only simulations (e.g., increased Hadley circulation and equatorial precipitation). The large change in relative humidity as τ_{SBM} varies over a wide range has little effect on the Hadley circulation system unless significant amounts of large scale condensation can occur.

A few comments are necessary to compare with the results of Fang and Tung (1997); in this study the authors vary the thermal relaxation time for Newtonian cooling in an axisymmetric model and find a large sensitivity to this parameter. With the Newtonian cooling parameterization the heating rate is proportional to $1/\tau$, assuming a temperature structure consistent with angular momentum conservation within the cell. Therefore, a significantly stronger Hadley circulation is required to transport enough heat to flatten temperatures as the relaxation time is decreased. By contrast, changing the convective relaxation time in our model changes the heating only minimally, and no additional meridional fluxes are required to keep the temperatures/zonal winds the same.

A value of $\tau_{SBM} = 16h$ is suggested by Bretherton et al. (2004); using this with $RH_{SBM} = .7$ is ineffective in preventing large scale condensation from occurring. We investigate what value of RH_{SBM} is required to use $\tau_{SBM} = 16h$ without significant large-scale precipitation in Section 7.4.3, after first examining the sensitivity to the RH_{SBM} parameter.

7.4.2 Sensitivity to Reference Profile Relative Humidity

We next present a brief treatment of the sensitivity to RH_{SBM}, the relative humidity of the reference profile to which we relax. Unfortunately the dependence on this parameter is significantly more complicated than the τ_{SBM} sensitivity. A first aspect of this dependence we consider is the relative humidity distribution, plotted in Figure 7.12 for $\tau_{SBM} = 2h$ and $RH_{SBM} = .8, .7, .6,$ and $.5$. The ITCZ humidity is fixed at a slightly larger value than RH_{SBM} in each case, as discussed in the previous section. The subtropical humidity varies as well with this parameter, although somewhat less than the ITCZ values.

We next plot the moist static energy flux by the Hadley circulation for the RH_{SBM} experiments in Figure 7.13. The flux gradually increases as RH_{SBM} is decreased; this is nearly identically compensated by decreased eddy moisture fluxes in these cases. It is unclear whether the reduction in eddy moisture fluxes can be considered to be the cause of the changes in Hadley circulation energy transports. The Hadley circulation is relatively insensitive to changes in RH_{SBM}, but the precipitation distribution is

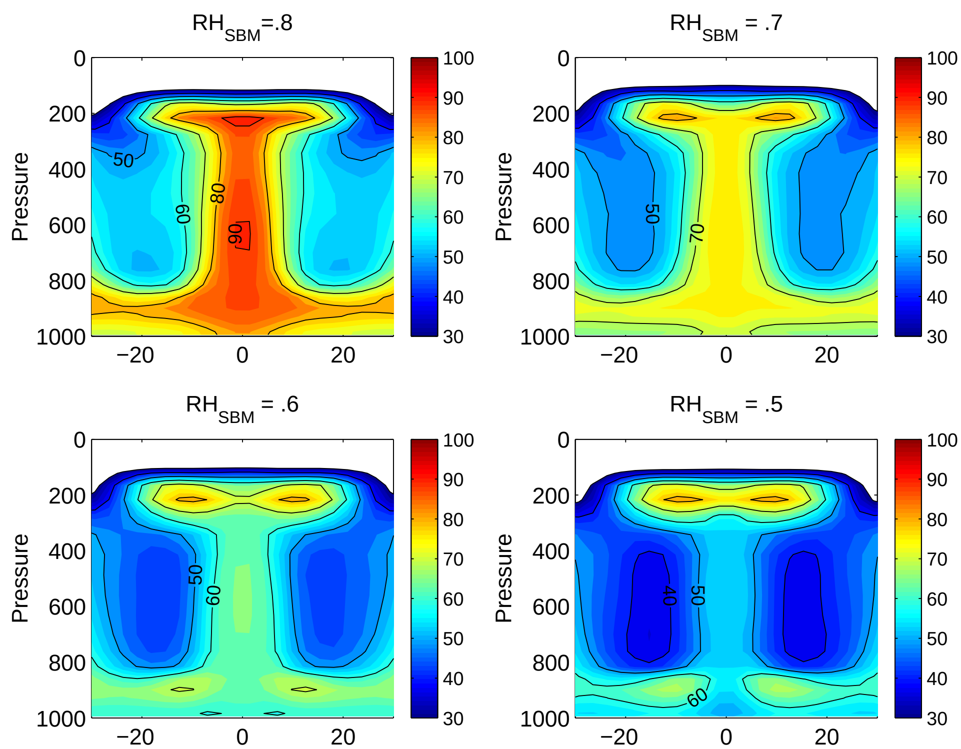

Figure 7.12: Relative humidity distribution for the control SBM scheme (top right), with $RH_{SBM} = .8$ (top left), $RH_{SBM} = .6$ (bottom left), and $RH_{SBM} = .5$ (bottom right).

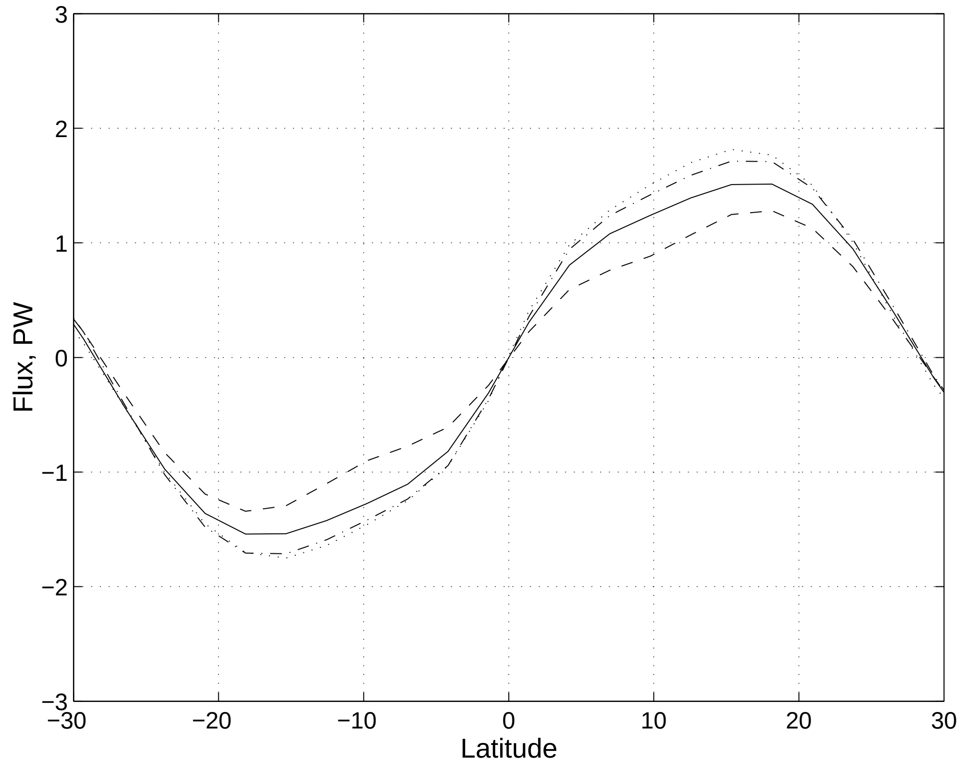

Figure 7.13: Vertically integrated meridional moist static energy flux by the mean flow for the control SBM scheme (solid), with $RH_{SBM} = .8$ (dashed), $RH_{SBM} = .6$ (dash-dot), and $RH_{SBM} = .5$ (dotted).

somewhat sensitive (Table 7.4). There is however non-uniform behavior with RH_{SBM} for both of these variables. A partial explanation of the complexity comes from the surface energy budget (given for the equator in Table 7.5). As RH_{SBM} is decreased, the surface relative humidity decreases essentially along with this parameter. The evaporation thus increases; however in order to preserve energy balance the surface temperature decreases, decreasing both the sensible heat flux and radiative flux. The surface budget changes vary significantly with latitude, causing nonuniform changes in both temperature and gross moist stability with latitude. The Hadley circulation additionally varies somewhat with latitude.

To understand fully all the changes in the tropical general circulation as the parameter RH_{SBM} is varied, more focused studies are necessary, that can effectively

Simulation	P(eq)	max(Had)
$RH_{SBM} = .8$	308	192
$RH_{SBM} = .7$	291	184
$RH_{SBM} = .6$	272	199
$RH_{SBM} = .5$	345	192

Table 7.4: Precipitation at the equator (W/m^2) and maximum meridional overturning streamfunction ($10^9 kg/s$) for the simulations varying the convection scheme relative humidity parameter RH_{SBM}.

Simulation	E	Q_{SH}	Q_{LW}
$RH_{SBM} = .8$	134	28	-70
$RH_{SBM} = .7$	142	24	-67
$RH_{SBM} = .6$	151	19	-63
$RH_{SBM} = .5$	170	12	-51

Table 7.5: Energy balance at the equator (W/m^2) for the simulations varying the convection scheme relative humidity parameter RH_{SBM}. These terms, which all act to cool the surface, are balanced by a short wave surface heating of 233 W/m^2 in each case.

isolate the mechanisms mentioned in the previous paragraph (e.g., the response of the Hadley circulation system to changes in gross moist stability, evaporation distribution, short wave heating distribution, etc.). We are currently performing such studies, but at the moment lacking succinct theories for this behavior, we emphasize the relative insensitivity of the tropical circulation to this parameter, and proceed with study of what value of RH_{SBM} is needed to use a relaxation time of $\tau_{SBM} = 16h$, as suggested by Bretherton et al. (2004).

7.4.3 Feasibility of Using 16 h Relaxation Time

Using $RH_{SBM} = .5$ with $\tau_{SBM} = 16h$ decreases the fraction of large scale precipitation at the equator to only 7%; using a value of $RH_{SBM} = .4$ decreases the ratio to below 1%. The midtropospheric relative humidity values at the equator are below 90% for $RH_{SBM} = .5$, and approximately 80% for $RH_{SBM} = .4$. This suggests that the value of the relaxation time best suggested from the observations of Bretherton et al. (2004) can be utilized effectively with the SBM convection scheme, provided $RH_{SBM} \leq .5$. The simulations with this longer relaxation time have a property not seen in the other simulations with no large scale condensation in the tropics. This can be seen in Figure 7.14, a plot of moist static energy flux by the Hadley circulation for $\tau_{SBM} = 16h$ and $RH_{SBM} = .5$ and $\tau_{SBM} = 16h$ and $2h$. The simulations with the longer relaxation time again exhibit a region with reduced Hadley cell moist static energy fluxes in the deep tropics, as some of the LSC only simulations. The reduced fluxes by the mean flow is offset by eddy fluxes of moist static energy within this region, and again is accompanied by reduced gross moist stability, strengthened Hadley circulation, and increased precipitation, but only within the region of reduced fluxes in Figure 7.14. This again points to the gross moist stability as an important diagnostic quantity of convection schemes, and suggests that this quantity can be changed by methods other than large scale precipitation.

7.5 Conclusions

In this chapter we have formulated a new simplified convection scheme in the style of Betts and Miller which can be used to study tropical circulations within a variety of model frameworks. The scheme relaxes to temperature and humidity reference profiles that are slightly more idealized than the full Betts-Miller scheme: a moist adiabat, and a specified relative humidity with respect to this adiabat. The method

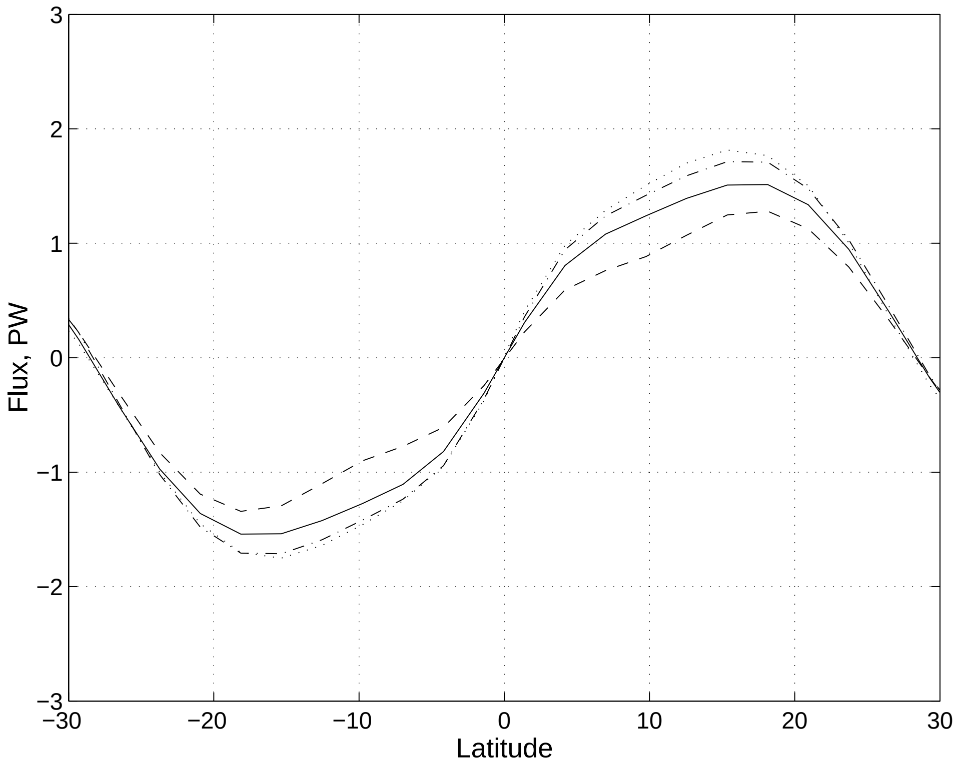

Figure 7.14: Vertically integrated meridional moist static energy flux by the mean flow for the SBM scheme with shallower shallow convection and $RH_{SBM} = .5$ and $\tau_{SBM} = 2h$ (solid) and $RH_{SBM} = .5$ and $\tau_{SBM} = 16h$ (dotted).

of enthalpy conservation used is the same as that of Betts and Miller; this scheme changes the reference temperature, implying that the reference profile is no longer an adiabat after the correction.

The primary simplification we make from the full Betts-Miller scheme is with the treatment of shallow (non-precipitating) convection. Whereas Betts and Miller perform their relaxation to mixing-line structures up to a specified depth, we propose shallow convection methods which can be used to simulate a wide variety of climates, with no empirical parameters such as the shallow convection depth. We study the behavior of three different shallow convection schemes, which are called when the predicted precipitation is less than zero: no shallow adjustment, a scheme which reduces the depth of convection in a continuous manner, and a scheme which adjusts all the way to the level of zero buoyancy.

We then study the effect of this convection scheme on the tropical circulation within the idealized moist GCM framework given in Chapter 2. In comparing with LSC only and MCA simulations, and among the three shallow convection formulations, we have found that a key categorization of convection schemes is the ability to build up and rapidly release CAPE. We find that schemes with an abrupt convective "trigger" such as LSC only or MCA, which require large scale saturation of the gridbox in order to be called, produce significantly different zonally averaged climates as compared with schemes with a less abrupt trigger. The latter consists of the SBM simulations with shallow convection, but surprisingly not the SBM simulations without shallow convection. Without non-precipitating convection to transport heat and moisture upwards, the simulations can build up a significant amount of CAPE: the relaxed nature of the convection is essentially ineffective without some shallow adjustment. These simulations take on many of the characteristics of the LSC only or MCA simulations, such as increased Hadley circulation transports, increased ITCZ precipitation, equatorward transport of energy within the Hadley cell, resolution dependence of energy transports, zonal winds, and relative humidity, and large variance of vertical velocity.

We can increase the abruptness of the trigger within the SBM schemes by requiring more humidity before deep convection is allowed. With this change, the simulations with no shallow convection exhibit even more similarity to LSC only simulations. Additionally, the two shallow convection methods show some divergence in these simulations as well: the scheme that lowers the depth for shallow convection can build up more CAPE, and shows a reduced amount of Hadley cell energy transport when the reference relative humidity is increased.

The SBM schemes exhibit less sensitivity to horizontal resolution as compared to the LSC only simulations. There is less of a tendency to superrotate in the equatorial upper troposphere (which is present at low resolution in the LSC only simulations but disappears at higher resolutions). A resolution of T42 or higher is necessary for adequate convergence of the SBM schemes, whereas the LSC only simulations require at least T85 or T170 for some fields.

We find the SBM simulations to be remarkably insensitive to convective relaxation time, provided large scale condensation is not allowed to occur. As convective relaxation time is increased, the latent heating remains essentially the same while the relative humidity of the atmosphere exceeds the reference value by a larger amount. Eventually, however, large scale precipitation takes over, and the simulations behave similarly to LSC only simulations. A relaxation time of 16 hrs (suggested from observations by Bretherton et al. (2004)) is not useful unless a reference relative humidity of .5 or below is used.

The sensitivity to reference relative humidity is more complex, primarily because the surface budget changes significantly as relative humidity is varied. There is nonuniform behavior in many variables as reference relative humidity is varied. We believe that more focused studies are required to understand the behavior of the

Hadley circulation and ITCZ under different climate regimes. We are currently investigating the determination and importance of the gross moist stability within the idealized GCM over fixed SST boundary conditions, in hope that this can further elucidate some of the results from this chapter.

Chapter 8

Conclusions

In this thesis we have developed a new moist general circulation model, and used this to study a variety of topics involving the effect of moisture on the general circulation of the atmosphere, including midlatitude static stability, eddy scales, and energy fluxes, and the effect of convection on the zonally averaged tropical circulation. Firstly we hope that this work will encourage others to pursue research using models of a similar intermediate complexity, between simple models and full GCM's. Models of this complexity can be a useful way to understand the complex dynamics of full GCM's. Intermediate complexity models can connect to simple models both by using the frameworks suggested by simple models to interpret results, and by providing clean tests of the usefulness of the simple theories. Further, the idealizations of intermediate complexity models as compared with full GCM's can allow the modeler to isolate certain feedbacks while suppressing others, and vary parameters over wide ranges to better understand climate feedbacks and processes.

There are many choices to be made of which physical processes to include within intermediate complexity models; within this work we have chosen to ignore all radiative feedbacks to focus on the dynamical effects of moisture. There are vast amount of additional sets of models that can be constructed; we hope that this work can serve as a building block for other work of similar levels of complexity. For example, concerning water vapor, the study of Pierrehumbert (2002) points out the vast range of effects of water in all its forms on the Earth's climate: as an amplifier of baroclinic eddy energy transports, a long wave radiative absorber, a short wave radiative reflector, etc. The review of Pierrehumbert et al. (2005) then presents simulations in which the dynamical feedbacks of increased water content are limited in favor of the radiative feedbacks, essentially the opposite of the model presented here. These simulations increase the long wave radiative impact of water vapor, and study the temperature response to altered water vapor contents. It is clear that there are many related intermediate complexity models that isolate the effect of other climate process on the circulation.

We hope that the model has been constructed and presented in a simple and clear enough manner so that these results are easily reproducible and extended. Reproducibility of the model was a primary goal of our formulation. For instance, the Monin-Obukhov surface flux scheme was simplified on the unstable side so that iteration is no longer necessary to obtain the drag coefficients. Additionally, the large-scale condensation scheme and the simplified Betts-Miller scheme are both easily reproducible in the realm of convection schemes, which are often sensitive to undocumented aspects of their formulation. We believe reproducibility of results is key for understanding of these models to build progressively.

In our study of midlatitude dynamics, we first investigated the determination of the static stability in Chapter 3. The static stability is found to be a strong function of the moisture content of the atmosphere. This is expected in the deep tropics, where the temperature structure is essentially on the moist adiabat, and dry stability increases with moisture content. However, we observe this behavior throughout the subtropics and midlatitudes as well. The effects of moist convection are found to overwhelm baroclinic eddies in setting the atmospheric stability over a wide range of moisture content, from completely dry to ten times the moisture of the current climate. This is in accordance with the theory of Juckes (2000), and goes against the typical thinking of baroclinic adjustment and other instability theories (Stone (1978a); Held (1982); Schneider (2004)). These dry baroclinic eddy theories for static stability derive the observed result that the normalized isentropic slope is of order one, i.e., that the isentrope leaving the boundary layer in the subtropics reaches the tropopause at the poles. Our work suggests that this result appears simply by coincidence; it is thus not surprising that the other predictions of the dry baroclinic adjustment theories do not bare out in observations or models (Juckes (2000); Thuburn and Craig (1997)). The stability above the moist adiabat in Juckes' theory is determined by the surface variance of moist static energy, with convection in the warmest cores of baroclinic eddies setting the effective temperature of the tropopause. The moist stability in our model therefore increases with moisture content as well, as the surface variance is larger in cases with more water vapor.

We then studied the effect of this change in stability on eddy length scales. Despite a large change in the Rossby radius as the static stability is changed, the length scales of baroclinic eddies change vary little. The energy content of the simulations changes drastically as well, suggesting that the typical Rhines scale is not valid for the eddy scale measure either. However, when the large change of jet latitude with moisture is taken into account and the Rhines scale at the latitude of maximum eddy kinetic energy is used, the length scales are in accordance with this prediction. The primary conclusion of this section is that typical definitions of the Rossby radius appear to have little bearing on the length scales of baroclinic eddies.

Next in Chapter 4 we focused on the changes in the meridional flux of moist static energy as the moisture content is changed. This question is key to how temperature gradients will change with global warming, and to elucidate the range of energy fluxes and temperature gradients possible in paleoclimate regimes. In our simulations, although moisture fluxes increase significantly as moisture content is increased, there is a remarkable compensating decrease of dry static energy fluxes that leaves the total energy fluxes nearly perfectly unchanged. The energy fluxes increase slightly as moisture content is increased, but are nearly identical as moisture is decreased.

We interpret this behavior using energy balance models, first with a model that exhibits exact compensation as the moisture content is varied. The key assumptions of this model are fixed diffusivity with moisture, and neutral moist stability to the emission level. The former assumption implies linearity of moisture and dry static energy fluxes versus their respective gradients; the latter assumption implies that the surface gradients are immediately communicated to gradients at the emission level. This simple model suggests that some degree of compensation is expected in GCM's, and that changes in diffusivity and moisture at the emission level are important for deviations from compensation.

We expand upon this simplest energy balance model to study the changes in diffusivity with moisture. When diffusivities from the model are diagnosed and substituted in the EBM with actual moist adiabats calculated, a similar amount of compensation is observed. The product of typical eddy length scales and velocity scales additionally scales with the diffusivity, suggesting the mixing length framework is valid. The diffusivity of the model decreases significantly as moisture content is increased, but remains approximately constant as the moisture content is decreased. This follows from our observation that eddy kinetic energy scales with the mean dry available potential energy, i.e., with the strength of the baroclinic component of the jet. The eddy kinetic energy and jet strength both decrease in the cases with more moisture, since dry static energy gradients decrease in this limit.

Another prominent characteristic of the moist simulations is that the eddy-driven jet moves significantly poleward as moisture content is increased. We understand this essentially as due to the location of maximum temperature gradients moving poleward. This, in turn, can be well predicted from moist adiabats traced down from the fixed emission temperatures implied by constant energy fluxes. These arguments do not reference momentum fluxes, or meridional propagation at all to explain the position of the jet. This theory therefore cannot explain the results of Robinson (1997) or G. Chen (personal communication, 2005), who vary surface friction and observe a movement of the jet latitude. However the large magnitudes of jet movement we observe here from moisture content (which dominate the possible changes from surface friction) suggest that thermodynamic constraints place a strong control on the location of the eddy-driven jet.

We construct a full energy balance model using the theories described above: neutral moist stability to the emission level, the Rhines scale at latitude of maximum eddy kinetic energy for the length scale, the latitude of maximum temperature gradients for the jet latitude, and eddy kinetic energy from the mean dry available potential energy. The resulting model predicts qualitatively all of the characteristics of the simulations described above, in a fully predictive model.

In Chapter 5, we shift our focus to the tropics, and formulate a simple model for the study of precipitation effects on tropical dynamics. The model is derived systematically from the primitive equations in a derivation suitable for an applied mathematics audience. This model can be used to study a variety of problems in tropical dynamics including the determination of precipitation regions, convectively-coupled tropical waves, and the Walker circulation. In Chapter 6, we use this model to study "precipitation fronts," which mark the border between precipitating and non-precipitating regions in the tropics. We derive the dynamics for these waves, including their structure and speed of propagation. There are three classes of fronts with different propagation characteristics. For instance, the "drying fronts" move from the dry region into the moist region at speeds in between the moist phase speed and the dry phase speed. All of the theoretically predicted fronts, derived under the vanishing relaxation time limit, are realizable in numerical simulations with a remarkable amount of accuracy with realistic finite relaxation times. Additionally we present Walker cell simulations that show that when a mean wind is applied, fronts develop in the steady forced-dissipative solution; therefore precipitation fronts are expected to be omnipresent in time-varying solutions. This is in accordance with expectations from energy principles we derive.

We then study similar tropical dynamical questions with the idealized moist GCM. Using large-scale convection only within the GCM yields a tropical circulation which is sensitive to resolution and excessively variant in the deep tropics. In order to remedy these deficiencies, we designed a simplified convection scheme in the style of Betts and Miller in Chapter 7, which we call the simplified Betts-Miller (SBM) scheme. The introduction of this convection scheme brings about significant changes to the tropical circulation. In general, with the convection scheme, the tropical circulation becomes more steady and less sensitive to resolution, the Hadley circulation decreases in strength and transports more energy poleward, there is less equatorial precipitation, and the zonal winds are less likely to exhibit equatorial superrotation in the upper troposphere.

We study the response of the tropical circulation to the two SBM parameters, the convective relaxation time and the reference profile relative humidity, as well as to the formulation of shallow convection. The primary result of this study is that a key classification of convection schemes is whether these can build up and rapidly release convectively available potential energy. Schemes with an abrupt trigger and rapid release behave more like the LSC only simulations in terms of resolution sensitivity, Hadley cell strength, and precipitation distribution. The formulation of the shallow convection scheme is of vital importance in the determination of this abruptness of convection. When no shallow convection scheme is used within the SBM scheme, even with long convective relaxation times the simulations are similar in the tropics to the LSC only simulations. The two shallow convection schemes that we study have slightly different behavior in the abruptness of convection.

As we vary the convective relaxation time for the SBM scheme, there is little change in Hadley circulation and tropical precipitation. The tropics respond simply by increasing their relative humidity distribution to become farther from the reference value as the relaxation time becomes larger. This is in accordance with the prediction of the simple model in Chapters 5-6. This behavior can continue with increasing relaxation time until the typical relative humidity values approach saturation. At that point large scale precipitation sets in, and the atmosphere is able to build up and rapidly release convectively available potential energy, and shares the characteristics of the LSC only simulations.

While the simulations are remarkably insensitive to convective relaxation time, the sensitivity to the assumed relative humidity of the reference profile is more obscure. The Hadley circulation and equatorial precipitation distribution change somewhat as this parameter is varied. We believe this is complicated by changes in the surface budget, in which terms such as radiative cooling and sensible heat flux must change to compensate the surface relative humidity change driven by the convection scheme. We believe more targeted studies are necessary to fully understand the influence of moisture and convection on the Hadley circulation system.

The primary result from our studies of the tropics is that it is possible to construct a class of convection schemes which are easily reproducible and relatively insensitive to convection scheme parameters. Having elucidated the principle sensitivities of this scheme, we can now proceed to more focused studies on the influence of moisture on the Hadley circulation, the equatorial precipitation distribution, and the tropical general circulation as a whole. We believe the simplified moist GCM that we have constructed in this thesis will continue to be useful for studying the Hadley circulation system and other outstanding problems involving the effect of moisture on the general circulation of the atmosphere.

Bibliography

Arakawa, A. and W. H. Schubert: 1974, Interaction of a cumulus cloud ensemble with the large-scale environment, Part I. *J. Atmos. Sci.*, **31**, 674–701.

Barry, L., G. C. Craig, and J. Thuburn: 2002, Poleward heat transport by the atmospheric heat engine. *Nature*, **415**, 774–777.

Betts, A. K.: 1986, A new convective adjustment scheme. Part I: Observational and theoretical basis. *Quart. J. Roy. Meteor. Soc.*, **112**, 677–692.

Betts, A. K. and M. J. Miller: 1986, A new convective adjustment scheme. Part II: Single column tests using GATE wave, BOMEX, and arctic air-mass data sets. *Quart. J. Roy. Meteor. Soc.*, **112**, 693–709.

Bourlioux, A. and A. J. Majda: 1995, Theoretical and numerical structure of unstable detonations. *Phil. Trans. R. Soc. London A*, **350**, 29–68.

Branscome, L. E.: 1983, A parameterization of transient eddy heat flux on a beta-plane. *J. Atmos. Sci.*, **40**, 2508–2521.

Bretherton, C., M. E. Peters, and L. E. Back: 2004, Relationships between water vapor path and precipition over the tropical oceans. *J. Climate*, **17**, 1517–1528.

Bretherton, C. S. and A. H. Sobel: 2002, A simple model of a convectively coupled Walker Circulation using the weak temperature gradient approximation. *J. Climate*, **15**, 2907–2920.

Brown, R. G. and C. S. Bretherton: 1997, A test of the strict quasi-equilibrium theory on long time and space scales. *J. Atmos. Sci.*, **54**, 624–638.

Budyko, M. I.: 1969, The effect of solar radiation variations on the climate of the earth. *Tellus*, **21**, 611–619.

Cabellero, R. and P. L. Langen: 2005, The dynamic range of poleward energy transport in an atmospheric general circulation model. *Geophys. Res. Lett.*, **32**, L2705, doi:10.1029/2004GL021581.

Cane, M. A., S. E. Zebiak, and S. C. Dolan: 1986, Experimental forecasts of El Niño. *Nature*, **321**, 827–832.

Charney, J. and A. Eliassen: 1964, On the growth of the hurricane depression. *J. Atmos. Sci.*, **21**, 68–75.

Chen, G. Q., C. D. Levermore, and T. P. Liu: 1994, Hyperbolic conservation laws with stiff relaxation terms and entropy. *Comm. Pure Appl. Math.*, **47**, 787–830.

Colella, P., A. Majda, and V. Roytburd: 1986, Theoretical and numerical structure for reacting shock waves. *SIAM J. Sci. Statist. Comput.*, **7**, 1059–1080.

Collela, P. and P. R. Woodward: 1984, The Piecewise Parabolic Method (PPM) for gas-dynamical simulations. *J. Comp. Phys.*, **54**, 174–201.

Donner, L. J.: 1986, Sensitivity of the thermal balance in a general circulation model to a parameterization for cumulus convection with radiatively interactive clouds. *J. Atmos. Sci.*, **43**, 2277–2288.

Donner, L. J., H.-L. Kuo, and E. J. Pitcher: 1982, The significance of thermodynamic forcing by cumulus convection in a general circulation model. *J. Atmos. Sci.*, **39**, 2159–2181.

Emanuel, K. A.: 1987, An air-sea interaction model of intraseasonal oscillations in the tropics. *J. Atmos. Sci.*, **44**, 2324–2340.

— 1988, Observational evidence of slantwise convective adjustment. *Mon. Wea. Rev.*, **116**, 1805–1816.

— 1994, *Atmospheric Convection*. Oxford Press.

Emanuel, K. A., M. Fantini, and A. J. Thorpe: 1987, Baroclinic instability in an environment of small stability to slantwise moist convection. Part I: Two-dimensional models. *J. Atmos. Sci.*, **44**, 1559–1573.

Emanuel, K. A., J. D. Neelin, and C. S. Bretherton: 1994, On large-scale circulations in convecting atmospheres. *Quart. J. Roy. Meteor. Soc.*, **120**, 1111–1143.

Fang, M. and K. K. Tung: 1997, The dependence of the Hadley circulation on the thermal relaxation time. *J. Atmos. Sci.*, **54**, 1379–1384.

Franzke, C.: 2002, Dynamics of low-frequency variability: Barotropic mode. *J. Atmos. Sci.*, **59**, 2897–2909.

Franzke, C., S. Lee, and S. B. Feldstein: 2004, Is the North Atlantic oscillation a breaking wave? *J. Atmos. Sci.*, **61**, 145–160.

Frierson, D. M. W.: 2005, The dynamics of idealized convection schemes and their effect on the zonally averaged tropical circulation. *J. Atmos. Sci., in prep.*

Frierson, D. M. W., I. M. Held, and P. Zurita-Gotor: 2005a, A gray-radiation aquaplanet moist GCM. Part I: Static stability and eddy scale. *Submitted to J. Atmos. Sci.*.

— 2005b, A gray-radiation aquaplanet moist GCM. Part II: Energy transports in altered climates. *J. Atmos. Sci., in prep.*

Frierson, D. M. W., A. J. Majda, and O. M. Pauluis: 2004, Large scale dynamics of precipitation fronts in the tropical atmosphere: A novel relaxation limit. *J. Comm. Math. Sci.*, **2**, 591–626.

Garner, S. T., D. M. W. Frierson, I. M. Held, O. M. Pauluis, and G. K. Vallis: 2005, "Deep Earth" global cloud resolving simulations. *J. Atmos. Sci., in prep*.

Gill, A. E.: 1980, Some simple solutions for heat induced tropical circulations. *Quart. J. Roy. Meteor. Soc.*, **106**, 447–462.

— 1982, *Atmosphere-Ocean Dynamics*. Academic Press.

Green, J. S.: 1970, Transfer properties of the large scale eddies and the general circulation of the atmosphere. *Quart. J. Roy. Meteor. Soc.*, **96**, 157–185.

Haine, T. W. N. and J. Marshall: 1998, Gravitational, symmetric, and baroclinic instability of the ocean mixed layer. *J. Phys. Oceanogr.*, **28**, 634–658.

Harnik, N. and E. K. M. Chang: 2004, The effects of variations in jet width on the growth of baroclinic waves: Implications for midwinter Pacific storm track variability. *J. Atmos. Sci.*, **61**, 23–40.

Harten, A., B. Engquist, S. Osher, and S. Chakravarthy: 1987, Uniformly high-order essentially non-oscillatory schemes III. *J. Comput. Phys.*, **71**, 231–303.

Hartmann, D. L.: 1994, *Global physical climatology*. Academic Press.

Haynes, P., J. Scinocca, and M. Greenslade: 2001, Formation and maintenance of the extratropical tropopause by baroclinic eddies. *Geophys. Res. Lett.*, **28**, 4179–4182.

Held, I. M.: 1982, On the height of the tropopause and the static stability of the troposphere. *J. Atmos. Sci.*, **39**, 412–417.

— 2004, The gap between simulation and understanding in climate modeling. *Submitted to Bull. Amer. Meteor. Soc.*.

Held, I. M. and I.-S. Kang: 1987, Barotropic models of the extratropical response to El Niño. *J. Atmos. Sci.*, **44**, 3576–3586.

Held, I. M. and V. D. Larichev: 1996, A scaling theory for horizontally homogeneous, baroclinically unstable flow on a beta plane. *J. Atmos. Sci.*, **53**, 946–952.

Held, I. M. and M. J. Suarez: 1994, A proposal for the intercomparison of the dynamical cores of atmospheric general-circulation models. *Bull. Amer. Meteor. Soc.*, **75**, 1825–1830.

Hess, P. G., D. S. Battisti, and P. J. Rasch: 1993, Maintenance of the intertropical convergence zones and the large-scale tropical circulation on a water-covered Earth. *J. Atmos. Sci.*, **50**, 691–713.

IPCC: 2001, *Climate Change 2001: The Scientific Basis. Contribution of Working Group I to the Third Assessment Report of the Intergovernmental Panel on Climate Change*. Cambridge University Press.

Janjic, Z. I.: 1994, The step-mountain Eta coordinate model: Further developments of the convection, viscous sublayer, and turbulence closure schemes. *Mon. Wea. Rev.*, **122**, 927–945.

Jin, S. and Z. P. Xin: 1995, The relaxation schemes for systems of conservation laws in arbitrary space dimensions. *Comm. Pure Appl. Math.*, **48**, 235–276.

Juckes, M. N.: 2000, The static stability of the midlatitude troposphere: The relevance of moisture. *J. Atmos. Sci.*, **57**, 3050–3057.

Katsoulakis, M. A. and A. E. Tzavaras: 1997, Contractive relaxation systems and the scalar multidimensional conservation law. *Comm. Partial Diff. Eqns.*, **22**, 195–233.

Khouider, B. and A. J. Majda: 2004, A high resolution balanced scheme for an idealized tropical climate model. *Submitted to Theoret. and Comp. Fluid Dyn.*.

Kuang, Z., P. N. Blossey, and C. S. Bretherton: 2005, A new approach for 3D cloud resolving simulations of large scale atmospheric circulation. *Geophys. Res. Lett.*, **32**, L02809, doi: 10.1029/2004GL021024.

Kushner, P. J. and L. M. Polvani: 2004, Stratosphere-troposphere coupling in a relatively simple AGCM: The role of eddies. *J. Climate*, **17**, 629–639.

Lapeyre, G. and I. M. Held: 2003, Diffusivity, kinetic energy dissipation, and closure theories for the poleward eddy heat flux. *J. Atmos. Sci.*, **60**, 2907–2916.

— 2004, The role of moisture in the dynamics and energetics of turbulent baroclinic eddies. *J. Atmos. Sci.*, **61**, 1693–1710.

Lindzen, R. S. and S. Nigam: 1987, On the role of sea surface temperature gradients in forcing low-level winds and convergence in the tropics. *J. Atmos. Sci.*, **45**, 2440–2458.

Lorenz, E. N.: 1963, Deterministic nonperiodic flow. *J. Atmos. Sci.*, **20**, 131–140.

Madden, R. A. and P. R. Julian: 1971, Detection of a 40-50 day oscillation in the zonal wind in the tropical Pacific. *J. Atmos. Sci.*, **28**, 702–708.

— 1994, Observations of the 40-50 day tropical oscillation- A review. *Mon. Wea. Rev.*, **122**, 814–837.

Majda, A. J.: 1981, A qualitative model for dynamic combustion. *SIAM J. Appl. Math.*, **41**, 70–93.

— 1984, *Compressible fluid flow and systems of conservation laws in several space variables*. Applied Math Sciences 53, Springer-Verlag, New York.

— 2003, *Introduction to PDE's and waves for the atmosphere and ocean*. Courant Institute Lecture Series #9. Amer. Math. Soc.

Majda, A. J. and J. A. Biello: 2003, The nonlinear interaction of barotropic and equatorial baroclinic Rossby waves. *J. Atmos. Sci.*, **60**, 1809–1821.

Majda, A. J., B. Khouider, G. N. Kiladis, K. H. Straub, and M. G. Shefter: 2004, A model for convectively coupled tropical waves: Nonlinearity, rotation and comparison with observations. *J. Atmos. Sci.*, **61**, 2188–2205.

Majda, A. J. and M. Shefter: 2001a, Models of stratiform instability and convectively coupled waves. *J. Atmos. Sci.*, **58**, 1567–1584.

— 2001b, Waves and instabilities for model tropical convective parameterizations. *J. Atmos. Sci.*, **58**, 896–914.

Majda, A. J. and P. E. Souganidis: 2000, The effect of turbulence on mixing in prototype reaction-diffusion systems. *Comm. Pure Appl. Math.*, **53**, 1284–1304.

Manabe, S. and A. J. Broccoli: 1985, The influence of continental ice sheets on the climate of an ice age. *J. Geophys. Res.*, **90**, 2167–2190.

Manabe, S., K. Bryan, and M. J. Spelman: 1975, A global ocean-atmosphere climate model. Part I. The atmospheric circulation. *J. Phys. Oceanogr.*, **5**, 3–29.

Manabe, S., J. Smagorinsky, and R. F. Strickler: 1965, Simulated climatology of a general circulation model with a hydrologic cycle. *Mon. Wea. Rev.*, **93**, 769–798.

Manabe, S. and T. B. Terpstra: 1974, The effects of mountains on the general circulation of the atmosphere as identified by numerical experiments. *J. Atmos. Sci.*, **31**, 3–42.

Mapes, B. E. and R. Houze: 1995, Diabatic divergence profiles in western Pacific mesoscale convective systems. *J. Atmos. Sci.*, **52**, 1807–1828.

Matsuno, T.: 1966, Quasi-geostrophic motions in the equatorial area. *J. Meteor. Soc. Japan*, **44**, 25–43.

Mechoso, C. R. and coauthors: 1995, The seasonal cycle over the tropical Pacific in coupled ocean-atmosphere general circulation models. *Mon. Wea. Rev.*, **123**, 2825–2838.

Neelin, J. and J. Yu: 1994, Modes of tropical variability under convective adjustment and the Madden-Julian Oscillation. Part I: Analytical theory. *J. Atmos. Sci.*, **51**, 1876–1894.

Neelin, J. D. and I. M. Held: 1987, Modeling tropical convergence based on the moist static energy budget. *Mon. Wea. Rev.*, **115**, 3–12.

Neelin, J. D., I. M. Held, and K. H. Cook: 1987, Evaporation-wind feedback and low-frequency variability in the tropical atmosphere. *J. Atmos. Sci.*, **44**, 2341–2348.

Neelin, J. D. and N. Zeng: 2000, A quasi-equilibrium tropical circulation model – formulation. *J. Atmos. Sci.*, **57**, 1741–1766.

Numaguti, A.: 1993, Dynamics and energy balance of the Hadley circulation and tropical precipitation zones: Significance of the distribution of evaporation. *J. Atmos. Sci.*, **50**, 1874–1887.

— 1995, Dynamics and energy balance of the Hadley circulation and tropical precipitation zones. Part II: Sensitivity to meridional SST distribution. *J. Atmos. Sci.*, **52**, 1128–1141.

Pauluis, O. M., A. J. Majda, and D. M. W. Frierson: 2005, Propagation, reflection, and transmission of precipitation fronts in the tropical atmosphere. *In prep for J. Atmos. Sci.*.

Pavan, V. and I. M. Held: 1996, The diffusive approximation for eddy fluxes in baroclinically unstable jets. *J. Atmos. Sci.*, **53**, 1262–1272.

Pedlosky, J.: 1987, *Geophysical Fluid Dynamics*. Springer-Verlag, second edition.

Philander, S. G. H., T. Yamagata, and R. Pacanowski: 1984, Unstable air-sea interactions in the tropics. *J. Atmos. Sci.*, **41**, 604–613.

Pierrehumbert, R. T.: 2002, The hydrologic cycle in deep-time climate problems. *Nature*, **419**, 191–198.

Pierrehumbert, R. T., H. Brogniez, and R. Roca: 2005, On the relative humidity of the earth's atmosphere. *The General Circulation*, T. Schneider and A. Sobel, eds., Princeton University Press (to appear).

Rhines, P. B.: 1975, Waves and turbulence on a beta-plane. *J. Fluid Mech.*, **69**, 417–443.

Roads, J. O., S.-C. Chen, and F. Fujioka: 2001, ECPC's weekly to seasonal global forecasts. *Bull. Amer. Meteor. Soc.*, **82**, 639–658.

Robinson, W. A.: 1997, Dissipation dependence of the jet latitude. *J. Climate*, **10**, 176–182.

Satoh, M.: 1994, Hadley circulations in radiative-convective equilibrium in an axially symmetric atmosphere. *J. Atmos. Sci.*, **51**, 1947–1968.

Schneider, T.: 2004, The tropopause and the thermal stratification in the extratropics of a dry atmosphere. *J. Atmos. Sci*, **61**, 1317–1340.

Seager, R., R. Murtugudde, N. Naik, A. Clement, N. Gordon, and J. Miller: 2003, Air-sea interaction and the seasonal cycle of the subtropical anticyclones. *J. Climate*, **16**, 1948–1966.

Sellers, W. D.: 1969, A climate model based on the energy balance of teh earth-atmosphere system. *J. Appl. Meteor.*, **8**, 392–400.

Slingo, J. M. and coauthors: 1996, Intraseasonal oscillations in 15 atmospheric general circulation models: Results from an AMIP diagnostic subproject. *Climate Dyn.*, **12**, 325–357.

Sobel, A. H., J. Nilsson, and L. M. Polvani: 2001, The weak temperature gradient approximation and balanced tropical moisture waves. *J. Atmos. Sci.*, **58**, 3650–3665.

Sobel, A. H., S. E. Yuter, C. Bretherton, and G. N. Kiladis: 2004, Large-scale meteorology and deep convection during TRMM KWAJEX. *Mon. Wea. Rev.*, **132**, 422–444.

Stone, P. H.: 1972, A simplified radiative-dynamical model for the static stability of rotating atmospheres. *J. Atmos. Sci*, **29**, 405–418.

— 1978a, Baroclinic adjustment. *J. Atmos. Sci*, **35**, 561–571.

— 1978b, Constraints on dynamical transports of energy on a spherical planet. *Dyn. Atmos. Oceans*, **2**, 123–139.

Stone, P. H. and M.-S. Yao: 1990, Development of a 2-dimensional zonally averaged statistical-dynamic model. 3. The parameterization of eddy fluxes of heat and moisture. *J. Climate*, **3**, 726–740.

Swanson, K. and R. T. Pierrehumbert: 1997, Lower-tropospheric heat transport in the Pacific storm track. *J. Atmos. Sci.*, **54**, 1533–1543.

Thuburn, J. and G. C. Craig: 1997, GCM tests of theories for the height of the tropopause. *J. Atmos. Sci.*, **54**, 869–882.

Trenberth, K. E. and J. M. Caron: 2001, Estimates of meridional atmosphere and ocean heat transports. *J. Climate*, **14**, 3433–3443.

Trenberth, K. E. and D. P. Stepaniak: 2003a, Covariability of components of poleward atmospheric energy transports on seasonal and interannual timescales. *J. Climate*, **16**, 3691–3705.

— 2003b, Seamless poleward atmospheric energy transports and implications for the Hadley Circulation. *J. Climate*, **16**, 3706–3722.

Troen, I. and L. Mahrt: 1986, A simple model of the atmospheric boundary layer: sensitivity to surface evaporation. *Bound.-Layer Meteor.*, **37**, 129–148.

Waliser, D. E., K. M. Lau, W. Stern, and C. Jones: 2003, Potential predictability of the Madden-Julian Oscillation. *Bull. Amer. Meteor. Soc.*, **122**, 814–837.

Williams, F. A.: 1985, *Combustion theory*. Benjamin/Cummings Publishing Company.

Williams, G.: 2003, Barotropic instability and equatorial superrotation. *J. Atmos. Sci.*, **60**, 2136–2152.

Xu, K.-M. and K. A. Emanuel: 1989, Is the tropical atmosphere conditionally unstable? *Mon. Wea. Rev.*, **117**, 1471–1479.

Yano, J.-I. and K. A. Emanuel: 1991, An improved model of the equatorial troposphere and its coupling to the stratosphere. *J. Atmos. Sci.*, **48**, 377–389.

Yano, J.-I., J. C. McWilliams, M. W. Moncrieff, and K. A. Emanuel: 1995, Heirarchical tropical cloud systems in an analog shallow-water model. *J. Atmos. Sci.*, **52**, 1723–1742.

Zurita-Gotor, P.: 2005, Updraft/downdraft constraints for moist baroclinic modes and their implications for the shortwave cutoff and maximum growthrate. *Submitted to J. Atmos. Sci.*.